Max-Planck-Institut
für Meteorologie

MAX-PLANCK-GESELLSCHAFT

International Max Planck Research School
on Earth System Modelling

The Role of Heterogeneities and Land-Atmosphere Interactions in the Development of Moist Convection

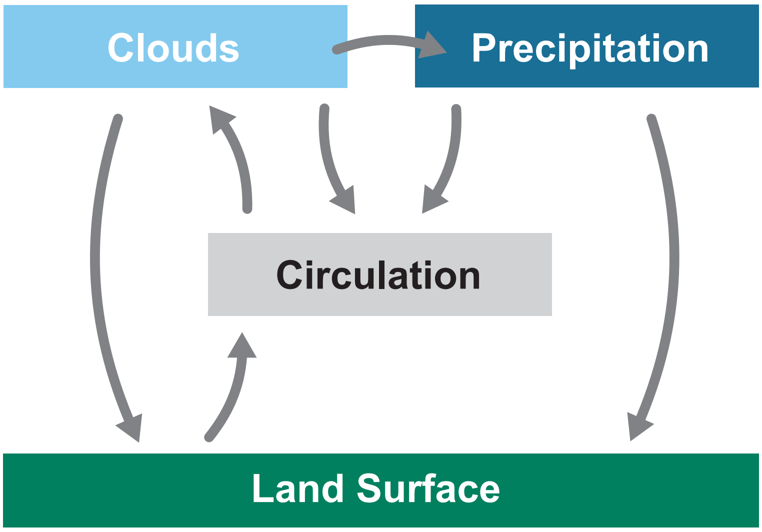
Clouds
Precipitation
Circulation
Land Surface

Malte Rieck

Hamburg 2015

Berichte zur Erdsystemforschung
Reports on Earth System Science

167
2015

Hinweis

Die Berichte zur Erdsystemforschung werden vom Max-Planck-Institut für Meteorologie in Hamburg in unregelmäßiger Abfolge herausgegeben.

Sie enthalten wissenschaftliche und technische Beiträge, inklusive Dissertationen.

Die Beiträge geben nicht notwendigerweise die Auffassung des Instituts wieder.

Die "Berichte zur Erdsystemforschung" führen die vorherigen Reihen "Reports" und "Examensarbeiten" weiter.

Anschrift / Address

Max-Planck-Institut für Meteorologie
Bundesstrasse 53
20146 Hamburg
Deutschland

Tel./Phone: +49 (0)40 4 11 73 - 0
Fax: +49 (0)40 4 11 73 - 298

name.surname@mpimet.mpg.de
www.mpimet.mpg.de

Notice

The Reports on Earth System Science are published by the Max Planck Institute for Meteorology in Hamburg. They appear in irregular intervals.

They contain scientific and technical contributions, including Ph. D. theses.

The Reports do not necessarily reflect the opinion of the Institute.

The "Reports on Earth System Science" continue the former "Reports" and "Examensarbeiten" of the Max Planck Institute.

Layout

Bettina Diallo and Norbert P. Noreiks
Communication

Copyright

Photos below: ©MPI-M
Photos on the back from left to right:
Christian Klepp, Jochem Marotzke,
Christian Klepp, Clotilde Dubois,
Christian Klepp, Katsumasa Tanaka

The Role of Heterogeneities and Land-Atmosphere Interactions in the Development of Moist Convection

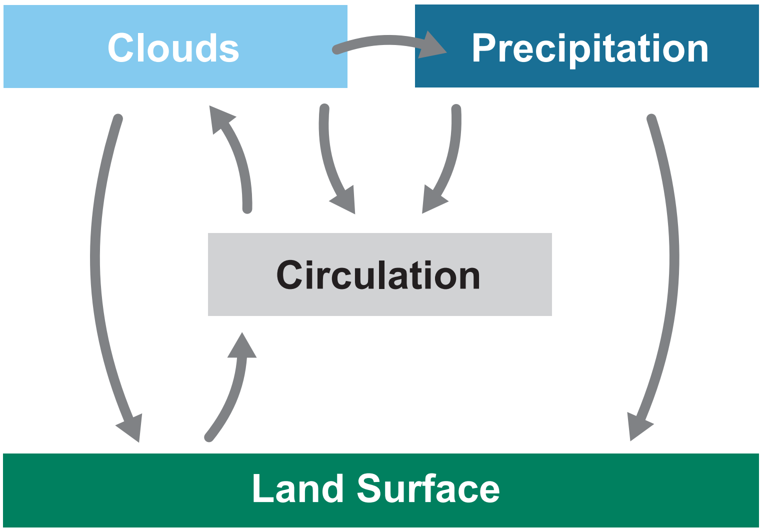
Clouds
Precipitation
Circulation
Land Surface

Malte Rieck

Hamburg 2015

Malte Rieck

Max-Planck-Institut für Meteorologie
Bundesstrasse 53
20146 Hamburg

Als Dissertation angenommen
vom Fachbereich Geowissenschaften der Universität Hamburg

auf Grund der Gutachten von
Prof. Dr. Martin Claußen
und
Dr. Cathy Hohenegger

Hamburg, den 27.01.2015
Prof. Dr. Christian Betzler
Leiter des Departments Geowissenschaften

Berichte zur Erdsystemforschung / Max-Planck-Institut für Meteorologie 167
Reports on Earth System Science / Max Planck Institute for Meteorology 2015

ISSN 1614-1199

Abstract

Numerical weather prediction and climate models face major challenges representing the diurnal cycle of moist convection over land. In particular, the interaction between moist convection and surface heterogeneities is a source of uncertainties, because both processes act on parameterized sub-grid scales. We introduce an interactive land surface into a high-resolution large-eddy simulation model to explicitly resolve the interactions between the two systems. In this dissertation, the coupling between surface heterogeneities, moist convection and related atmospheric circulations is investigated in three studies to advance our understanding and to quantify relationships among the three processes.

First, we investigate the influence of land surface heterogeneities on cloud size development. We approximate the cloud size distribution by a power law with a scale break at the largest clouds. The exponent of the power law is independent of the heterogeneity patch size, implying a similar cloud cover. In contrast, the scale break varies with patch size. The local maximum size, which a cloud can reach, scales with half the patch size. We show that the transition to deep convection is accelerated over heterogeneous surfaces, with an optimum at intermediate patch size (12 to 25 km). The results contradict the concept that larger clouds always grow faster, known from homogeneous surface conditions.

Second, we analyze the effect of precipitating convection on the propagation of an atmospheric circulation induced by a land surface contrast. Three distinct stages are identified. First, a dry convective circulation with a slowly propagating breeze front. Second, the occurrence of deep convection intensifies the circulation and accelerates the front propagation. Third, a precipitation stage, which allows strong cold pools to develop at the breeze front and to further accelerate the propagation speed. Classical theory of density currents fails to represent the second stage and is extended using the cloud base mass flux, which accounts for the observed effects of nonprecipitating convection on the propagation speed. We demonstrate that this theory is applicable to results from large-eddy simulations.

In the last part of this dissertation, we explore how precipitating convection feeds back on heterogeneous surface fluxes on longer timescales. Sensitivity experiments reveal that the infiltration of precipitation in areas of low evapotranspiration tends to homogenize the surface fluxes across the domain. However, two weeks of convective precipitation are not sufficient to completely eliminate the heterogeneity imposed by different vegetation characteristics. In addition, the surface flux spectrum reveals a pronounced homogenization effect by cold pools during periods of precipitation.

Overall, our results highlight the persistent role of surface heterogeneities for convection formation at intermediate patch sizes and in particular the important role of precipitating convection on the propagation of circulations induced by surface heterogeneity. The observed effects are not represented in current weather and climate models.

Zusammenfassung

Numerische Wetter- und Klimamodelle haben Probleme, den Tagesgang von feuchter Konvektion über Land korrekt darzustellen. Insbesondere die Wechselwirkung zwischen tiefer Konvektion und heterogenen Landoberflächen ist in Modellen nicht repräsentiert und eine Quelle für Unsicherheiten. Um diese Effekte zu untersuchen und die beteiligten Prozesse hochaufgelöst zu berechnen, wird ein Modell zur Beschreibung der Landoberfläche in ein atmosphärisches Large-Eddy Modell integriert. Ziel der vorliegenden Doktorarbeit ist ein besseres Verständnis der Wechselwirkungen zwischen der heterogenen Landoberfläche, mesoskaligen Zirkulationen und tiefer Konvektion, um Beziehungen zwischen den Prozessen herstellen zu können.

Zunächst untersuchen wir den Einfluss der Heterogenität der Landoberfläche auf die Größenverteilung der Wolken. Es zeigt sich, dass die Verteilung der Wolken mit einem Potenzgesetz genähert werden kann, wobei ein Skalenabbruch bei den größten Wolken beobachtet wird. Der Exponent des Potenzgesetzes und damit auch der großräumige Wolkenbedeckungsgrad sind in erster Näherung unabhäanging von der Längenskala der Heterogenität. Im Gegensatz dazu hängt der Skalenabbruch von der Längenskala der Heterogenität ab. Die größten Wolken wachsen bis zu einem maximalen Durchmesser, der mit der Hälfte der Längenskala der Heterogenität skaliert. Wir zeigen, dass der Übergang von flacher zu tiefer Konvektion über heterogenen Landoberflächen beschleunigt abläuft, wobei insbesondere mittlere Längenskalen (12-25 km) eine deutliche Beschleunigung bewirken. Darüberhinaus widersprechen die Ergebnisse dieser Studie dem Prinzip, dass die größten Wolken grundsätzlich schneller wachsen, wie es über homogenen Oberflächen postuliert wird.

In zweiten Teil der Dissertation analysieren wir den Einfluss von tiefer Konvektion und Niederschlag auf die Ausbreitungsgeschwindigkeit einer mesoskaligen Zirkulation, die durch Oberflächenheterogenität ausgelöst wurde. Dabei zeigen sich drei klar abgegrenzte Phasen. In der ersten Phase entwickelt sich eine schwache Zirkulation in der trockenen Grenzschicht mit einer sich langsam bewegenden Front. In der zweiten Phase wird die Zirkulation durch das Auftreten tiefer Konvektion verstärkt und die Front deutlich beschleunigt. In der letzten Phase erzeugt die Verdunstung von fallendem Niederschlag Kaltluftbereiche in der Grenzschicht und beschleunigt dadurch die Frontenwanderung zusätzlich. Die klassische Theorie zur Ausbreitung von mesoskaligen Zirkulationen versagt bei der Berücksichtigung der zweiten Phase und wird um den konvektiven Massenfluss ergänzt. Die neue Theorie ist im Einklang mit den Ergebnissen aus hochaufgelösten Large-Eddy Simulationen.

Im letzten Teil dieser Dissertation untersuchen wir inwieweit konvektiver Niederschlag auf längeren Zeitskalen dazu beiträgt die Landoberfläche zu homogenisieren. Sensitivitätsstudien zeigen, dass das Eindringen von Niederschlag in den Boden die turbulenten Oberflächenflüsse im Modellgebiet homogenisiert. Allerdings ist diese Homogenisierung nicht stark genug, um eine statische Oberflächenheterogenität innerhalb von zwei Wochen vollständig zu unterdrücken. Zusätzlich zeigt das Energiespektrum

der Oberfläche kurzfristig eine deutliche Homogenisierung während dem Auftreten von Kaltlufttropfen aus verdunstetem Niederschlag.
Insgesamt kann festgestellt werden, dass Oberflächenheterogenitäten langfristig die Struktur der Grenzschicht und die Entwicklung von Konvektion in ihrer Umgebung beeinflussen. Im Gegensatz dazu wirkt tiefe Konvektion und damit einhergehender Niederschlag homogenisierend auf die Landoberfläche und beschleunigt insbesondere die Ausbreitung von mesoskaligen Zirkulationssystemen, die durch Oberflächenheterogenitäten entstanden sind. Die simulierten Effekte werden in gängigen Wetter- und Klimamodellen nicht berücksichtigt.

Contents

Abstract **i**

Zusammenfassung **iii**

1 Introduction **1**

- 1.1 Motivation . . . 1
  - 1.1.1 Moist Convection in the Earth System . . . 1
  - 1.1.2 Land-Atmosphere Interactions . . . 2
  - 1.1.3 Moist Convection over Heterogeneous Surfaces . . . 4
  - 1.1.4 The Parameterization Problem in Large-Scale Models . . . 5
- 1.2 Research Objective . . . 6
- 1.3 Outline . . . 9

2 The Modeling Framework **11**

- 2.1 The Large-Eddy Simulation Model . . . 11
- 2.2 The Land Surface Model . . . 13
  - 2.2.1 Surface Energy Balance . . . 13
  - 2.2.2 Soil Model . . . 16
  - 2.2.3 Surface Runoff Model . . . 18
  - 2.2.4 Additional Remarks . . . 18
- 2.3 Validation . . . 20
  - 2.3.1 Dry Convective Boundary Layer . . . 20

3 The Influence of Land Surface Heterogeneities on Cloud Size Development **25**

- 3.1 Introduction . . . 25
- 3.2 The Experiment Setup . . . 28
- 3.3 Main Features and Transition Times . . . 29
- 3.4 The Cloud Size Distribution . . . 35
- 3.5 Mechanisms Generating the Cloud Size Distribution . . . 38
- 3.6 Summary and Discussion . . . 44

4 The Effect of Moist Convection on Thermally Induced Mesoscale Circulations 47
4.1 Introduction 47
4.2 Methodology 49
4.2.1 Model Setup 49
4.2.2 Experiment Setup 50
4.3 Results from Large-Eddy Simulations 52
4.3.1 The Role of Clouds 55
4.3.2 The Role of Cold Pools 59
4.4 Extension of the Density Current Formulation 61
4.4.1 Theory 61
4.4.2 Application to LES Results 64
4.5 Summary and Discussion 66

5 The Interaction Between Static and Dynamic Land Surface Heterogeneities 69
5.1 Introduction 69
5.2 Methodology 71
5.2.1 Large-Eddy Simulation Setup 71
5.2.2 Initial Conditions and Experiment Design 71
5.3 Equilibrium Characteristics of Convection over Inhomogeneous Land Surfaces 74
5.4 From Heterogeneous Towards Homogeneous Land Surface Fluxes 76
5.5 Summary and Discussion 82

6 Summary and Conclusions 85

7 Outlook 91
7.1 Ideas for Parameterization Development 92
7.2 The Use of Observations 93
7.3 Land-Atmosphere Interactions in a Warmer Climate 94

References xviii

Acronyms xix

List of Figures xxv

List of Tables xxv

Acknowledgements xxvii

Chapter 1

Introduction

1.1 Motivation

1.1.1 Moist Convection in the Earth System

Convection is the fundamental process to transport heat at the surface into the free atmosphere. This vertical transport often involves condensation processes on a wide range of scales, commonly referred to as moist convection. Moist convection plays a central role for weather and climate because of its influence on energy and water cycles (Stevens and Bony, 2013). The complexity of moist convection introduces large uncertainties into weather and climate models (Bechtold et al., 2004; Bony and Dufresne, 2005; Flato et al., 2013; Sherwood et al., 2014). The scales of moist convection range from shallow boundary layer clouds to large mesoscale convective systems. We define convection with a vertical extent below 5 km as shallow convection and beyond 5 km as deep convection. Shallow convection is abundant in the atmosphere and often found in regions of large-scale subsidence (see Siebesma, 1998, for a review). These shallow clouds are important for the overall cloud cover and vertical moisture transport because of their frequent occurrence. Under unstable conditions, shallow convective clouds grow in size and transition to deep convection. Understanding of this transition process is key to predict the occurrence of deep convection (Kuang and Bretherton, 2006; Wu et al., 2009; Hohenegger and Stevens, 2013). Deep convection is characterized by strong vertical motions, mixed phase cloud particles and the formation of intense precipitation. The precipitating stage is accompanied by cold pools (cold downdrafts) from evaporation and melting of hydrometeors (Srivastava, 1987; Rotunno, 1988; Tompkins, 2001). Cold pools also support the organization of deep convection into larger systems (Seifert and Heus, 2013). Convective systems larger than 25 km are often called mesoscale convective systems. While these large systems occur less frequently, they exhibit the highest precipitation rates, account for much of the warm season precipitation and are cause for severe weather events (Fritsch et al., 1986; Mathon et al., 2002).

It has long been known that the occurrence of convection over land is fundamentally different from that over ocean. For instance, satellite measurements show that the intensity of convection is much stronger over land (Zipser et al., 2006). What is so different between land and ocean? An important difference is that land surfaces have much smaller heat capacities, allowing for higher variability of available surface energy. This is the fundamental reason why interactions between land surface and atmosphere can develop on short timescales, whereas interactions between the ocean surface and the atmosphere are buffered by the oceans' slowly varying surface temperature. As a consequence, in absence of large-scale synoptic perturbations, convection over land develops a pronounced diurnal cycle where convective activity is directly linked to the available surface energy. Such conditions are prevailing especially during mid-latitude summertime, in semi-arid subtropical and in tropical areas. In addition, the ocean provides an infinite moisture reservoir, whereas over land, moisture is limited and evapotranspiration is often not at its potential rate.

Another difference between land and ocean is the fact that the ocean surface is, to a first approximation, homogeneous, while the land surface is not. Natural land surface heterogeneities involve the distribution of vegetation and soil characteristics, soil moisture, lakes and rivers, as well as ice and snow. In addition, human activity has a direct influence on these distributions. Anthropogenic land-use changes often create distinct vegetation boundaries by deforestation, crop plantation or irrigation. The inhomogeneity of the land surface might be part of the reason why convection over land occurs so differently compared to convection over the ocean. This motivates a detailed analysis of the interaction between land surface heterogeneities and moist convection.

1.1.2 Land-Atmosphere Interactions

At the Earth surface, incoming radiation is absorbed and converted into thermal and latent heat. The surface energy balance regulates the partitioning of energy fluxes between the surface skin layer, the atmosphere and the soil (Fig. 1.1). While the primary energy exchange happens directly between the surface layer and the atmosphere, the soil helps to buffer part of the energy fluctuations at the surface. The energy exchange is controlled by the atmospheric state but also, and especially over land, by surface characteristics. The turbulent energy exchange with the atmosphere is limited by the aerodynamic surface resistance, which is minimized under conditions of weak atmospheric stability, high wind speeds and large roughness length. Early work revealed the important role of plant physiology and soil properties on the evapotranspiration (Penman, 1948; Monteith, 1965). Despite atmospheric temperature, humidity, and radiation, the surface resistance to evapotranspiration depends on the plant physiology (e.g. the leaf area index, the root properties, and the wilting point), the soil properties (e.g. porosity), and the soil moisture. Under conditions of sufficient soil moisture, forests typically exhibit much higher evapotranspiration rates than grassland because

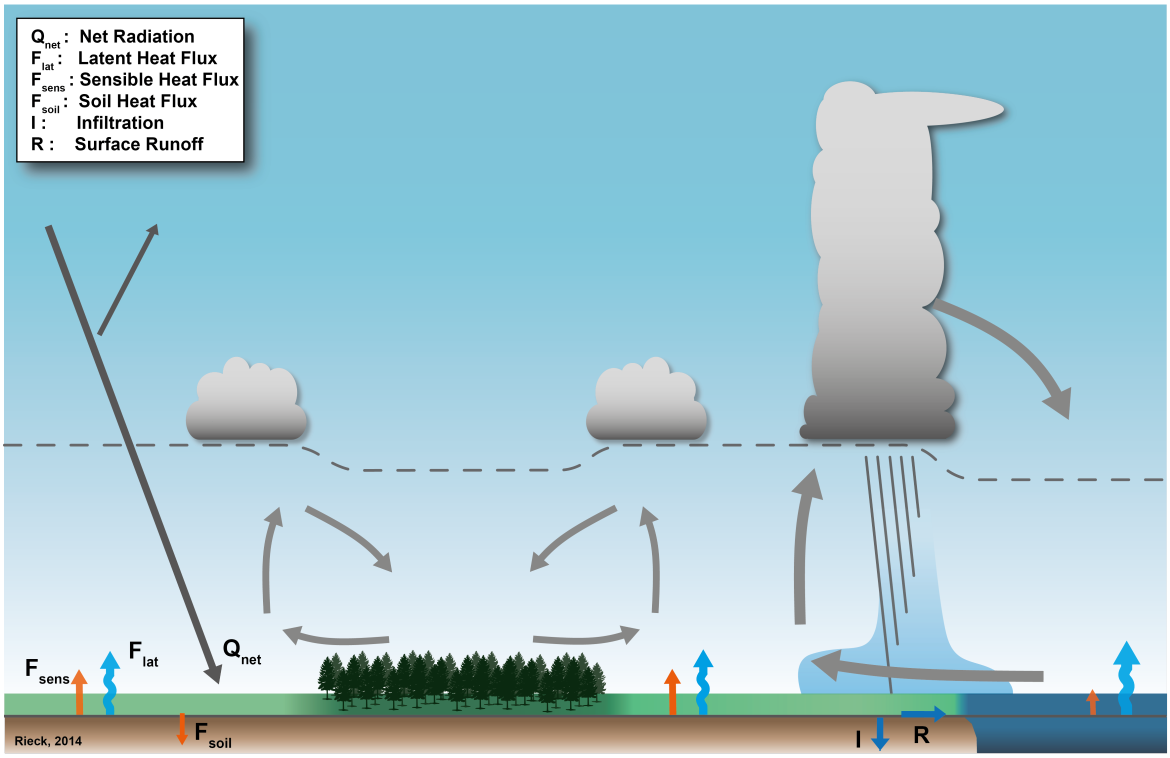
Q_{net} : Net Radiation
F_{lat} : Latent Heat Flux
F_{sens} : Sensible Heat Flux
F_{soil} : Soil Heat Flux
I : Infiltration
R : Surface Runoff
F_{sens}
F_{lat}
Q_{net}
F_{soil}
I
R
Rieck, 2014

Figure 1.1: Illustration of the components of the surface energy balance and the main interactions between the surface and the atmosphere. The dashed line represents the atmospheric boundary layer. The arrows at the surface represent the surface exchange of energy and water, whereas the arrows in the boundary layer represent surface induced mesoscale circulations. Q_{net} is the net radiation at the surface, F_{lat} the surface latent heat flux, F_{sens} the surface sensible heat flux, F_{soil} the soil heat flux, I the infiltration of precipitation, and R the surface runoff.

of their larger leaves and deeper roots. Soil moisture also controls evapotranspiration in a wide range of surface conditions (soil moisture limited regime), whereas the evapotranspiration becomes independent of soil moisture beyond a critical value close to the field capacity (energy limited regime) (Koster et al., 2004; Seneviratne et al., 2010).

Despite their temporal variability, we define some land surface properties as static because they do not change much during typical convective timescales and beyond, $\mathcal{O}(days)$. Static properties include surface albedo, surface roughness, leaf area index, and soil type. In contrast, we define soil moisture as a dynamic surface property because it changes on shorter timescales due to infiltration of precipitation and due to the history of evaporation. Since the surface is generally inhomogeneous we differentiate between static and dynamic heterogeneities analogously. In addition, clouds also induce dynamic surface heterogeneities by shading the Earth surface. Unlike soil moisture, cloud shading exhibits only weak memory, because the surface heat capacity is small.

1.1.3 Moist Convection over Heterogeneous Surfaces

The presence of surface heterogeneities creates horizontal gradients of temperature and humidity at the surface and in the boundary layer. These gradients drive atmospheric circulations, so called mesoscale circulations (Fig. 1.1). Early studies recognized the importance of mesoscale circulations on the local and regional climate (Pielke and Avissar, 1990). While the most prominent examples occur at the boundary between land and ocean (Crosman and Horel, 2010), mesoscale circulations are abundant in the atmosphere and may develop even under weak land surface discontinuities (Segal and Arritt, 1992).

Using high-resolution numerical modeling, mesoscale circulations have been identified to influence not only the boundary layer (Avissar and Schmidt, 1998) but also the development of shallow convection (Van Heerwaarden and Vilà-Guerau de Arellano, 2008; Garcia-Carreras et al., 2011; Huang and Margulis, 2012). These studies revealed that mesoscale circulations create convergence and force convective clouds especially in cases with large heterogeneity amplitudes. Early observational studies using satellite data support the connection between the occurrence of shallow cumulus clouds, mesoscale circulations and the underlying surface characteristics (Rabin and Stensrud, 1990; Cutrim et al., 1995). Both studies indicate that cumulus clouds organize over deforested areas with a buoyancy advantage. This confirms the idea that shallow convection depends on surface characteristics and motivates further studies.

Observations also indicate a higher potential for deep convection over inhomogeneous boundary layers (Wakimoto, 1982; Taylor et al., 1997; Zhang and Klein, 2010). These boundary layer perturbations are caused by surface heterogeneities and give observational evidence that deep convection can also depend on surface characteristics (Taylor et al., 1997). Three-dimensional high-resolution modeling of deep precipitating convection over heterogeneous land surfaces has gained less attention. Due to limited computing resources, partially two-dimensional simulations with coarse resolution have been performed (see Pielke, 2001, for a review). While these simulations did not fully resolve the evolution of convective clouds, they still bear interesting results. Lynn et al. (1998), for example, found an increase of domain accumulated precipitation with surface patch size, while in a later study, they could not reconfirm this linear relationship (Lynn et al., 2001). In a recent high-resolution study, Kang and Bryan (2011) simulated the transition from shallow to deep convection and found a faster transition over surfaces with a strong heterogeneity amplitude. Their study uses high resolution to fully resolve moist convection, but prescribed constant surface fluxes. However, interactive land surface models allow for feedbacks between the land and the atmosphere, e.g. the shading of the Earth surface by clouds, the infiltration of precipitation and near surface cooling by cold pools. To our knowledge, no three-dimensional simulations of deep convection at high resolution and with interactive heterogeneous land surface have been performed. In this dissertation, an interactive land surface model is coupled to a high-resolution large-eddy simulation, which allows to explicitly resolve moist convection and its interaction with the land surface.

The above-mentioned studies investigate atmospheric feedback mechanisms in response to heterogeneous land surface characteristics on small spatiotemporal scales. Despite these small scales, large-scale land-cover changes may also affect the global climate through biogeophysical and biogeochemical feedbacks. Long before Williams (2002) named the Amazon the "green ocean", several studies demonstrated that Amazonian deforestation may cause profound changes in regional and global climate (Shukla et al., 1990; Dickinson and Kennedy, 1992; Zhang et al., 1996; Claussen et al., 2001). For instance, Zhang et al. (1996) reported that land cover changes in various regions cause different effects on regional climate. While the Amazonian forest was identified as a hotspot for land-atmosphere interactions, the Asian monsoon climate was less sensitive to land cover changes. Other studies found a particular dependence of the Asian monsoon on land cover changes (McGuffie et al., 2007). Recently, extreme deforestation experiments with a coupled Earth system model revealed that forests exert a cooling in the tropics but a warming in high latitudes (Bathiany et al., 2010). The interactions between land and atmosphere involve biogeochemical feedbacks acting on long spatiotemporal scales, but also biogeophysical feedbacks acting on smaller spatiotemporal scales. Global climate models cannot fully resolve the latter scales and induce uncertainty into climate predictions (see Section 1.1.4). In this dissertation, we study the small spatiotemporal scales of the coupling between the heterogeneous land surface and moist convection to understand related mechanisms. The knowledge of physical mechanisms on a local scale helps to understand problems in numerical weather prediction models, but also in larger scale climate models.

1.1.4 The Parameterization Problem in Large-Scale Models

How is surface heterogeneity treated in numerical models? In current weather and climate models both land surface heterogeneity and moist convection are often not resolved and have to be parameterized. A direct interaction between land surface heterogeneity and moist convection is generally not considered. Instead, two main approaches exist to account for sub-grid land surface heterogeneity effects on the grid-scale surface energy exchange. First, the surface fluxes can be obtained by aggregation of fluxes for each sub-grid tile (Avissar and Pielke, 1989), or second by aggregation of surface parameters and subsequent calculation of the surface energy balance (Noilhan and Lacarrere, 1995). Both approaches are applicable in large scale models to obtain grid-scale surface fluxes (Koster and Suarez, 1992) and may be extended using blending height theory (Wieringa, 1986; Claussen, 1991). While the above-mentioned approaches are successfully applied to calculate the averaged surface fluxes, they exclude sub-grid variability induced by surface heterogeneity and especially its effect on convection.

All numerical models have to parameterize the effect of moist convection to a certain degree. Even high-resolution large-eddy simulation models with explicit convection have to parameterize microphysical processes. Numerical weather prediction and climate models typically employ a parameterization for moist convection. The principle idea of parameterizations is to describe sub-grid processes by resolved grid-scale quantities. In order to develop such parameterizations, physical understanding needs to be established to formulate relationships for the contribution of unresolved scales to the large-scale state. Since the early days of global modeling, parameterizations have been introduced to account for unresolved convective processes (Manabe and Strickler, 1964; Kuo, 1965). Since then, different convection parameterizations have been developed, including statistical plume models (Arakawa and Schubert, 1974) and bulk mass-flux models (Tiedtke, 1989). Because the nature of convection is a continuous process, advanced statistical approaches offer promising alternatives. First steps in this direction are taken by a unified eddy diffusivity mass flux approach (Neggers, 2009) and stochastic schemes with spectral cloud distribution (Plant and Craig, 2008; Sakradzija et al., 2014). In these schemes the convective ensemble is prescribed by probability density functions (PDF). Assumptions have to be made to prescribe the PDFs of convective cloud base mass flux or cloud size. It is therefore important to understand the distribution of these properties for parameterization development. Surface heterogeneities may contribute to the shape of the PDFs by modification of the convective ensemble through land-atmosphere interactions. This is important in coarser resolution numerical weather prediction and climate models (10-100 km) with parameterized convection because structures often originate at scales that are unresolved. Additional complication arises in the ”grey-zone” (1-10 km) because convection is partially resolved and partially parameterized (Pearson et al., 2014). Despite the higher resolution within this ”grey-zone”, the representation of moist convection and land-atmosphere interactions is still questionable since convection and related circulations are neither fully resolved nor correctly parameterized. Land-surface interactions induce further complications. For example, Hohenegger et al. (2009) found that the feedback between soil moisture and precipitation depends on the treatment of convection. Because moist convection is such a complex process to parameterize, it induces large uncertainties into weather (Bechtold et al., 2004) and climate predictions (Bony and Dufresne, 2005; Flato et al., 2013). This means that for both, high-resolution weather and climate models, process understanding at cloud resolving scales is required to develop future parameterizations and motivates the following research objective.

1.2 Research Objective

The overall goal underlying this dissertation is to improve the understanding of the interactions between surface heterogeneity, (deep) moist convection and related circulations, and to derive relationships among them. We split the interaction between

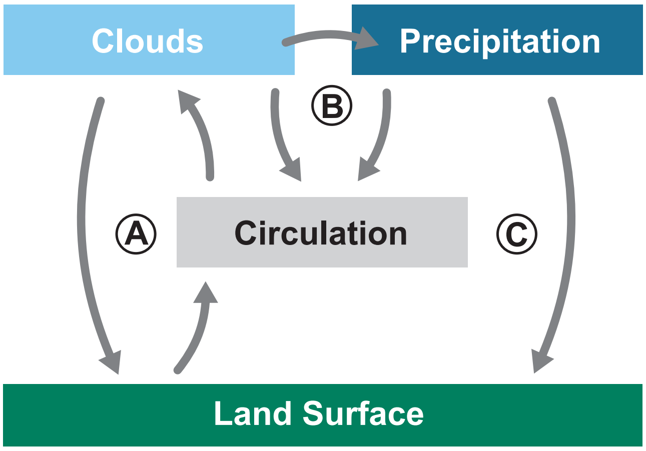

Figure 1.2: Illustration of the interactions studied in this dissertation.

these three components into three main cycles (Fig. 1.2). A), the influence of the land surface on convective clouds via the atmospheric circulation and the feedback of convection back on the surface. B), the effect of clouds and precipitation on the atmospheric circulation. And finally C), the effect of precipitation on the land surface. In order to address these problems we need to disentangle the possible feedbacks of the different cycles. This requires insights into processes at small scales that are unresolved in current weather and climate models. For this purpose, we use large-eddy simulations (LES) at 100 m resolution to resolve both shallow and deep convective clouds. Historically, LES has mostly been used to study equilibrium convection over the ocean. Therefore, a land surface model has to be implemented into a LES model to establish the link between land surface heterogeneities and moist convection. The implementation of a land surface model is crucial to obtain a correct surface energy balance and to represent the feedbacks between land and atmosphere. The implementation and validation of the new land surface scheme is part of this dissertation and is described in Chapter 2. Given this advanced modeling framework, we study the interactions between the land surface, mesoscale circulations, clouds and precipitation (Fig. 1.2) by raising the following four research questions.

What Determines the Cloud Size Distribution over Land?

The cloud size is key to predict cloud and precipitation development in future convection parameterizations. Over land, the cloud size distribution may be strongly affected by the interactions between a heterogeneous land surface, the atmospheric circulation and convective clouds (A in Fig. 1.2). We are thus interested to understand how the surface patch size can influence the size of convective clouds and whether we can derive any relationship between the two length scales. This research question is addressed using idealized LES simulations by systematically varying the surface patch size. The cloud size evolution is analyzed and PDFs of cloud size are derived. It is unclear whether such PDFs show a similar behavior as found over homogenous surface conditions (Neggers et al., 2003; Heus and Seifert, 2013). The development of the cloud spectrum also determines the transition from shallow to deep convection, which motivates the following question.

Does the Transition Time from Shallow to Deep Convection Depend on the Size of Land Surface Heterogeneity?

The transition from shallow to deep convection is the fundamental process to capture a correct diurnal cycle of convection. Several studies have addressed this problem from different perspectives but mostly over homogeneous ocean and land surfaces (Khairoutdinov and Randall, 2006; Wu et al., 2009). Current weather and climate models have difficulties in predicting a correct diurnal cycle over land. Models with fully parameterized convection typically depict a too early onset of convection (Bechtold et al., 2004), while models with partly resolved convection show a too late onset (Petch et al., 2002). Over land, heterogeneity effects may accelerate or slow down the transition process, thus possibly affecting the timing of the diurnal cycle of convection. We are therefore interested to understand the transition process under different surface patch sizes. For this purpose, a simple relationship between patch size and the transition time would be of great value. This question is addressed by analyzing idealized LES experiments as described for the previous question.

What are the Impacts of Precipitating Convection on the Characteristics of Surface Induced Circulations?

The previous two questions focus on the effect of surface heterogeneity on convection, where mesoscale circulations act as links between the two. While mesoscale circulations are induced by land surface heterogeneities (Avissar and Schmidt, 1998), the circulation may in turn be modified by moist convection and subsequent precipitation. This is the second feedback cycle we are going to address in this dissertation (B in Fig. 1.2). Sea or vegetation breezes are typical examples of surface induced circulations (Crosman and Horel, 2010). Under weak synoptic forcing, the breeze front propagates from the colder into the warmer region. Linear theory has been used to quantify the propagation speed of such density currents in a dry atmosphere (Rotunno, 1988). Given the strong influence of moist convection on its environment, it is conceivable that convection may influence the circulation and in particular its propagation. The goal of this study is to isolate and quantify the effect of convection on the characteristics of the circulation. This will include the cloud circulation as well as the cold pool circulation induced by precipitation evaporation. Both effects are not fully resolved in weather and climate models and may thus introduce biases in the strength and propagation of mesoscale systems. A conceptual theory for the propagation of mesoscale systems over homogeneous surfaces has been proposed by (Rotunno, 1988), but is still missing for mesoscale circulations induced by land surface heterogeneity. We formulate an extension of the propagation theory for mesoscale circulations over heterogeneous land surfaces.

Can Precipitating Convection Homogenize the Surface Fluxes over Heterogeneous Land Surfaces?

To address this question we increase the complexity of land-atmosphere interactions and include the modification of the land surface by the infiltration of precipitation (C in Fig. 1.2). The incorporation of this effect induces dynamic surface heterogeneity because soil moisture has a direct control on the surface energy balance through evapotranspiration. Depending on its occurrence, surface precipitation may either increase or dampen the heterogeneity of the surface fluxes. Studies with cloud resolving models revealed the buoyancy excess and surface heterogeneity at the mesoscale (10-50 km) as key factors for a strong coupling between soil moisture and precipitation (Findell and Eltahir, 2003; Clark and Taylor, 2004; Schlemmer et al., 2012). Previous studies have only looked at this coupling in connection with either static or dynamic surface heterogeneities but did not isolate the interaction between the two. In this study, we test a homogenization of a preexisting static surface heterogeneity (different vegetation characteristics) by precipitation infiltration into the soil. In order to homogenize the surface fluxes, precipitation has to fall on the patches with low evapotranspiration. The precipitation process acts on longer timescales because soil moisture introduces memory through the history of precipitation events. Optimal conditions for this effect are chosen to assess the potential of a homogenization of the land surface. LES simulations are integrated for two weeks of simulation time to understand the surface response to precipitation infiltration.

1.3 Outline

The following chapters focus on the above stated research questions. Each chapter has a separate and detailed introduction and discussion part and may thus be read independently. The dissertation outline is as follows:

Chapter 2 In this chapter, the modeling framework is established. A particular focus is on the formulation of the implemented land surface model. This helps understanding the coupling between land surface and atmosphere, which is important for the feedback with moist convection. The land surface formulation is validated for an experiment with a simple dry convective boundary layer over a homogeneous land surface.

Chapter 3 The modeling framework is applied to study cloud development over different heterogeneous land surfaces. The effect of the land surface on the cloud size distribution (question 1) and the transition to deep convection (question 2) are the major topics of this chapter.

Chapter 4 The role of moist convection on a thermally induced mesoscale circulation is investigated (question 3). High resolution LES simulations in an idealized setup with a 800 km wide channel are used. The LES results are applied to advance classical density current theory to a case of a density current interacting with precipitating convection.

Chapter 5 In this chapter, long-term LES simulations are analyzed to investigate under which conditions an initially heterogeneous land surface can be homogenized (question 4).

Chapter 6 The last chapter summarizes our findings by revisiting the research questions stated in this introduction. Separate conclusions are given for each question as well as a general evaluation of this work.

Chapter 7 We end with an outlook on how to proceed with parameterization development and process understanding from models and observations. Finally, we propose to study land-atmosphere interactions in a warmer climate.

Chapter 2

The Modeling Framework

The concept of numerical modeling has become an important part of modern meteorology. The cascade of numerical models ranges from global coarser resolution models to local high-resolution models. Global circulation models (GCM) operate at horizontal resolutions of several hundreds of km, regional cloud resolving models (CRM) operate at resolutions of several km whereas high resolution large-eddy simulation (LES) operate at horizontal resolutions of 10-100 m. Recently, direct numerical simulation with horizontal resolution of few cm have become feasible.

LES was introduced to explicitly resolve parts of the turbulent motion to avoid the use of parameterizations needed at coarser resolution. LES typically operates at horizontal resolutions considerably smaller than the boundary layer height and employs sub-grid parameterizations only for turbulence from small eddies, microphysics and radiation. Thus the major advantage over CRMs is the explicit treatment of the large energy containing eddies and the explicit simulation of clouds and convection. Because the grid size is typically smaller than the size of shallow convective clouds, LES also captures the transition from shallow to deep clouds more accurately than larger scale models. In this chapter, we introduce the LES-modeling framework with a focus on the newly implemented land surface model and its validation.

2.1 The Large-Eddy Simulation Model

The University of California Los Angeles - Large-Eddy Simulation (UCLA-LES) model (Stevens et al., 2005; Savic-Jovcic and Stevens, 2008) is used. The model solves the

LES-filtered equations of motion:

$$\begin{aligned}
\frac{\partial \bar{u}_i}{\partial t} &= -\bar{u}_j \,, \frac{\partial \bar{u}_i}{\partial x_j} - c_p \Theta_0 \frac{\partial \bar{\pi}}{\partial x_i} + \frac{g \bar{\theta}_v''}{\Theta_0} \,, \delta_{i3} + \frac{1}{\rho_0} \frac{\partial(\rho_0\, \tau_{ij})}{\partial x_j} + F_i, && (2.1)\\
\frac{\partial \bar{\theta}_l}{\partial t} &= -\bar{u}_j \frac{\partial\, \bar{\theta}_l}{\partial x_j} + \frac{1}{\rho_0} \,, \frac{\partial(\rho_0\, SGS_{u_j,\theta_l})}{\partial x_j} + S_{\theta_l}, && (2.2)\\
\frac{\partial \bar{q}_t}{\partial t} &= -\bar{u}_j \frac{\partial\, \bar{q}_t}{\partial x_j} + \frac{1}{\rho_0} \,, \frac{\partial(\rho_0\, SGS_{u_j,q_t})}{\partial x_j} + S_{q_t}, && (2.3)\\
\frac{\partial(\rho_0 \bar{u}_i)}{\partial x_i} &= 0, && (2.4)
\end{aligned}$$

on a three-dimensional grid in the anelastic limit, where overbars denote the LES-filtered mean prognostic variables. θ_l is the liquid water potential temperature, q_t the total water mixing ratio, $\bar{\pi}$ the Exner function, Θ_0 the basic state background potential temperature and $\bar{\theta}_v''$ its deviation from the basic state. The sub-grid momentum flux is denoted by τ_{ij}, which is parameterized using the Smagorinsky closure. F_i represents additional forcings, such as the Coriolis force or other synoptic scale forcings. The conservation of scalar quantities (θ_l, q_t) is given by advection, sub-grid scale scalar fluxes ($\mathrm{SGS}_{u_j,\varphi} = \overline{u_j \varphi} - \bar{u}_j \bar{\varphi}$) and other sources or sink terms (S_φ).

The model operates in the LES limit ranging from a few meters to hundreds of meters where large eddies are typically resolved. The time integration is performed using a third order Runge-Kutta scheme with a variable time step depending on the Courant-Friedrich-Lewy (CFL) criterion. Lateral boundary conditions are cyclic, whereas the model top is buffered with a damping layer to absorb upward propagating gravity waves. The bottom boundary conditions are parameterized by sub-grid scale surface fluxes, more details are given in Section 2.2.1.

The UCLA-LES has been widely used to study a variety of problems, from purely dry to moist convective environments, including well-established cases for shallow cumulus such as RICO (VanZanten et al., 2011), BOMEX (Cheng et al., 2010) and stratocumulus convection such as DYCOMS (Stevens et al., 2005). Most of these cases require only warm-rain microphysics, prescribed radiation, and use simple surface parameterizations.

However, to ensure suitable model physics for the simulation of deep convection, more comprehensive schemes are required to parameterize cloud microphysics and radiation. The two-moment mixed-phase microphysics scheme of Seifert and Beheng (2005) including prognostic equations for cloud water, rain, ice, graupel, hail and snow is used to include the formation of ice in deep convective clouds into UCLA-LES.

The radiative transfer is modeled with a delta four-stream method following Pincus and Stevens (2009). In this context, the radiation model has been updated to represent the effects of ice clouds on radiative properties following Fu and Liou (1993).

This modeling framework has been tested and successfully applied to simulate the transition to deep convection over oceanic tropical areas in Hohenegger and Stevens

(2013) and to simulate the diurnal cycle of continental mid-latitude areas using prescribed surface fluxes in Schlemmer and Hohenegger (2014). In the next section, we introduce a new land surface model into the UCLA-LES, which will allow us to study land-atmosphere interactions.

2.2 The Land Surface Model

The parameterization described in this section computes the sub-grid surface fluxes of latent and sensible heat, which serves as the bottom boundary conditions for the LES. For the purpose of this study, the UCLA-LES has been coupled to a land surface model (LSM). The LSM is adopted from the Dutch Atmospheric LES (DALES) as described in Heus et al. (2010), which is derived from the ECMWF-IFS land surface scheme. The LSM consists of two main parts: A solver for the surface energy balance and a four-layer soil scheme.

2.2.1 Surface Energy Balance

We solve the surface energy balance (Eq. 2.5) for each grid cell at every time step to calculate the fluxes between the land at the atmosphere.

$$C_{\mathrm{surf}} \, \frac{dT_{\mathrm{surf}}}{dt} = Q_{\mathrm{net}} - F_{\mathrm{sens}} - F_{\mathrm{lat}} - F_{\mathrm{soil}} \tag{2.5}$$

The surface energy balance is solved for a skin layer, which is introduced to couple the atmosphere to the soil model. The surface temperature is represented by T_{surf}, while C_{surf} is the heat capacity of the skin layer. Q_{net} denotes the net surface energy that is the sum of the net short and longwave radiation at the surface.

The sensible and latent heat flux, F_{sens} and F_{lat}, are computed using a classical resistance formulation (e.g. Stensrud, 2007):

$$F_{\mathrm{sens}} = \frac{\rho \; c_{\mathrm{p}}}{r_{\mathrm{a}}} \; \left(\theta_{\mathrm{surf}} - \theta_{\mathrm{atm}}\right) \, , \tag{2.6}$$

$$F_{\mathrm{lat,x}} = \frac{\rho \; L_{\mathrm{v}}}{r_{\mathrm{a}} + r_{\mathrm{s,x}}} \; \left(q_{\mathrm{sat}}(\theta_{\mathrm{surf}}) - q_{\mathrm{atm}}\right) \, , \tag{2.7}$$

where θ_{surf} and θ_{atm} are the potential temperatures at the surface and at the first atmospheric model level, respectively. r_{a} is the aerodynamic resistance, $r_{\mathrm{s,x}}$ the surface resistance depending on whether the surface is covered with plants or bare soil, $q_{\mathrm{sat}}(\theta_{\mathrm{surf}})$ the saturation specific humidity at the surface, q_{atm} the specific humidity at the first atmospheric level, ρ the density of air, c_{p} the specific heat capacity of the air at constant pressure and L_{v} the specific heat of vaporization. In the applied formulation of the surface fluxes, latent and sensible heat is released when the temperature and moisture difference between the surface and the atmosphere becomes large. The resistance formulation is elucidated in the next section.

The surface soil heat flux, F_{soil}, is calculated following Duynkerke (1999):

$$F_{\mathrm{soil}} = \Lambda \left(T_{\mathrm{surf}} - T_{\mathrm{soil}} \right) , \tag{2.8}$$

where Λ is the bulk conductivity of the skin layer and T_{soil} the temperature of the uppermost soil layer. The formulation of the soil heat flux is similar to the one from the surface sensible heat flux but with a fixed bulk conductivity that describes the ability of the skin layer to conduct thermal heat.

The total evapotranspiration is calculated as the sum of the transpiration from plants, $F_{\mathrm{lat,veg}}$, the direct evaporation from liquid water on the vegetation, $F_{\mathrm{lat,liq}}$ and the evaporation from bare soil $F_{\mathrm{lat,soil}}$:

$$F_{\mathrm{lat}} = \alpha_{\mathrm{veg}} \left(1 - \alpha_{\mathrm{liq}}\right) F_{\mathrm{lat,veg}} + \alpha_{\mathrm{veg}}\ \alpha_{\mathrm{liq}}\ F_{\mathrm{lat,liq}} + \left(1 - \alpha_{\mathrm{veg}}\right) F_{\mathrm{lat,soil}} , \tag{2.9}$$

where α_{veg} is the surface fraction covered with vegetation and α_{liq} is the fraction of vegetated surface covered with liquid water. α_{veg} is a fixed parameter, whereas α_{liq} may change when water evaporates or condensates following:

$$\alpha_{\mathrm{liq}} = \frac{W_l}{LAI\ W_{\mathrm{l,max}}} , \tag{2.10}$$

$$\tag{2.11}$$

where LAI is the leaf area index, $W_{\mathrm{l,max}}$ the maximum liquid water and W_l the actual liquid water on the leaves, which is related to latent heat flux by:

$$\frac{dW_l}{dt} = \frac{F_{\mathrm{lat,liq}}}{\rho_w L_v} , \tag{2.12}$$

$$\tag{2.13}$$

where ρ_w is the density of water and L_v the specific heat of vaporization. In the current model version, W_l can only increase in case of dew fall when the surface latent heat flux becomes negative.

Resistance Formulation

We employ a classical resistance formulation to include the influence of the land surface and the atmospheric properties on the exchange of heat and moisture at the surface. The aerodynamic resistance, r_a, that limits the exchange of heat and moisture at the surface is defined as:

$$r_a = \frac{1}{C_h\ u} , \tag{2.14}$$

where C_h is the drag coefficient for heat and u the absolute wind speed at the lowest model level. In situations when the air near the surface is unstable and the surface winds are strong, the aerodynamic resistance is small and promotes a fast exchange of heat moisture between the surface and the atmosphere. On the other hand, small wind speeds or stable conditions reduce the ability of the surface to release latent or sensible heat. Monin-Obukhov similarity theory (Louis, 1979) is used to calculate the surface drag coefficient:

$$C_h = \frac{\kappa}{\left[ln(\frac{z_{\mathrm{sl}}}{z_{0m}}) - \Psi_m \frac{z_{\mathrm{sl}}}{L} + \Psi_m \frac{z_{0m}}{L}\right] \left[ln(\frac{z_{\mathrm{sl}}}{z_{0h}}) - \Psi_h \frac{z_{\mathrm{sl}}}{L} + \Psi_h \frac{z_{0h}}{L}\right]} \;, \tag{2.15}$$

where κ is the von Kármán constant, $\mathrm{z_{0h}}$ and $\mathrm{z_{0m}}$ the roughness length for heat and momentum and $\mathrm{z_{sl}}$ the surface layer depth (which is typically the lowest 10% of the atmospheric boundary layer). The Monin-Obukhov length, L, which defines the atmospheric stability is computed using an iteration method and Ψ_h and Ψ_m denote the integrated stability functions for momentum and heat (Beljaars and Holtslag, 1991).

The surface resistance, $r_{\mathrm{s,x}}$, describes the effect of the surface on evapotranspiration. Under the same energy and atmospheric conditions, the presence of soil and vegetation implies a smaller evapotranspiration than over a water surface. This is due to the retention of soil moisture caused by e.g. closed stomata of plants or soil porosity. The fraction of the surface that is covered with plants is described by the vegetation resistance, $r_{\mathrm{s,veg}}$ and the remaining part of the the surface covered with bare soil is described by the soil resistance, $r_{\mathrm{s,soil}}$. Both surface resistances are calculated following the Jarvis-Stewart parameterization (Jarvis, 1976).

The vegetation resistance is modeled as:

$$r_{\mathrm{s,veg}} = \frac{r_{\mathrm{s,veg,min}}}{LAI}\; f_1(S_{\mathrm{in}})\; f_2(\phi_{\mathrm{tot}})\; f_3(q_{\mathrm{sat}}, q_{\mathrm{atm}})\; f_4(T_{\mathrm{surf}}) \tag{2.16}$$

where $r_{\mathrm{s,veg,min}}$ is the minimum vegetation resistance, LAI is the leaf area index, f_1 is a function depending on the incoming shortwave radiation at the surface (S_{in}), f_2 is a function depending on the soil moisture content averaged over the root depth of the vegetation canopy (ϕ_{tot}), f_3 is a function depending on the water-vapor pressure deficit at the first atmospheric model level and f_4 is a function depending on the surface temperature. The four functions describe the effects of external parameters on the plant physiological properties and hence on the evapotranspiration.

The functions are given as:

$$f_1(S_{\mathrm{in}}) = \frac{1}{\min\left(1, \frac{0.004 S_{in} + 0.05}{0.81(0.004 S_{\mathrm{in}} + 1)}\right)} \;, \tag{2.17}$$

$$f_2(\phi_{tot}) = \frac{\phi_{\mathrm{fc}} - \phi_{\mathrm{wp}}}{\phi_{\mathrm{tot}} - \phi_{\mathrm{wp}}} \;, \tag{2.18}$$

$$f_3(q_{\mathrm{sat}}, q_{\mathrm{atm}}) = \frac{1}{\exp\left(g_D \left[q_{\mathrm{sat}}(T_{\mathrm{atm}}) - q_{\mathrm{atm}}\right]\right)} \;, \tag{2.19}$$

$$f_4(T_{\mathrm{surf}}) = \frac{1}{1.0 - 0.0016\,(298.0 - T_{\mathrm{surf}})^2} \;, \tag{2.20}$$

where ϕ_{fc} is the soil moisture at field capacity and ϕ_{wp} is the soil moisture at wilting point and g_D a correction factor that is only nonzero in high vegetation and T_{atm} the absolute temperature of the first atmospheric level. The evapotranspiration is favored under conditions of weak incoming radiation (to avoid drying-out of the vegetation when the incoming radiation is large), under wet soil conditions, under high surface temperatures and when the vapor-pressure deficit is large.

Analogous to the vegetation resistance, the bare-soil evaporation is also calculated with the resistance approach:

$$r_{\mathrm{s,soil}} = r_{\mathrm{s,soil,min}} \; f_2(\phi(z_1)) \ , \tag{2.21}$$

where $r_{\mathrm{s,soil,min}}$ is the minimum soil resistance depending on the soil type and f_2 a function depending on the soil moisture content of the uppermost soil level (z_1) which is in contact with the atmosphere (see Eq. 2.18). Larger evaporation from bare soil is promoted during wet soil conditions.

2.2.2 Soil Model

The skin layer is coupled to a four layer soil model to predict the soil moisture and soil temperature in time. The soil model solves a diffusion equation for the soil temperature:

$$C_{\mathrm{soil}} \, \frac{\partial T_{\mathrm{soil}}}{\partial t} = \frac{\partial}{\partial z} \left(\lambda \frac{\partial T_{\mathrm{soil}}}{\partial z} \right) \ , \tag{2.22}$$

where C_{soil} is the average soil heat capacity a function of the heat capacity of dry soil ($C_{\mathrm{soil,dry}}$) and water (C_{w}), and λ is the soil heat conductivity. The uppermost soil level is coupled to the skin layer to compute the surface soil heat flux, whereas the lowest soil layer is in contact with a deep soil temperature ($T_{\mathrm{soil,deep}}$) representative for the climatological mean. The soil layers can effectively store heat and moisture and therefore help to damp the system against an excessive exchange with the atmosphere.

The soil heat conductivity, λ, depends on the soil moisture content and is modeled following Peters-Lidard (1998):

$$\lambda = K_e(\lambda_{\mathrm{wet}} - \lambda_{\mathrm{dry}}) + \lambda_{\mathrm{dry}} \ , \tag{2.23}$$

where the conductivity of dry soil, λ_{dry}, is assumed constant and the conductivity of wet soil follows $\lambda_{\mathrm{wet}} = (\lambda_{sm})^{1-\phi_{\mathrm{sat}}} \, (\lambda_w)^{\phi}$, where λ_{sm} is the heat conductivity of the soil matrix and λ_w the thermal conductivity of water. K_e is the Kersten number, a weighting factor defined as:

$$K_e = log_{10} \left[max(0.1, \frac{\phi}{\phi_{\mathrm{sat}}}) \right] + 1 \ , \tag{2.24}$$

where ϕ is the volumetric soil moisture content and ϕ_{sat} the volumetric soil moisture at saturation. The soil moisture at saturation is larger than the soil moisture at field

	z_1	z_2	z_3	z_4
depth [m]	0.07	0.34	1.47	2.86
θ [K]	291.14	291.09	290.86	289.92
ϕ [m^3 m^{-3}]	0.273	0.274	0.276	0.335

Table 2.1: Default values of the depth, temperature and soil moisture for each soil level from top to bottom. The values are interpolated from the land surface scheme used in the COSMO model in Schlemmer et al. (2011).

capacity, because the soil moisture at field capacity is measured after excess water has drained away. The lowest model level is in contact with a constant deep soil temperature to represent a climatological mean state. The uppermost layer is coupled to the surface temperature (T_{surf}) determined from Eq. 2.5.

The soil moisture content is modeled with a differential equation describing the movement of water in unsaturated soils (Richards, 1931):

$$\frac{\partial \phi}{\partial t} = \frac{\partial}{\partial z}\left(\lambda_\phi \frac{\partial \phi}{\partial z} - \gamma_\phi\right) + S_\phi \ , \tag{2.25}$$

where γ_ϕ is the soil diffusivity, λ_ϕ the hydraulic conductivity and S_ϕ the sources and sinks. The lowest model level has a rigid lid to prevent soil moisture from draining away into deeper layers. The only process to reduce the soil moisture content is the surface evaporation, while an increase is only generated by surface precipitation (see next section).

The soil diffusivity and the hydraulic conductivity are defined following Clapp and Hornberger (1978):

$$\gamma_\phi = \gamma_{\phi,\text{sat}} \left(\frac{\phi}{\phi_{\text{sat}}}\right)^{2b+3} , \tag{2.26}$$

$$\lambda_\phi = -\frac{b\ \gamma_{\phi,\text{sat}}\ \psi_{\text{sat}}}{\phi_{\text{sat}}} \left(\frac{\phi}{\phi_{\text{sat}}}\right)^{b+2} , \tag{2.27}$$

where b is a dimensionless constant depending on the soil type, $\gamma_{\phi,\text{sat}}$ is the saturation hydraulic conductivity, ψ_{sat} is the matrix potential of water at saturation. The lower boundary condition of the soil model is prescribed by a climatological mean soil moisture.

The thickness of the soil layers decreases from the lowest level towards the surface (see Table 2.1). Because of the thin top soil layer and the small heat capacity of the skin layer, this setup is able to capture the fast interactions that arise between the land surface and the atmosphere. The soil neglects lateral exchange of heat and moisture but employs a surface runoff model which is discussed in the next section.

2.2.3 Surface Runoff Model

A runoff model is employed to determine the amount of surface precipitation that can penetrate into the uppermost soil layer. Especially in wet soil conditions and when precipitation rates are large, the runoff process can be important. For this purpose, a Simple Water Balance (SWB) model developed by Schaake et al. (1996) and validated in the Penn-State NCAR modeling system by Chen and Dudhia (2001) is implemented. The infiltration is bounded by the surface precipitation and the maximum amount of water the soil can hold:

$$I = min(I_{\mathrm{max}}, P_{\mathrm{surf}}) \tag{2.28}$$

where I is the actual infiltration into the uppermost soil level, I_{max} the maximum infiltration rate depending on the soil type and P_{surf} the surface precipitation rate.

The maximum infiltration is defined as:

$$I_{\mathrm{max}} = P_{\mathrm{surf}} \; \frac{D_x(1-e^{-\kappa\Delta\tau})}{P_{\mathrm{surf}} + D_x(1-e^{-\kappa\delta_i})} \; , \tag{2.29}$$

where $\Delta\tau$ is the model time step and κ is a constant defined as:

$$\kappa = \kappa_{\mathrm{ref}} \frac{\gamma_{\phi,\mathrm{sat}}}{\gamma_{\phi,\mathrm{ref}}} \; , \tag{2.30}$$

where κ_{ref} is a constant and $\gamma_{\phi,\mathrm{ref}}$ the reference soil diffusivity. In the present model setup, the time step of the infiltration model has been fixed to 2 s in order to avoid fluctuations in the infiltration rate induced by a variable time step of the LES model.

D_x is the average soil spare capacity over all vertical soil layers:

$$D_x = \sum_{k=1}^{k_{\mathrm{max}}} \left[\phi_{\mathrm{fc}}(k) - \phi(k)\right] \; \Delta z(k) \; , \tag{2.31}$$

where k_{max} is the number of soil layers, and Δz the thickness of each layer. The surface runoff model described in this section is only used in Chapter 5. It is only required for the study of convection on longer time scales, e.g several days or weeks.

2.2.4 Additional Remarks

The LSM presented in the previous sections requires the choice of several parameters that are held constant during the simulation period. Table 2.2 presents the default values of all parameters employed in this dissertation. The exact configuration and particularly the initialization of the soil temperature and moisture may vary between different simulations. In case it deviates from the default setting, the scenario is discussed in the corresponding chapter.

The LSM is coupled to the atmospheric radiation scheme through the radiative fluxes at the surface. The surface net radiation (Q_{net}) is averaged in time to avoid short-term

Variable	Explaination	Value	Unit
α_{veg}	Fraction covered with vegetation	1.0	-
α_{liq}	Fraction of vegetation covered with liquid	0.0	-
a	Surface albedo for radiation model	0.153	-
$z_{0\mathrm{h}}$	Roughness length for heat	0.025	m
$z_{0\mathrm{m}}$	Roughness length for momentum	0.1	m
$T_{\mathrm{soil,deep}}$	Deep soil temperature	283	K
$r_{\mathrm{s,veg,min}}$	Minimum vegetation resistance	150	s m^{-1}
$r_{\mathrm{s,soil,min}}$	Minimum soil resistance	50	s m^{-1}
C_{surf}	Skin layer heat capacity	20000	J
LAI	Leave area index	3.	-
LAI_{min}	Minimum leave area index	2.	-
LAI_{max}	Maximum leave area index	6.	-
$W_{\mathrm{l,max}}$	Maximum layer of liquid water on surface	0.0002	m
g_D	Vegetation response factor for vapor deficit	0	-
ϕ_{wp}	Volumetric soil moisture at wilting point	0.171	m^3 m^{-3}
ϕ_{fc}	Volumetric soil moisture at field capacity	0.323	m^3 m^{-3}
ϕ_{sat}	Volumetric soil moisture at saturation	0.472	m^3 m^{-3}
$C_{\mathrm{soil,dry}}$	Volumetric heat capacity of dry soil	2.19 10^6	J m^3 K^{-1}
C_w	Volumetric heat capacity of water	4.2 10^6	J m^3 K^{-1}
Λ	Bulk heat conductivity of skin layer	5	W m^{-1} K^{-1}
λ_{dry}	Heat conductivity dry soil	0.190	W m^{-1} K^{-1}
λ_{sm}	Heat conductivity soil matrix	3.11	W m^{-1} K^{-1}
λ_{w}	Heat conductivity water	0.57	W m^{-1} K^{-1}
b	Clapp and Hornberger exponent	6.04	-
ψ_{sat}	Matrix potential at saturation	-0.388	m
$\gamma_{\phi,\mathrm{sat}}$	Hydraulic conductivity at saturation	0.57 10^{-6}	m s^{-1}
$\gamma_{\phi,\mathrm{ref}}$	Reference soil diffusivity	0.285	m s^{-1}
κ_{ref}	Constant	-3.0	-
$\Delta\tau$	Time constant for runoff model	2	s

Table 2.2: List of default values of all land surface and soil parameters applied in this dissertation.

fluctuations in the surface temperature due to the use of Monte Carlo sampling in the radiation code, a problem described in Pincus and Stevens (2013). Given a background wind of e.g. 0.5 m s^{-1} and horizontal resolution of 100 m (as used in Chapter 3), we choose an averaging period of 100 s, which corresponds to a travel distance of 50 m (half the horizontal resolution).

Although the LSM includes the main interaction between the surface and the atmosphere, some surface and soil processes have been neglected. A detailed description of roots, groundwater runoff and interception water on the vegetation are, for example, not included. Further, the model has not been used in wintertime conditions and is therefore not designed to represent snow and ice processes at the surface. Despite these minor limitations, the LSM setup is well suited for the purpose of our studies because it captures the main interactions between the atmosphere and the land surface. The correct implementation of the LSM is tested in the next section.

2.3 Validation

The modeling framework described in Section 2.1 is compared to results from the Dutch Atmospheric Large-Eddy Simulation (DALES) for a case of a dry convective boundary layer. The land-surface model has also been tested for a case with fixed sea surface temperature and prescribed drag coefficients for a case of shallow cumulus convection over the ocean. In the following, we only focus on the case of a dry convective boundary layer.

Although DALES uses different parameterization packages, it solves the same filtered equations of motions as UCLA-LES, but assuming the Boussinesq approximation in contrast to the anelastic approximation used in UCLA-LES. DALES also employs the same land surface model as described above and is therefore used to test the correct implementation of the LSM into UCLA-LES. A detailed description of the DALES code is given in Heus et al. (2010). An important difference between the two models simulating dry convection is the treatment of sub-grid scale turbulence. DALES uses a prognostic TKE-based turbulence scheme, whereas UCLA-LES uses the Smagorinsky model to treat sub-grid scale fluctuations. Despite the discussed differences, both models took part in several inter-comparison case studies and showed similar results for moist convective cases (VanZanten et al., 2011; Blossey et al., 2013).

2.3.1 Dry Convective Boundary Layer

To compare the statistics of both models, an idealized case of a dry convective boundary (DCBL) coupled to an interactive but homogeneous land surface is simulated. Both models are run with the exact same initial conditions of the atmosphere and land surface. The atmospheric initial conditions are taken from the Cabauw measurement site in the Netherlands and resemble the structure of the atmosphere on a dry and cloudless day (van Heerwaarden et al., 2010). The selected case uses data recorded during 25 September 2003, a day without synoptic scale forcing. The initial profiles of temperature and humidity are denoted by dashed lines in Fig. 2.2. The temperature profile shows an inversion at about 800 m ($\Delta T = 3$ K), whereas the specific humidity is vertically homogeneous (q = 5.5 g kg^{-1}). The horizontal background wind is fixed at 2.5 m s^{-1}. The soil model is initialized as described in Table 2.1 but with a faster soil temperature decrease with depth, (T_{soil}: [290, 287, 285, 283 K]). The computational domain spans 64 × 64 × 96 points with a horizontal grid size of 50 m and a vertical grid size of 25 m. Both models are integrated for 5 hours of simulation time, starting at 8 local standard time (LST).

Note that the sensitivity of the results to the horizontal domain size has been tested for four different domain sizes (1.6, 3.2, 6.4 and 12.8 km). Generally, the domain size has a small influence on the presented quantities as long as eddies of the size of the boundary layer can be resolved and a sufficient number of eddy turnovers has been averaged (Sullivan and Patton, 2011). The presented domain size of 3.2 km proves to be a reasonable choice in this respect.

Experiments with Fixed Radiation

We start with fixed incoming net radiation at the surface, $Q_{\text{net}} = 450\ \text{W m}^{-2}$. The time evolution of the surface sensible and latent heat fluxes (Fig. 2.1a,b) are very similar in both models, the deviation of UCLA-LES averaged over the last 2 hours of simulation time is less than 5 % (F_{sens}: +1.67 %, F_{lat}: -4.33 %). Hence, the surface energy has been partitioned in a very similar way in both models. The small differences may be explained by the different computation of the surface drag coefficient in both models. This issue will be discussed again in the next section.

The vertical profiles of temperature and specific humidity depict a similar structure in both models (Fig. 2.2a,b,e,f). At the end of the simulations, the mixed layer temperature (moisture) differs by less than 0.1 K (0.1 g kg^{-1}) between the two models. Consequently, both models simulate almost the exact same growth rate of the convective boundary layer (Fig. 2.1c). The boundary layer height is defined as the height of the maximum vertical gradient in potential temperature. The growth rate is faster than suggested by classical theory, because we apply a large temperature jump at the inversion, which is not in equilibrium with the forcing. Fluctuations in the vertically integrated kinetic energy (Fig. 2.1d) are surprisingly small given the different turbulence parameterizations in both models.

Using this DCBL case we show that the LSM has been successfully implemented into UCLA-LES. In the next step, we test the coupling with the radiation scheme and the behavior with diurnal surface forcing.

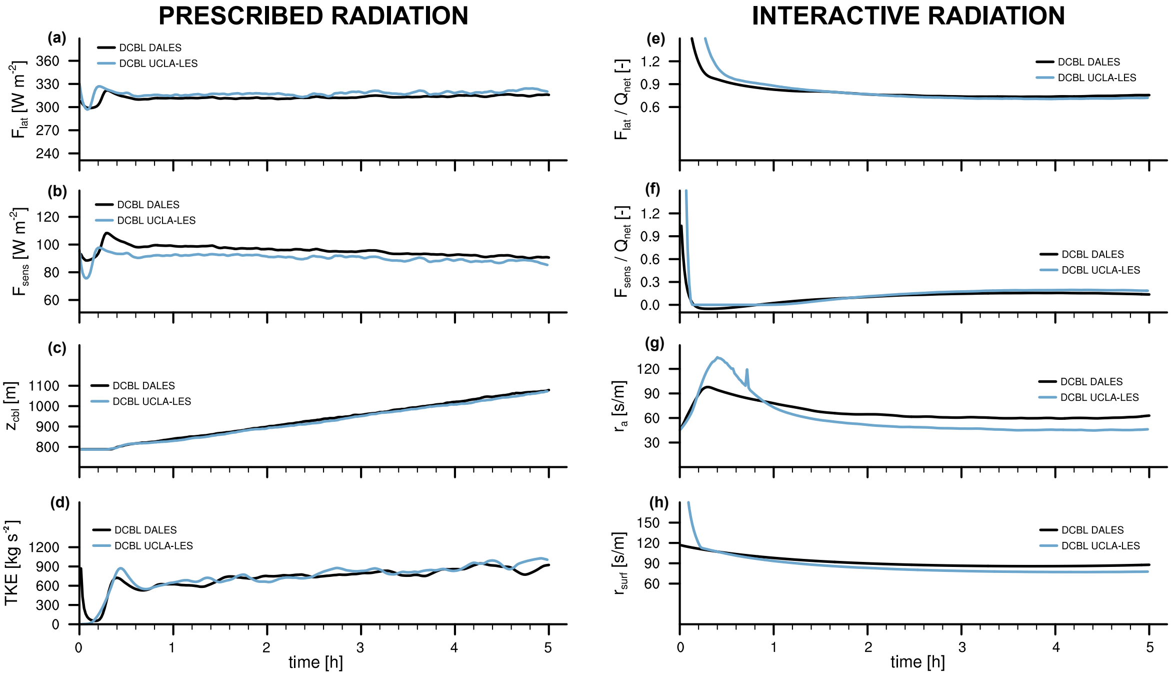

Figure 2.1: Time series of domain mean (a) surface latent heat flux, (b) surface sensible heat flux, (c) boundary layer height and (d) vertical integrated turbulent kinetic energy for the models UCLA-LES and DALES and with fixed surface radiation. The other time series are determined with interactive diurnal radiation and show (e) the latent and (f) sensible heat fluxes scaled with Q_{net} and the (g) aerodynamic and (h) surface resistance for both models.

Experiments with Interactive Radiation

In this case the available net radiation at the land surface is calculated interactively by the radiation scheme from the balance of incoming and outgoing short- and long-wave radiation. Therefore, Q_{net} is not constant as in the previous scenario but shows a distinct diurnal cycle. In UCLA-LES, the radiation is sampled using the spectral Monte Carlo scheme (Pincus and Stevens, 2009), whereas in DALES, a simple parameterization for the incoming and outgoing radiation at the surface is used (Stull, 2000). The radiation scheme is initialized at day 287 of the year and at 48 degrees north. The experiments are once again started at 8 LST and stopped at 13 LST (after the maximum insolation is reached).

Although the simulation with DALES is started at the same local time, Q_{net} is different in both models because different radiation parameterizations are used. In DALES, Q_{net} is on average 81 Wm^{-2} smaller compared to UCLA-LES. The difference stems mostly from the downward longwave radiation and is a result of the different radiation parameterization. Because we do not test the performance of the radiation model, the resulting surface fluxes of both models are normalized with their corresponding values of Q_{net} to facilitate the comparison (Fig. 2.1e,f). After an initial spin-up period, the surface energy is partitioned similarly in both models. The deviations in the evaporative fraction (Fig. 2.1e) are again less than 5 %, whereas the deviations in

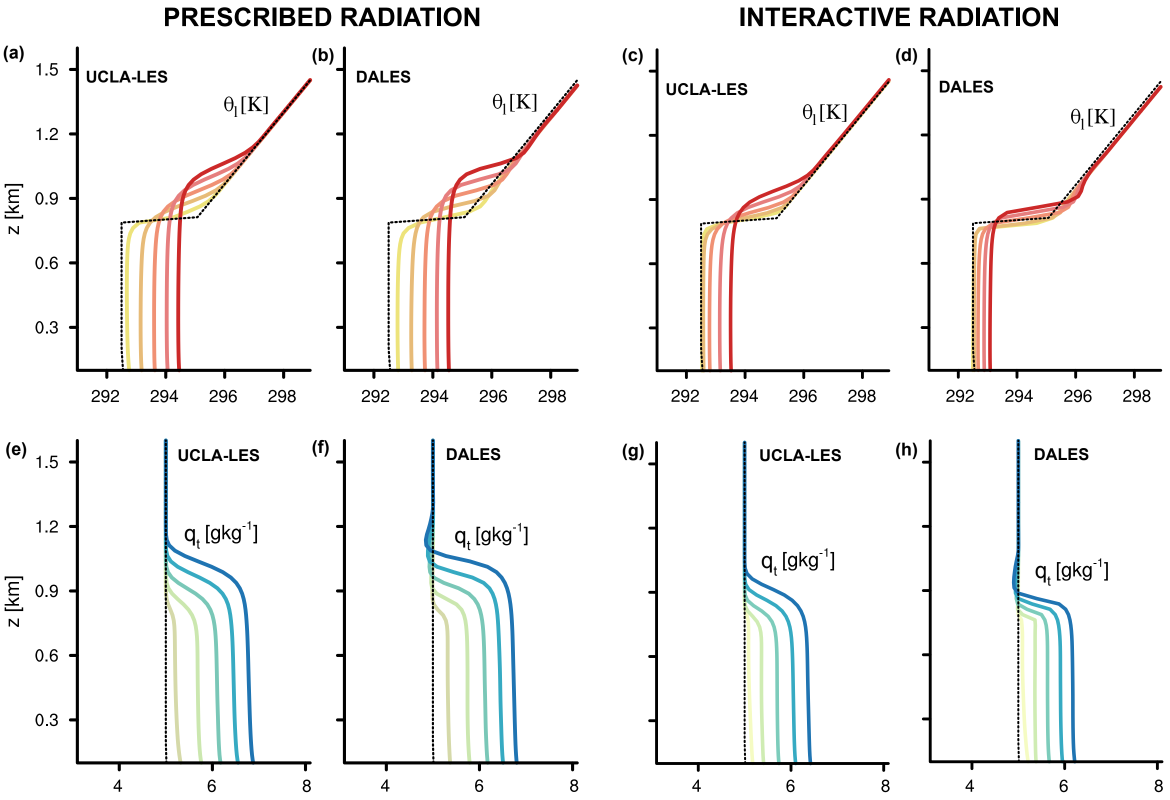

Figure 2.2: Vertical profiles of domain mean (a-d) liquid water potential temperature, (e-h) specific humidity for the models UCLA-LES and DALES. Configuration with prescribed surface energy (a,b,e,f) and with the coupled radiation scheme (c,d,g,h). Dashed lines indicate the initial conditions and continuos lines show values every consecutive hour (9-13 LST) with increasing shade of color.

the sensible heat flux are considerably higher (+ 25 %). The surface fluxes depend on the resistance to aerodynamic and surface properties, shown in Fig. 2.1g,h. When averaged over the last two hours of simulation time, the aerodynamic resistance, r_a, in DALES is about 30 % lower and the surface resistance, r_surf, is 10 % lower compared to UCLA-LES. The small deviations in the surface resistance are caused by differences in the incoming solar radiation and temperature at the surface (see Eq. 2.16). The large deviations in the sensible heat flux are explained by the strong dependence on the aerodynamic resistance. The calculation of the surface drag coefficient differs between both models and is identified as the reason for the different surface flux partitioning. Both the iteration method for the computation of the Monin-Obukhov length, (L), and the integrated stability functions for momentum (ψ_m) and heat (ψ_h) are different among the models. Further analysis reveals that the integrated stability functions induce the surface flux differences between both models, while the iteration methods give very similar results.

The simulations with interactive radiation show a diurnal cycle in the available energy and therefore the boundary layer grows at a much slower rate compared to the experiments with constant available surface energy. At the end of the simulation period, both the mixed layer temperature and specific humidity are lower in the experiments with interactive radiation (Fig. 2.2c,d,g,h) compared to the experiments with prescribed radiation (Fig. 2.2a,b,e,f).

Differences in the vertical structure are also visible among the two models for the experiments with interactive radiation (Fig. 2.2c,d,g,h). In DALES, the boundary layer height, temperature and humidity are lower compared to UCLA-LES, because the total energy input into the boundary layer is smaller. The structure of the dry convective boundary layer is again similar, except that in DALES we find a rather unusual warming in the layer just above the inversion. Because this warming is a local effect, we believe that it is not connected to land-surface processes but to the different turbulent closures employed by the models. The TKE based scheme in DALES allows for transport of kinetic energy while the turbulence model in UCLA-LES acts only locally. An increased upward transport of TKE from the boundary layer into the free atmosphere might explain the warming on top of the boundary layer in DALES. The effect appears smaller in the experiments with interactive radiation because the direct transport is faster than the modeled transport term. Despite this rather small warming effect, the experiments show a reasonable coupling between the atmospheric radiation and the land-surface scheme.

In both experiment setups, the UCLA-LES coupled to the LSM was able to produce reasonable sensible and latent heat fluxes resulting in a very similar boundary layer structure as compared to DALES (Fig. 2.2). To further evaluate the performance of the LSM in a cloudy case, an idealized oceanic case (RICO) has been run with the interactive LSM (not shown). Further validation with a cloudy case and comparison to results from the COSMO model in terms of the development of deep convection over land with a coupled LSM is given in Chapter 3.3. These results also reveal a good agreement between the two models. Hence, we have successfully implemented the LSM into UCLA-LES. The modeling framework can now be applied to study surface heterogeneities and their interaction with moist convection.

Chapter 3

The Influence of Land Surface Heterogeneities on Cloud Size Development[1]

3.1 Introduction

Energy fluxes at the land-atmosphere boundary are spatially heterogeneous as a result of variability in the surface properties. In addition, these exchange processes are also regulated by the atmospheric state. Weather and climate predictions are thus expected to be sensitive to land-atmosphere interactions (e.g Koster et al., 2004). The diurnal cycle of convection is particularly sensitive to land-atmosphere interactions because convective clouds root in the planetary boundary layer. Several studies performed with large-eddy simulations have investigated the mechanisms controlling the transition from shallow to deep convection (Khairoutdinov and Randall, 2006; Kuang and Bretherton, 2006; Wu et al., 2009; Hohenegger and Stevens, 2013). Khairoutdinov and Randall (2006) as well as Kuang and Bretherton (2006) suggested that the horizontal widening of clouds as time proceeds is important for the transition to deep convection. Wu et al. (2009) argued that the transition happens when shallow clouds become on average buoyant, and Hohenegger and Stevens (2013) dismissed the idea that moistening by congestus clouds is important for triggering deep clouds. Despite this improved understanding, the diurnal cycle of deep convection remains a major challenge for current weather and climate models with a typically too late onset of precipitation in cloud-resolving models (e.g. Petch et al., 2002; Baldauf et al., 2011; Kühnlein et al., 2014) and too early onset of precipitation in models with parameterized convection (e.g. Bechtold et al., 2004). Moreover the above-mentioned studies have focused on the transition over homogeneous surfaces. In this study the effect of heterogeneous surfaces on the transition is examined.

---

[1] **Rieck M.**, C. Hohenegger and C. van Heerwaarden (2014): The influence of land surface heterogeneities on cloud size development. Mon. Wea. Rev., **142**, 3830–3846.

It has long been known that heterogeneous surface conditions affect the state of the planetary boundary layer, the development of shallow convection and may influence the amount of convective precipitation. Avissar and Schmidt (1998) and others explained the generation of mesoscale circulations as a result of surface heterogeneity. From linear theory it was shown that the circulation strength increases with patch size (Dalu and Pielke, 1989). Since then several high-resolution modeling studies with grid spacings ranging from tens to hundreds of meters have been carried out to understand these circulations and their possible importance for shallow convection (Raasch and Harbusch, 2001; Van Heerwaarden and Vilà-Guerau de Arellano, 2008; Garcia-Carreras et al., 2011; Huang and Margulis, 2012). The use of high resolution is crucial given the small-scale nature of the simulated phenomena. It has been found that roll like structures create local areas of convergence associated with strong vertical motion. These circulations are confined by the boundaries of the land surface discontinuities with their strength depending on the amplitude of the surface heterogeneity. an HeerwaardenVAN HEERWAARDEN and Vilà-Guerau de Arellano (2008) found areas of higher relative humidity over warm patches indicating a higher potential for cloud formation. Huang and Margulis (2012) showed that strongly heterogeneous surfaces yield thicker and deeper shallow convective clouds. Garcia-Carreras et al. (2011) explained the reasons for a preferred location of shallow convective clouds on the front of the mesoscale circulations. Recently, Kang and Bryan (2011) studied the effect of the amplitude of the surface heterogeneity on the transition to deep convection by prescribing sinusoidal surface fluxes of various amplitudes. As the amplitude becomes larger the area of mesoscale convergence becomes narrower and stronger and will lead to an earlier transition to deep convection. Kang and Bryan (2011) suggested local differences in the planetary boundary layer height to explain their results.

Due to the computational costs, three-dimensional high-resolution simulations of deep convection with an interactive land surface model have not yet been performed. Results from two-dimensional or coarser resolution simulations with partly parameterized convection exist (see Pielke, 2001, for a review). Lynn et al. (1998) especially found that precipitation increases with patch size with a maximum close to the local radius of deformation. Later, using quasi three-dimensional simulations, Lynn et al. (2001) could not reconfirm a linear relationship between total accumulated rainfall and patch size. However, precipitation varied with the size of the individual patch. Limitations in both domain and grid sizes raise the question whether the effects of surface heterogeneity have been correctly modeled in those earlier studies (see Hohenegger et al., 2009).

Given these various effects of land surface heterogeneities on convection, several authors have also attempted to implement such effects in convective parameterizations. Lynn et al. (2001) for instance proposed to alter the triggering formulation. Future scale-aware convective parameterizations are expected to make use of the statistical nature of convection by considering an ensemble of clouds and directly predict the time evolution of the cloud size. The Eddy Diffusivity Mass Flux scheme (Neggers, 2009) or the convection scheme developed by Plant and Craig (2008) may be seen as first attempts in this direction. Recent studies on shallow convection over homogeneous surfaces have shown that the cloud size distribution can be described by a power law with a scale break at the larger clouds (Neggers et al., 2003; Dawe and Austin, 2012; Heus and Seifert, 2013). Prediction of the correct cloud size is also important for conventional bulk mass flux schemes where the entrainment rate is often implicitly assumed to be inversely proportional to the cloud radius (e.g. Kain, 2004).

The goal of this study is to assess and understand the effects of surface heterogeneity on the transition from shallow to deep convection. Of particular interest are possible relationships between (i) the patch size of the surface heterogeneity and the transition time and (ii) the patch size and the cloud size distribution. The cloud size distribution is characterized by the functional shape of its distribution (e.g. power law, exponent of the power law, scale break) and the evolution of its largest cloud. The view that clouds need to grow in (horizontal) size to transition to deep convection, emphasized recently for the development of deep convection over homogeneous surfaces, is adopted. Larger clouds entrain less and can more easily grow deep. The question addressed by this study may thus be reformulated in simple terms whether and how surface heterogeneities support the formation of larger clouds.

High-resolution, three-dimensional large domain large-eddy simulations coupled to a land surface model are employed. The setup allows an interactive representation of the dynamical interactions between the land surface and the atmosphere including the effect of cloud shading, local circulations and cold pools on heating and evapotranspiration. An idealized case mimicking the transition from shallow to deep convection over mid-latitude continental areas during summer is simulated. Surface heterogeneity with various patch sizes are imposed by varying the leaf area index.

Except for the study by Kang and Bryan (2011), previous studies on the effects of surface heterogeneity have neither focused on the transition phase, nor used fully interactive three-dimensional large-eddy simulations. The present study differs from the one by Kang and Bryan (2011) in several key points: The model setup is substantially advanced by the use of an interactive land surface, the focus lies on the sensitivity to the patch size of the surface heterogeneity and not to its amplitude, and the impact on the cloud size distribution is investigated.

The chapter outline is as follows. Section 3.2 describes the model and experimental setups in more detail. The basic effects of heterogeneous surface conditions on the diurnal cycle of convection, on the mean cloud features and especially on the transition time are presented in Section 3.3. The shape and evolution of the cloud size distribution as well as its relationship to the patch size of the surface heterogeneity is discussed in Section 3.4, followed by a detailed analysis of the underlying mechanisms in Section 3.5. Summary and discussion are given in Section 3.6.

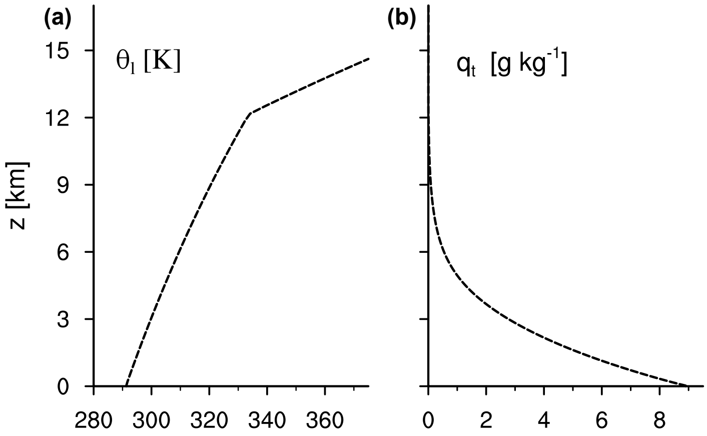

Figure 3.1: Initial profile of (a) liquid water potential temperature (θ_l) and (b) total water specific humidity (q_l).

3.2 The Experiment Setup

The UCLA-LES is employed to simulate the transition from shallow to deep convection over mid-latitude continental area during summer. The computational domain spans 1024 × 1024 × 118 grid points with an isotropic horizontal grid spacing of 100 m. In the vertical a stretched grid ranging from $\Delta z = 50$ m in the lowest boundary layers up to $\Delta z = 500$ m near the tropopause is used.

This study uses initial conditions from Schlemmer et al. (2011) representative for mid-latitude summertime convection. The atmospheric dataset is taken from radio soundings around Munich, Germany and from zonal mean climatologies for summertime conditions at 48° N. Our experiments nevertheless differ in a few key points. First, due to computational limitations in this study we simulate only one diurnal cycle instead of an equilibrium diurnal cycle that is averaged over 30 consecutive days. Second, a uniform and height independent background wind of 0.5 m s^{-1} is prescribed. Third, heterogeneous surface conditions are considered. Finally and most importantly, the horizontal resolution amounts to 100 m instead of 2.2 km, meaning that both shallow and deep convection can be explicitly resolved.

Figure 3.1 shows initial profiles of liquid water potential temperature and total water specific humidity used in this study. The liquid water potential temperature linearly increases up to the tropopause at 12.8 km followed by a much stronger increase. This translates into a tropospheric lapse rate of absolute temperature of 6.8 K km^{-1}. The specific humidity decays with height, resulting in a relative humidity of 68 % in the lower atmosphere and 40 % at 5.5 km height.

The skin layer is characterized by a vegetated surface and initialized with a surface temperature of 291 K. The surface roughness length for momentum is set to 0.04 m and 0.008 m for heat, respectively. The soil is classified as loam with a wilting point of 0.171 m^3 m^{-3} and a field capacity of 0.323 m^3 m^{-3}. The upper three soil levels are initialized with a soil moisture content of 0.27 m^3 m^{-3} (about 85 % saturation of field capacity) and a temperature in equilibrium with the skin and first atmospheric layer. The soil initial state is thought to represent continental midlatitude conditions, and is similar to the CONTROL case presented in Schlemmer et al. (2011).

Six experiments are performed (see Table 3.1). Five of them employ heterogeneous surface conditions with a fixed patch size. The heterogeneity at the surface is prescribed exclusively by varying the leaf area index (LAI) in a checkerboard pattern. For this purpose a fixed LAI of 2.0 and 6.0 is used. The above-mentioned patch size thus refers to the size of one such patch of constant LAI. Changes in LAI induce changes in sensible and latent heat flux between the patches (see Fig. 3.2). All other surface conditions are held constant across the patches. The chosen specification of the surface heterogeneity is thus not meant to represent realistic surface conditions but to understand the effects of surface heterogeneity in a simple and idealized setup. Despite this idealization it is to note that the modeled surface fluxes are in the order of magnitude of measurements over grassland for various FLUXNET sites in central Europe (see Fig. 2 in Teuling et al., 2010). The differences in surface fluxes between the two surfaces types may be caused by varying the vegetative situation or the soil moisture. Similar flux variations were observed over cropland with different LAI during the SMACEX campaign (see Tabel 4 in Su et al., 2005).

The sixth simulation employs homogeneous surface conditions (HOM). The LSM is switched off and the surface fluxes are prescribed by averaging the surface fluxes of HET-XS. Although HOM has no interactive surface, this technique assures comparability with the HET experiments since all simulations experience the same mean energy input as long as the cloud cover remains similar (not shown). This is especially true during the transition phase (see e.g. Fig 3.4a).

3.3 Main Features and Transition Times

In the land-atmosphere system the surface fluxes of heat and moisture closely follow the incoming net radiation with the surface determining their partition. The available incoming net radiation reaches its maximum at 12 local standard time (LST) resulting in domain mean average latent and sensible heat fluxes of 374 Wm^{-2} and 145 Wm^{-2} respectively. These values are akin to the ones obtained in Schlemmer et al. (2011) for a similar but homogeneous case simulated with the COSMO model.

Figure 3.2 shows the horizontal distribution of the surface fluxes at 11 LST. Alternating warm and dry and cold and wet patches can be recognized. The displayed checkerboard pattern mirrors the imposed surface heterogeneity in spite of the influence of turbulence, clouds and the developing near surface anomalies in atmospheric temperature and moisture. In HET-XL, the sensible heat flux is 40 Wm^{-2} higher over the warm than over the cold patch whereas the latent heat flux is 122 Wm^{-2} higher over the cold than

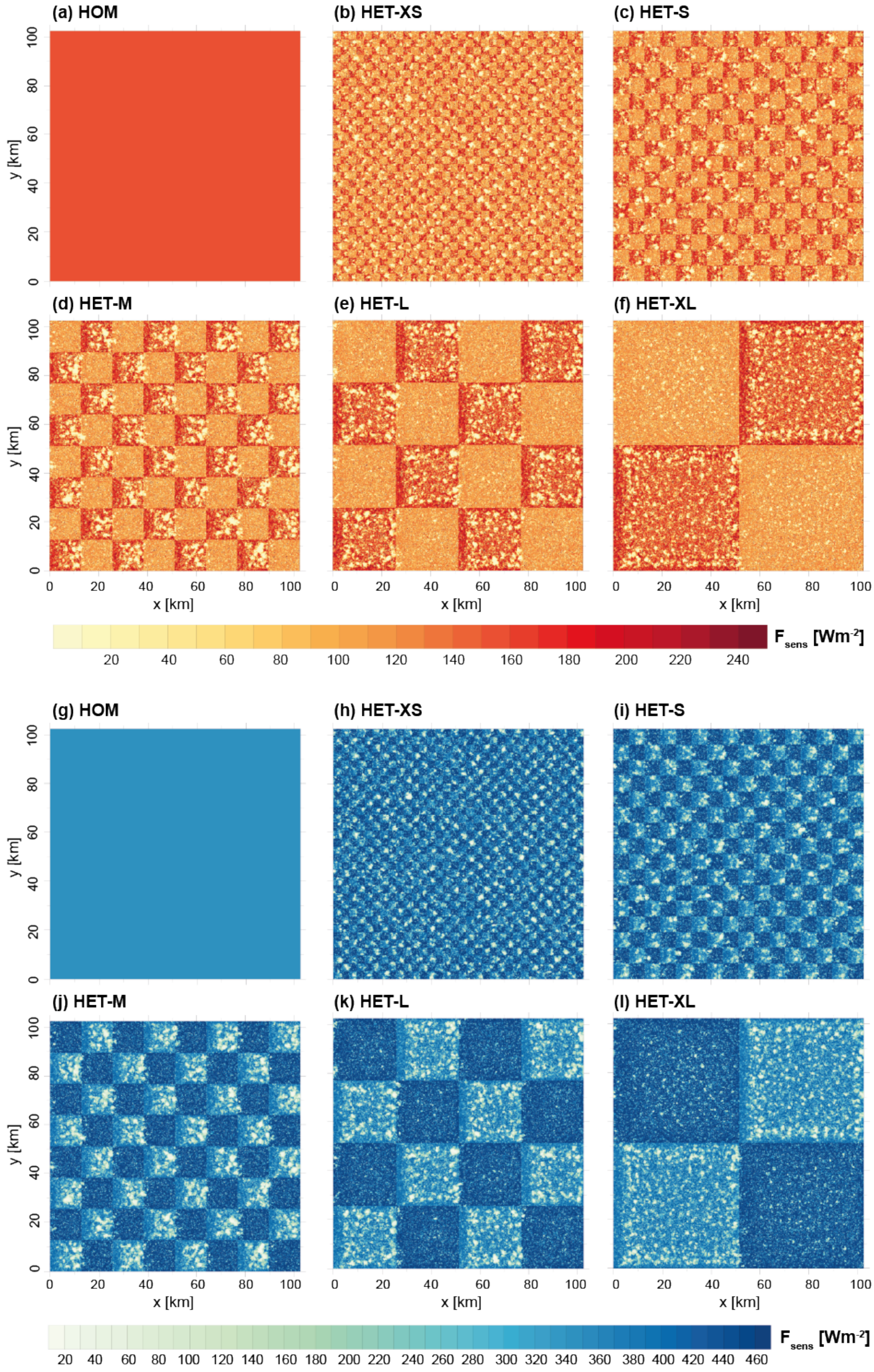

Figure 3.2: Horizontal view of the surface fluxes, (a-f) sensible and (g-l) latent heat, in the different experiments at 11 LST.

over the warm patch. The corresponding mean Bowen ratios are 0.59 for the warmer and 0.32 for the colder patch, indicating a higher potential for turbulence and stronger updrafts over the warmer patch.

Although the use of an interactive LSM does not mask the imposed pattern in surface heterogeneity, one effect is clearly visible in Fig. 3.2. The lighter spots visible on the warm patches, both on the sensible and latent heat flux, mark the location of clouds (compare e.g. Fig. 3.2 and Fig. 3.3). The effect of cloud shading can be quantified by comparing the fluxes for cloudy and non-cloudy points. In HET-XL at 11 LST the presence of clouds over the warm patch reduces the sensible heat flux by 12 Wm^{-2} whereas the reduction is only 2 Wm^{-2} over the cold patch. Since most of the clouds are located above the warm patch, the shading effect decreases the difference in surface sensible heat fluxes between the two surface types by 20% ($\Delta F_{\mathrm{sens,clearsky}} = 50\ Wm^{-2}$ and $\Delta F_{\mathrm{sens,allsky}} = 40\ Wm^{-2}$). This suggests that models without interactive land surface may overestimate both local surface fluxes and the horizontal gradient due to surface heterogeneities and consequently produce too strong mesoscale circulations. These effects are expected to be larger for situations with higher cloud cover and cloud albedo. The attenuation of the available net incoming radiation by clouds is independent of the patch size as long as the cloud cover remains constant across the simulations (see Fig. 3.4a), which is the case up to about 12 LST.

Figure 3.3 shows the horizontal distribution of the liquid water path at 11 LST for the various experiments. The signature of the surface heterogeneity is again clearly visible. Cloud formation happens predominantly over the warm and dry patches. This effect has been discussed for different cases of summertime convection over heterogeneous land surfaces (Avissar and Schmidt, 1998; Kang and Bryan, 2011; Garcia-Carreras et al., 2011). Clouds form when strong thermals penetrate the boundary layer and reach their lifting condensation level. Conditions for cloud formation can be more favorable over warm patches in the sense that thermals are stronger, the boundary layer is deeper and convective inhibition is reduced. Additionally, mesoscale circulations intensify cloud formation along the warm side of patch boundaries. The effect of mesoscale circulations on the timing and size distribution of the convective clouds is discussed in Section 3.5.

The time evolution of cloud cover and rain rate is shown in Fig. 3.4. All the simulations exhibit a similar and realistic diurnal cycle of convection. At 8 LST thermals start penetrating the convective boundary layer. Shallow clouds appear shortly thereafter and grow deeper causing a rapid increase in cloud cover of up to 20 % around noon (Fig. 3.4a). Convective clouds are triggered in response to the increasing instability (surface warming) and disappear in the evening when the surface forcing ceases. Convective precipitation starts around noon and peaks later in the afternoon (Fig. 3.4b).

A similar behavior was found in Schlemmer et al. (2011). Both the onset of clouds and of precipitation nevertheless occurs more rapidly in HOM as compared to the CONTROL simulation of Schlemmer et al. (2011). The precipitation amounts are also smaller in HOM whereas the time of peak precipitation remains identical. A major

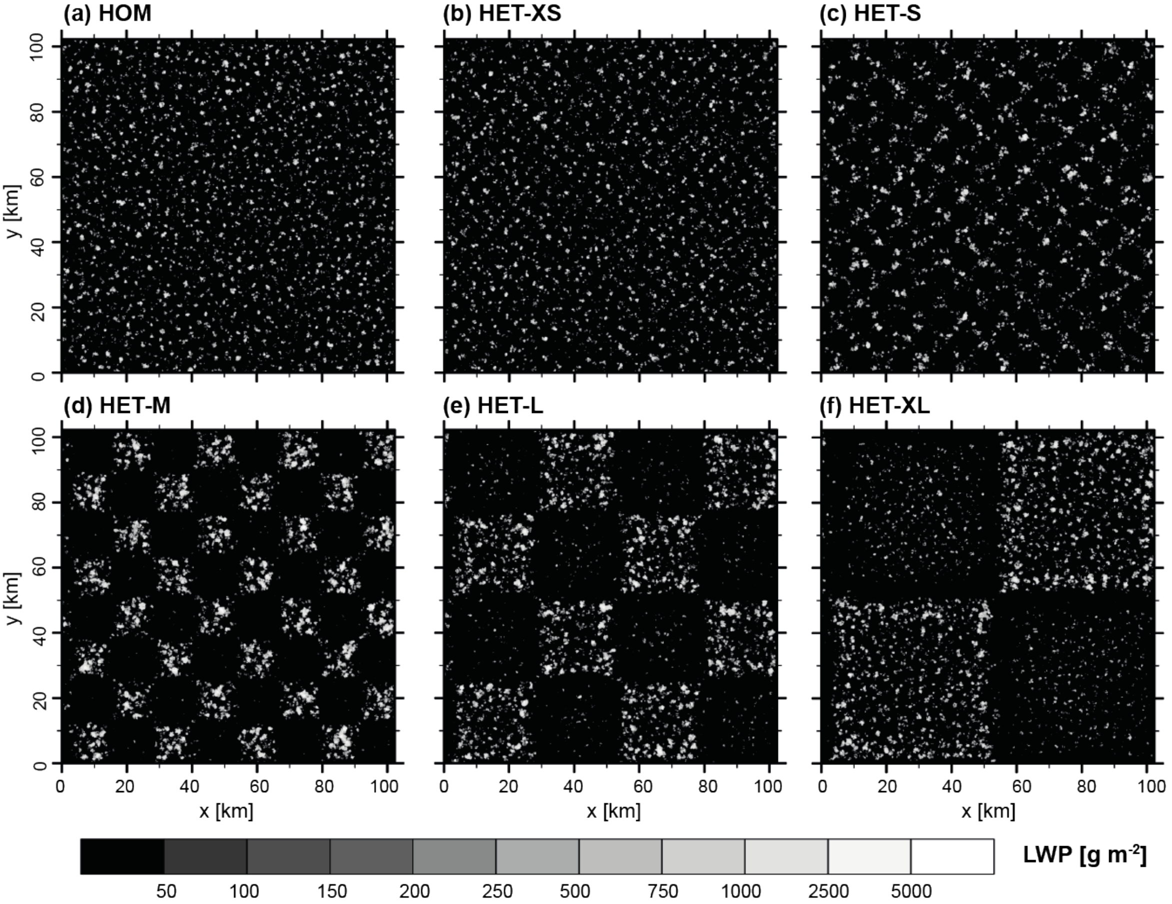

Figure 3.3: Instantaneous view of the cloud field in terms of liquid water path in the different experiments at 11 LST.

difference between the two studies is the model resolution. Shallow convection is explicitly resolved in UCLA-LES whereas the COSMO grid size is too coarse to explicitly resolve all shallow clouds. This may in part explain the later start of precipitation in COSMO, a common issue in cloud-resolving models (Petch et al., 2002; Baldauf et al., 2011; Kühnlein et al., 2014). Furthermore, both models employ a different microphysics scheme. Other differences, e.g. the surface fluxes calculated from different LSMs or the domain size, may further explain the discrepancies between the two experiments. Given these differences in the modeling setup the obtained results remain remarkably similar and give confidence that they are representative for mid-latitude summertime convection.

Comparison of the different simulations in Fig. 3.4a indicates that the cloud cover remains similar as long as no precipitation is falling. Precipitation is an efficient mechanism to remove moisture from the atmosphere so that changes in precipitation rates tend to result in changes in cloud cover. The cloud cover is mainly determined by the smaller clouds due to their abundance (see Wood and Field, 2011). As will be shown in section 3.4, the distribution of these small clouds remains similar between the experiments before strong precipitation sets in. The time of cloud onset is barely

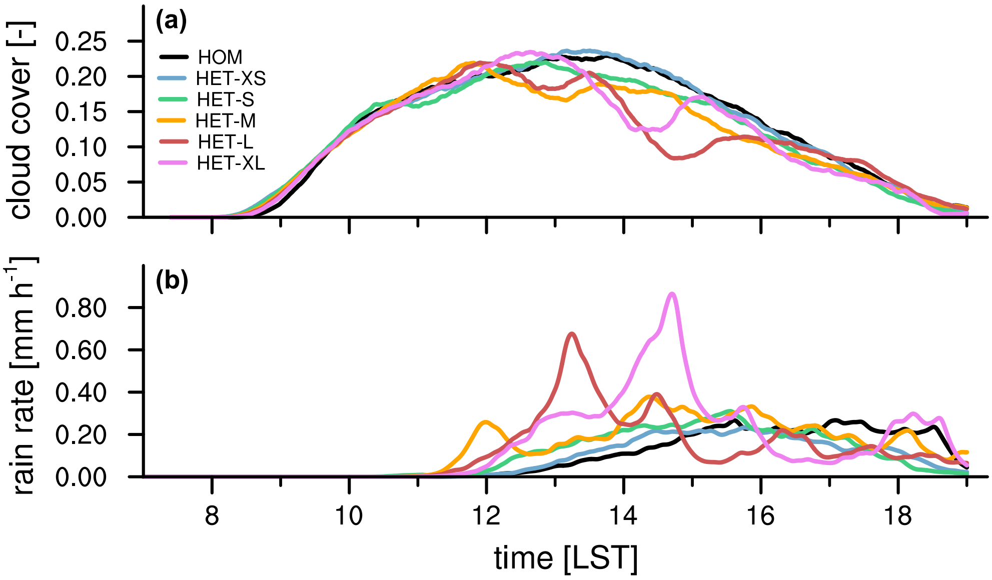

Figure 3.4: Time series of domain averaged (a) cloud cover and (b) surface rain rate.

influenced by the patch size. The use of a relatively moist initial profile may limit the impact of surface heterogeneity in this regard.

In contrast to Fig. 3.4a the timing and strength of the surface precipitation varies clearly with patch size (Fig. 3.4b). Here, HET-M begins to precipitate before HET-L followed by HET-XL, HET-S, HET-XS and HOM whereby HET-XS and HOM exhibit a very similar time series. Although the patch size clearly influences the timing of precipitation, there is no linear relationship between the time of precipitation onset and the patch size (see further below). The differences in timing between the simulations are more visible in the precipitation time series than in the cloud cover because precipitation formation is a slower process. The domain mean precipitation averaged over the full simulation period generally increases with increasing patch size (see Table 3.1). The domain mean precipitation is largest in HET-XL with a 67 % increase compared to HOM. The obtained changes in precipitation with patch size confirm the results from two-dimensional cloud resolving simulations as presented by Lynn et al. (1998). In their case the precipitation also tended to increase with patch size. A simulation with a patch size of 64 km yielded an increase by about 60 % compared to a simulation with homogeneous surface conditions (from a visual inspection of their Fig. 10). Chen and Avissar (1994) furthermore reported an increase in precipitation with patch size. Both studies attributed this behavior to the dependency of the triggered mesoscale circulation on the imposed perturbation scale as reported by Dalu and Pielke (1989). Linearization of the equation of motion indicates that the strongest circulations are obtained when the scale of the imposed perturbation equals the size of the local Rossby radius of deformation, which is about 100 km in mid-latitudes. By studying the response of the convection to a localized source of heating, Robinson et al. (2008) proposed an alternate explanation and argued that the strongest response of

experiment	patch size [km]	$t_{transition}$ [h]	$t_{collision}$ [h]	precipitation [mm day^{-1}]
HOM	-	12:15	-	1.12
HET-XS	3.2	12:05	-	0.94
HET-S	6.4	11:35	10:30	1.17
HET-M	12.8	11:00	11:30	1.60
HET-L	25.6	11:04	13:00	1.45
HET-XL	51.2	11:20	13:30	1.87

Table 3.1: Summary of the performed experiments with experiment name, patch size, local time of transition to deep convection, local time of breeze front collision and domain mean precipitation averaged over the simulation period. The transition time is determined from profile statistics sampled every 60 seconds. The collision time is diagnosed from vertical cross sections showing horizontal (as displayed in Fig. 3.8) and vertical wind, sampled from 3D data every 30 minutes.

convection should be obtained when the aspect ratio of the applied heating matches the ratio of vertical and horizontal wave numbers demanded by the dispersion relation for buoyancy waves. This scale was found to be 50 km, which is equivalent to the patch size of HET-XL. Hence both explanations support the results of Table 3.1, i.e. the largest domain mean precipitation for HET-XL given the considered patch sizes.

To assess the transition from shallow to deep convection more quantitatively, mean profiles of cloud condensate and precipitation are sampled and displayed in Fig. 3.5. All experiments show a gradual increase of cloud depth with time until they finally transition to deep convection. The transition time is defined as the time when the mean cloud condensate exceeds 1 mg kg^{-1} at 5.5 km height for at least 10 minutes. Other choices give different transition times but do not fundamentally alter the main differences between the simulations. From now on, the word shallow (deep) is reserved to characterize the convection before (after) the diagnosed transition time.

The transition time substantially differs among the experiments (see Fig. 3.5 and Table 3.1). The transition tends to occur faster with increasing patch size, although HET-M exhibits the fastest transition. The behavior is similar to the behavior of the onset time of precipitation, confirming Figure 3.4a. The transition is already completed at 11:00 LST in HET-M whereas it takes 1.25 h longer in HOM. Given that the transition is a fast process, taking only 2.5 h in HET-M, a difference of 1.25 h, half the transition time, is not negligible. These differences in transition time can be understood by considering the cloud size distribution and its relationship to the patch size as explained in the next sections.

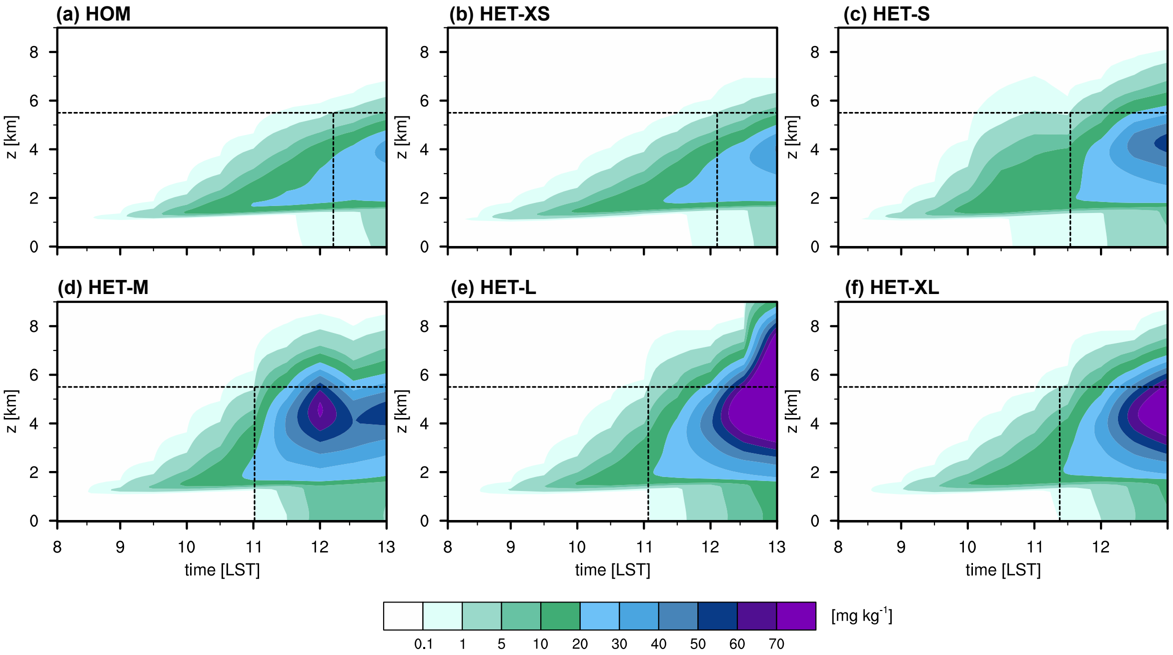

Figure 3.5: Domain averaged vertical profiles of cloud condensate for all experiments (a)-(f) (condensate includes liquid water, ice, snow, hail, graupel and rain). Vertical dashed lines denote transition time, where the cloud condensate exceeds 1 mg kg^{-1} at 5.5 km height.

3.4 The Cloud Size Distribution

To determine the cloud size distribution and link it to the patch size, we derive the size of the clouds from the simulation statistics. We follow here the approach taken in previous studies (e.g. Neggers et al., 2003). Cloud clusters are first defined based on the value of the liquid water path. A cloud cluster represents a connected area of points where the liquid water path exceeds 50 g m $^{-2}$. This minimum threshold is used to exclude very thin clouds. This prevents deep convective outflow as well as cloud haze from being counted as convective cloud. Because the liquid water path is a vertically integrated quantity such a cloud cluster describes the vertically projected area of a cloud. The wording ”cloud size” then refers to the horizontal extent of a cloud cluster. It is determined as the diameter of a circle that has the same area as the cloud cluster. This method assumes all clouds being circular irrespective of the actual shape, the cloud overlap as well as the splitting and merging in time. From visual inspection of the horizontally projected cloud field we are convinced the approximation that clouds have a circular shape is a good one. The so computed cloud size can be quite large as one cloud may contain several convective cores as long as they are connected in space. The liquid water path is sampled every 60 seconds yielding comprehensive time series statistics. In most of the shallow and deep convective phase the domain cloud number exceeds 1000 objects at a given time. To increase sample size the distributions are calculated from data considering the cloud population within intervals of 30 minutes.

Figure 3.6 shows the cloud size distributions for all experiments from 9 to 12 LST, i.e. during the transition phase. The distributions are displayed in a logarithmic scale. Previous studies based on shallow convection over homogeneous surfaces have indicated that the cloud size distribution can be approximated by a power law with a specific scale break at the largest clouds (Neggers et al., 2003; Dawe and Austin, 2012; Heus and Seifert, 2013). The cloud size density, $N(D)$, ranging from the smallest clouds to the scale break follows the form

$$N(D) \propto D^{\mathrm{b}}. \tag{3.1}$$

The scale break denotes the scale at which $N(D)$ departs from the power law as given in equation 3.1. Unlike in earlier studies, in this study the cloud size statistics do not converge with time since convection is transitioning from shallow to deep. As a consequence the characteristics of the size distribution, the power law exponent and the scale break may differ both in time and between the experiments. Neggers et al. (2003); Dawe and Austin (2012); Heus and Seifert (2013) obtained power law exponents for shallow cumulus convection that are spread around b = -1.7, -1.9 and -2.5 respectively.

In the early shallow phase around 9 LST (Fig. 3.6a), the distribution is generally narrow with almost all clouds being smaller than 1 km. Here, the HET experiments exhibit wider distributions with a maximum cloud size larger by 0.3 km as compared to HOM. Experiments with smaller patch sizes (HET-XS, HET-S) promote slightly larger clouds. The differences are nevertheless rather small so that, to a first approximation, all HET simulations exhibit a similar size distribution. At 10 LST the distributions have advanced towards larger cloud sizes, showing a power law scaling between 0.3 and 1 km cloud size. All curves have a similar shape in this range with a power law exponent around b = -1.9. At this time of simulation HET-S shows the largest clouds with a scale break around 3 km against 1.5 km for HOM. The snapshots at 11 and 12 LST show similar behavior, i.e. a cloud ensemble that continues to grow, a similar power law behavior at the smaller scales and distinct scale breaks. At 12 LST the experiments with the larger patch sizes (HET-M, HET-L, HET-XL) have completed the transition from shallow to deep convection. A distinct scale break is barely visible and cloud sizes in the range from 0.2 to 10 km follow a power law with an exponent around b = -2.2 (Fig. 3.6d). The results (Fig. 3.6) thus demonstrate that there is no clear dependency of the power law exponent of the cloud size distribution on the patch size. The effect of the patch size on the cloud size distribution is only visible in the scale break. Since the experiments with larger patch sizes (HET-M, HET-L, HET-XL) tend to transition earlier, the distribution is more rapidly shifted to larger cloud sizes and the scale break at a given time differs.

Figure 3.6 reveals another important difference between the cloud size evolution over homogeneous and heterogeneous surface conditions. Studies on the transition to deep convection performed with large-eddy simulations over homogeneous surface conditions have indicated that larger clouds grow deeper due to reduced lateral mixing with their

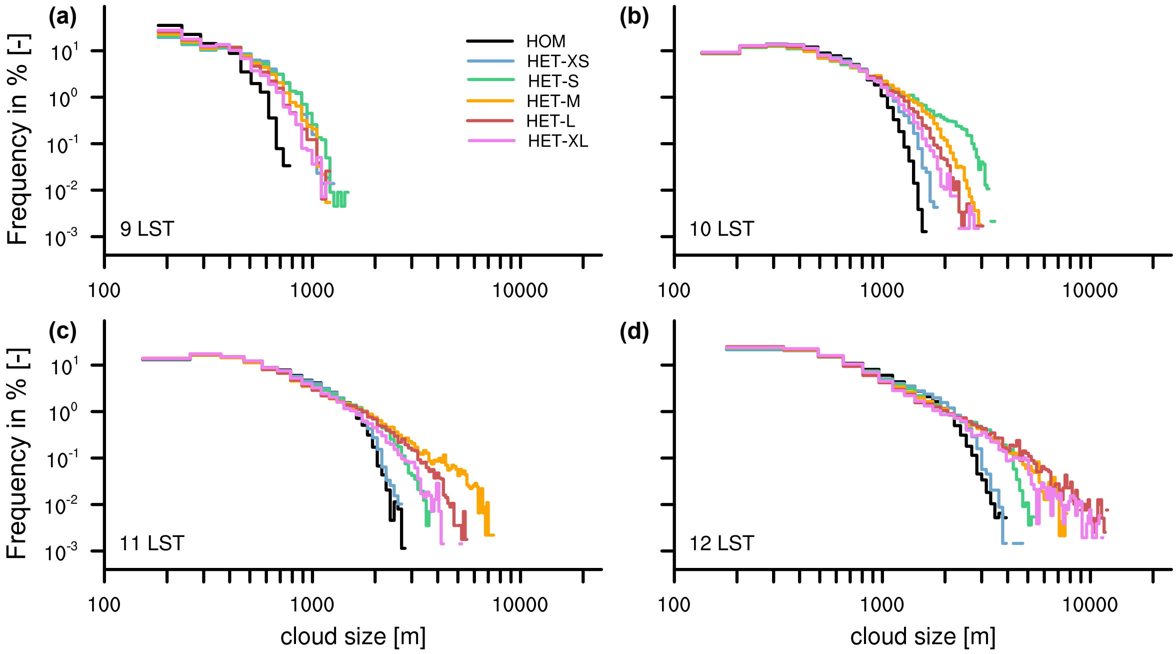

Figure 3.6: Cloud size distribution for the various experiments at different times (a-d). The distributions are calculated from instantaneous values of the liquid water path sampled every 60 seconds and the distributions are averaged over 30 minutes. The same bin width is used among the various experiments. The bin width increases with time to account for the growing cloud population.

environment and that this effect is important in promoting the transition to deep convection. This implies that a simulation with initially larger clouds should transition faster to deep convection. This is clearly not the case in Figure 3.6. Although HET-S displays the largest clouds at 10 LST, it is overtaken by HET-M at 11 LST, which is itself overtaken by HET-L and HET-XL at 12 LST. In a heterogeneous environment, a simulation with the largest clouds at a given time may not transition faster to deep convection than another one. The growth of the larger clouds must be limited by some other process (see next section).

To further understand this behavior the largest clouds are sampled. The resulting time series is shown in Fig. 3.7a. Starting with a size below 1 km the largest clouds grows up to a size between 6 and 22 km. The growth rate however depends both on the patch size and time. In HOM the growth rate of the largest cloud is rather constant in time. The size ranges from 0.5 km at 8:30 LST to 5.2 km at 12:30 LST. This suggests a smooth and unperturbed lifecycle from shallow to deep convection in response to the diurnal cycle of surface heating. Looking at HET-XS, a similar behavior is observed. In HET-S clouds grow more rapidly up to a size of 3.5 km at 10 LST followed by a slow decline in size until 11 LST. A similar effect is visible in HET-M. The cloud size increases up to 7.5 km at 11:30 LST before slightly decreasing until 12:30 LST. At this time HET-L has caught up and exhibits the largest maximum cloud size of 12 km. Finally, at 14 LST, HET-XL displays the largest cloud with a size of 22 km.

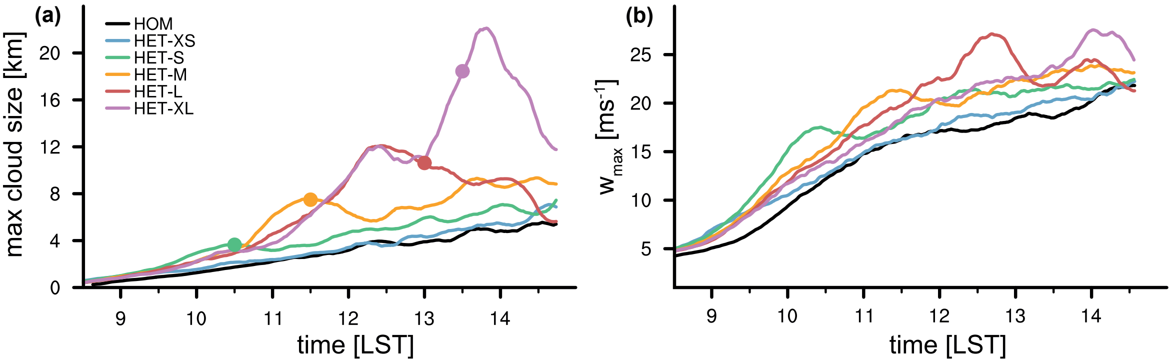

Figure 3.7: (a) Time series of the maximum cloud size for all experiments and (b) domain maximum vertical velocity. Cloud statistics and vertical velocity are sampled every 60 seconds, applying a 20 minutes running mean. Marker points denote the collision time.

Overall, the experiments with larger patch sizes end up producing much larger clouds. Although the local maximum in the size of the largest clouds increases with patch size, its ratio to the patch size stays constant. This ratio amounts to half the patch size. This ratio may vary depending on the atmospheric conditions. Nevertheless it is to be expected to scale with the patch size since the maximum size a cloud may reach is limited by the size of a single patch.

Although the cloud evolution may appear different at first sight, Fig. 3.7a emphasizes a consistent behavior across all simulations consisting of two phases: a phase of above normal growth rate into a local maximum and a return back towards the original growth rate. This behavior suggests a preferred time and length scale for cloud development over heterogeneous land surfaces. Reasons are given in the next section.

3.5 Mechanisms Generating the Cloud Size Distribution

To demonstrate the proposed effect of surface heterogeneities in generating the cloud size distribution, the transition period between 9 and 12 LST is analyzed in detail.

Figure 3.8 shows vertical cross sections through the cloud field in the x-direction at 11 LST. All quantities at a given x-location are averaged in y-direction over patches with the same leaf area index. Clouds are depicted in terms of their cloud condensate including liquid and ice phases. Note that as the cloud condensate is averaged in the y-direction, the apparent size of the clouds in Figure 3.8 does not correspond to the true size of the clouds, as defined in Section 3.4 and displayed in Fig. 3.3 and 3.6. Figure 3.8 indicates that in HOM the clouds are randomly distributed over the whole domain whereas clouds are located directly above the warm patches in the HET experiments. This is consistent with Fig. 3.3. As discussed in Fig. 3.7a, HET-M features the largest clouds at 11 LST.

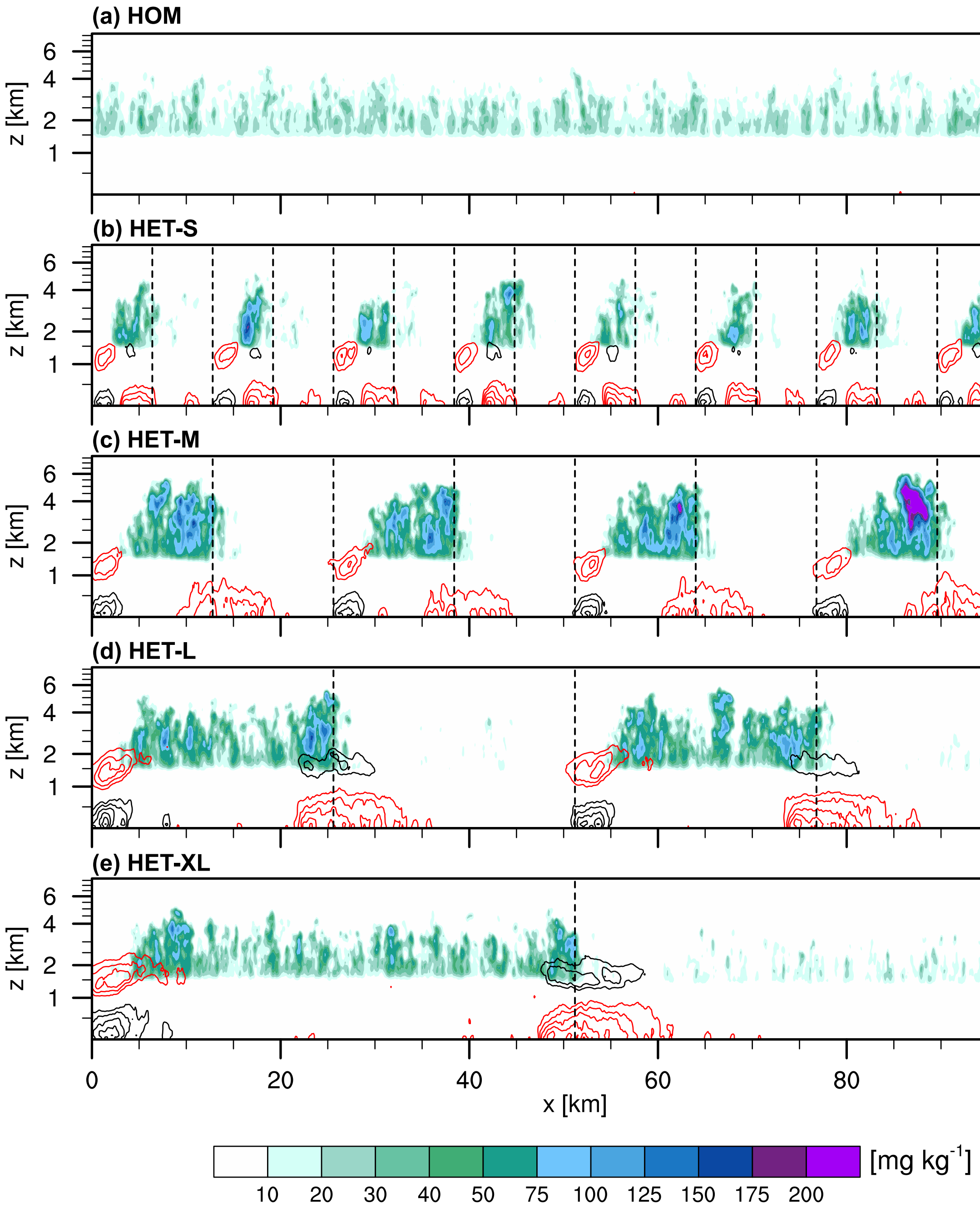

Figure 3.8: Vertical cross section of cloud condensate (shaded contours in mg kg^{-1}) and horizontal wind (contour lines in m s^{-1} with background wind removed, black colors in positive and red colors in negative x-direction, intervals of 0.25 m s^{-1} starting at 0.5 m s^{-1}) for different experiments (a)-(e) at 11 LST. HET-S resembles HOM and is not shown. All quantities at a given location x are averaged in y-direction over patches with the same leaf area index. Dashed lines indicate patch boundaries in y-direction.

The contour lines in Fig. 3.8 show the mesoscale circulations in u-direction that develop due to the surface heterogeneity (see e.g. Avissar and Schmidt (1998); Roy (2003)). Locations with a sharp gradient in wind velocity indicate the position of the breeze front. Cloud development is enhanced at the leading edge of the breeze front where air is lifted and vertical velocities are larger (e.g. Garcia-Carreras et al., 2011). With time, the breeze fronts travel towards the patch center. The periodic heterogeneity in the experiments forces convergence of opposing breeze fronts, which end up colliding. The collision time is defined as the time when opposing horizontal winds from mesoscale circulations converge at the first time (see contour lines in Fig. 3.8) and a single updraft is produced (from cross sections of vertical velocities, not shown). Values of the collision time for the different experiments are listed in Table 3.1. Simulations with larger patch sizes display a later collision time. Note that the collision time is diagnosed from three-dimensional output which is only available every 30 minutes. The collision time is indicated with marker points in Fig. 3.7a. It is evident that in all simulations the cloud size reaches a local maximum near the collision time. Mesoscale circulations produce horizontally confined areas of updrafts surrounded by larger areas of sinking motion. The convergence of the breeze fronts with time produces higher vertical velocities and accelerates the cloud development until the breeze fronts collide. The accelerated cloud development corresponds to the above normal growth rate of the cloud size in Fig. 3.7a as documented in Section 3.4. After the collision of the breeze fronts those more favorable areas for cloud development become less important, the vertical motion weakens and the cloud size development proceeds at a slower rate. This is because the deep convective clouds, which at this time are exclusively located over the warm patches, produce cold downdrafts, cool the surface and stabilize the atmosphere over the warm patches. As mesoscale circulations decay, the remaining clouds continue to grow at a slower rate. Figure 3.7b shows the maximum vertical velocity and confirms a high level of agreement with the time evolution of the size of the largest could. Nevertheless, it is to note that in all heterogeneous experiments both maximum cloud size and maximum vertical velocity remain larger compared to the experiment with homogeneous surface conditions.

It follows that the introduced patch sizes are both favorable and detrimental to the formation of larger clouds. At first, through the effects of the triggered mesoscale circulations, heterogeneous surface conditions allow the formation of larger clouds that expand faster and should more rapidly transition to deep convection. But the finite size of those patches and thus of the updraft areas also sets a limit for the maximum size that a cloud can reach. The latter size may still be smaller than the size a cloud would need to reach 5.5 km, meaning that a simulation with the largest clouds at a given time (e.g. HET-S) may not exhibit the fastest transition to deep convection. HET-M exhibits the fastest transition in Fig. 3.7a because the collision time (11:30) happens at the most optimal time with respect to the time clouds would transition without the help of mesoscale circulation, which is 12.15 LST in HOM. The collision time in HET-XS and HET-S is too early, whereas it is too late in HET-L and HET-XL.

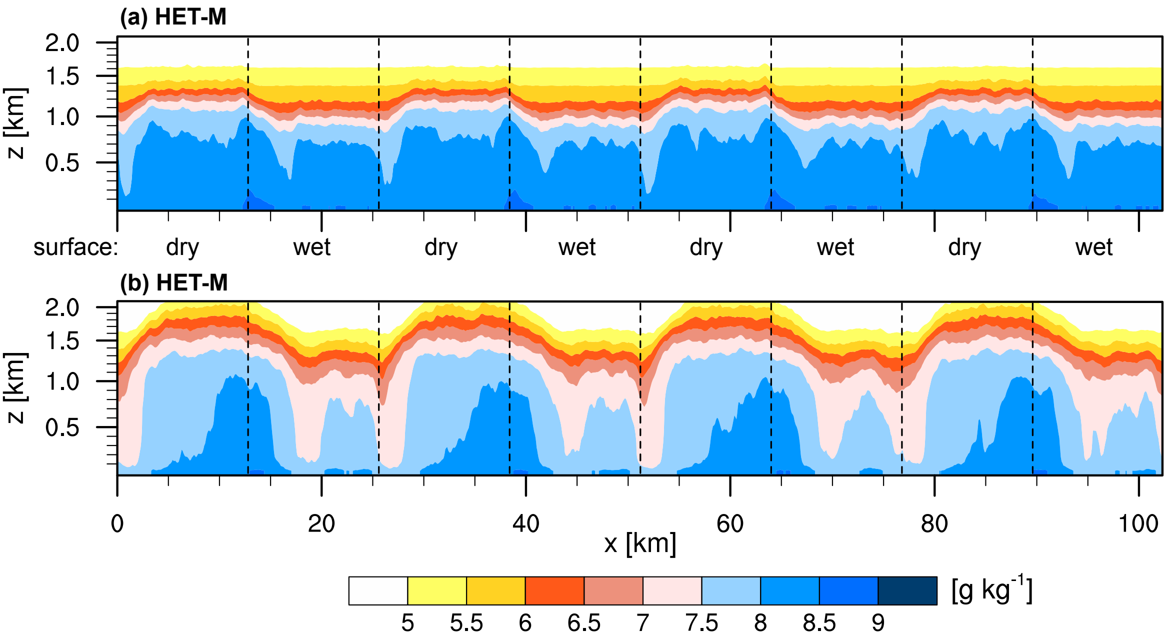

Figure 3.9: Vertical cross sections of the total water content (shaded contours in g kg^{-1}) for HET-M at (a) 9 and (b) 11 LST. All quantities at a given location x are averaged in y-direction over patches with the same leaf area index. Dashed lines indicate patch boundaries in y-direction.

This explains that there is no simple relationship between the transition time and the patch size. Other cases, for instance a drier case where the transition without the help of mesoscale circulation would happen later in time, could favor HET-L or HET-XL. As the precipitation onset follows the transition time (see Section 3.3) the explanation also holds for the onset time of precipitation.

The previous explanation has emphasized the role of the convergence associated with the mesoscale circulations. Additionally, mesoscale circulations also act to bring moist air towards the warm surface patches increasing the amount of water available for cloud formation (Avissar and Schmidt, 1998; Van Heerwaarden and Vilà-Guerau de Arellano, 2008). Figure 3.9 shows two vertical cross sections of total water mixing ratio for HET-M as an example, taken at 9 and 11 LST. At 9 LST, when shallow convection starts, the boundary layer is deeper and the surface layer is drier above the warm patches than above the cold patches. Much of the available net radiation at the surface is released in form of sensible heat, warming the boundary layer. Later, at 11 LST, the circulation advects moist air over the warm patches whereas the air above the cold patches is slowly desiccated through the subsiding branch of the mesoscale circulation. The combined effect of both higher temperature and moisture results in a local maximum in the moist static energy (MSE) above the warm patches, especially close to the breeze front (not shown). These pockets of air with high MSE above the warm patches are a preferential location for the triggering of deep convection.

In some convective parameterizations the boundary layer height is used to determine

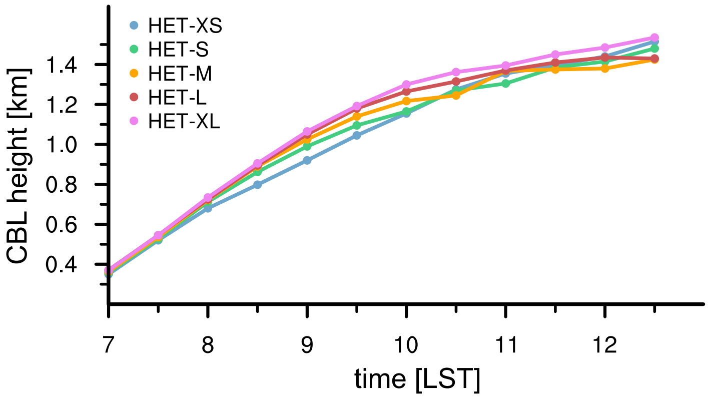

Figure 3.10: Time series of mean boundary layer height sampled only above warm patches. Values are diagnosed from three-dimensional data every 30 minutes.

the maximum initial cloud size in a given area (Graf and Yang, 2007). The idea behind this concept is the fact that clouds grow from thermals with a maximum size limited by the height of the boundary layer itself. The boundary layer growth rate is known to be influenced by the surface buoyancy flux, which is largely controlled by the exchange of sensible heat. Consequently, in heterogeneous environments, the boundary layer may deepen locally (over the warmer patches) and trigger clouds if the condensation level is reached. This effect was found to be important to explain the sensitivity of the transition time to the amplitude of the imposed surface heterogeneity in Kang and Bryan (2011). In addition, the patch size itself may influence the boundary layer height and thus change the expected maximum cloud size.

Figure 3.10 shows a time series of the boundary layer height derived from mean temperature profiles conditionally sampled the over warm patches. We extend the maximum gradient method (see original definition in Sullivan et al., 1998) to account for moist convection. The boundary layer height is defined at the intersection of the tangents to the maximum temperature gradient and to the minimum temperature of the mixed layer. The resulting boundary layer height is similar but slightly lower compared to the standard maximum gradient method. In the morning hours at 7 LST all the experiments depict a very similar boundary layer height with a value near 350 m. Later, at 9 LST, the height reaches about 920 m in HET-XS whereas HET-XL features a height that is 145 m deeper. The boundary layer height appears proportional to the patch size. This is because at larger patch sizes the boundary layer in the center of a patch is less contaminated by its surrounding patches, and thus convect less and exhibit weaker thermals. Kang and Bryan (2011) argued that over areas with deeper boundary layer convective initiation occurs earlier and clouds become deeper. In their study they used an intermediate heterogeneity size of 16 km, which is in between HET-M and HET-L. However, in the present study convective initiation happens first over areas with small patch sizes where the boundary layer is comparably shallow. This discrepancy might be explained by the fact that in all the HET simulations, the buoyancy flux is the same over the warm patch, which was not the case in Kang and Bryan (2011). The assump-

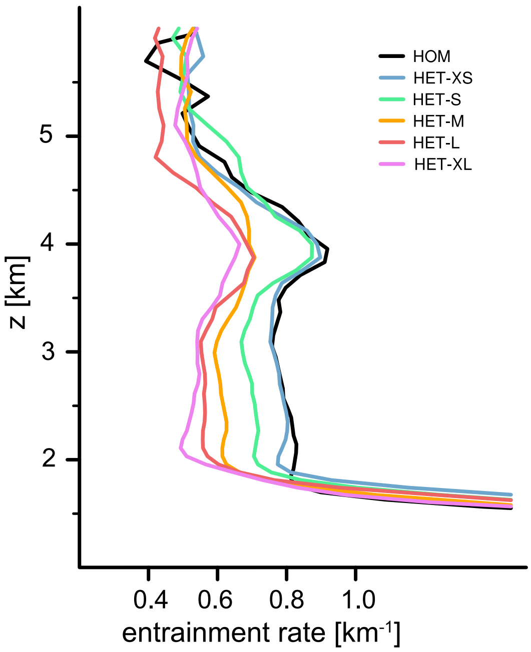

Figure 3.11: Vertical profile of bulk fractional entrainment rate for different experiments at 14:00 LST. The entrainment is diagnosed from LES data following Betts (1975) (see also de Rooy et al., 2013, Eq. 18).

tion that the size of the largest cloud (Fig. 3.7a) scales with the boundary layer height (Fig. 3.10) cannot be found. In fact, at 10 LST the simulation with the shallowest boundary layer (HET-S) exhibits the largest clouds. At later times, the formation of widespread clouds reduces the difference in the boundary layer height between the simulations. Comparison of Fig. 3.7a and Fig. 3.10 again indicates that the boundary layer height is not a good predictor for the cloud size over heterogeneous surfaces as long as the patches sustain a similar surface buoyancy flux. Instead, the timing and strength of mesoscale convergence is a better proxy for the convective cloud development.

The so derived effects of mesoscale circulations on the cloud size distribution may be included in a convective parameterization by modifying the entrainment. The entrainment is often viewed as inverse proportional to the cloud size. As an example, Fig. 3.11 shows the vertical profile of the bulk fractional entrainment rate at 14 LST for the set of simulations. The entrainment of environmental air into the cloud core is diagnosed following Betts (1975) (see also de Rooy et al., 2013, Eq. 18). In the cloud layer between 1.5 and 4 km the entrainment rate decreases with patch size. This is akin to the behavior of the diagnosed maximum cloud size at 14 LST in Fig. 3.7a. In HET-XL the diagnosed entrainment is about 30% smaller compared to HOM. The observed variations in terms of entrainment rate are quite large (see Böing et al., 2012). Such large differences in the entrainment would speak for their inclusion in a convective parameterization.

3.6 Summary and Discussion

The timing of the transition from shallow to deep convection with the sub-sequential precipitation formation is still a major challenge for current weather and climate models. This study investigated the influence of surface heterogeneities on the convective development using large-eddy simulations. We focused in particular on the dependency of the evolving cloud size distribution on the horizontal scale of surface heterogeneity. One idealized case of the transition from shallow to deep convection, as typically occurring during summertime over mid-latitude continental areas, has been simulated with large-eddy simulations. The large-eddy simulations have been coupled to a land-surface model to introduce surface heterogeneities in a checkerboard pattern. Six experiments have been performed; five with various patch sizes within the mesoscale and one control experiment with homogeneous surface conditions.

In contrast to previous studies on the influence of surface heterogeneity on convective clouds, the adopted modeling setup allows for full interactions between the land surface, clouds and radiation, at high resolution (100 m) and on a large domain (100 km). We showed that clouds counteract the initially higher potential for cloud formation over the warm patches by reducing the available energy at the surface. Hence, simulations without interactive land surface overestimate the surface fluxes below cloudy areas and thus may produce too strong mesoscale circulations.

The transition from shallow to deep convection occurred faster over heterogeneous surfaces; experiments with intermediate patch size (10-25 km) exhibited the fastest transition. Consequently, also the onset of precipitation occurred earlier and the total accumulated precipitation tends to increase with patch size. However, no linear relationship concerning the transition time, precipitation onset and accumulated precipitation compared to the patch size could be determined.

Consideration of the cloud size distribution revealed further effects of the imposed land surface heterogeneity and important differences to homogeneous surface conditions. As over homogeneous surface conditions, the cloud size distribution follows a power law with a scale break at larger scales. During the shallow convective phase and transition phases, the power law remains similar but the scale break shifts to larger and larger clouds with time. The exponent of the power law lies near -2 and is independent of the imposed patch size. As a consequence, the cloud cover during the shallow and transition phases does not vary much between the simulations.

In contrast to the exponent of the power law, the scale break exhibits a clear dependency on the patch size. The scale break indicates the size of the largest clouds. These few but much larger clouds are important for the transition to deep convection as larger clouds entrain less and can more easily deepen and ultimately produce precipitation. The maximum size of the largest clouds at a given time depends on two main factors. On the one hand clouds expand in response to destabilization of the atmosphere caused by the diurnal cycle. This process is independent of the patch size and proceeds at the same pace in all the simulations. On the other hand the clouds feel the effect of the mesoscale circulations triggered by the surface heterogeneity. The convergence of the opposing breeze fronts yields an increase in the vertical velocity and an accelerated cloud development. This process depends upon the patch size. This leads to a faster than normal expansion of the clouds as long as the breeze fronts are converging. When breeze fronts collide the largest cloud size reaches a local maximum followed by a return towards the normal growth rate. This evolution can be found in all simulations but happens earlier in simulations with smaller patch sizes due to a shorter lifetime of the mesoscale circulations. Because clouds are generally larger in experiments with heterogeneous surface conditions, the diagnosed entrainment rate is reduced by up to 30 % as compared to experiments with homogeneous surface conditions. Finally, mesoscale circulations also advect moisture from the cold patches onto the warm patches. This process increases the moist static energy and invigorates convection as a result of larger buoyancy.

The tendency of cloud-resolving models to exhibit a too late onset of precipitation might pinpoint to an incorrect representation of small-scale surface heterogeneity. The intermediate patch size accelerated the onset of deep convection by 75 min, which corresponds to a transition time two thirds that over a homogeneous surface. It is unlikely that the effects of these intermediate scales are properly represented in cloud-resolving models. Following Skamarock (2004), a grid spacing of 2.8 km, as for instance used for operational weather forecasts at the German Weather Service (DWD), would correspond to a effective resolution of about 20 km. On the other hand, large-scale general circulation models need to parameterize convection at all stages of its development. The effects described in this study may be best incorporated in the entrainment formulation as the entrainment rate is often viewed as inversely proportional to the cloud radius.

The complex interplay between cloud size and surface heterogeneity yields three main consequences for the transition from shallow to deep convection.

First, there is no simple relationship between transition time and patch size. The transition time depends upon the relative timing of the converging breeze fronts and the time it would take to transition in the absence of mesoscale circulations. If the collision happens too early or too late, the effects of the breeze on the cloud size and hence on the transition time will be rather modest. The same is true for the onset time of precipitation because the formation of noticeable precipitation requires deep clouds.

Second, the idea that larger clouds always grow faster and more rapidly transition to deep convection does not fully hold over heterogeneous surfaces. The largest clouds grow faster only until they reach a size equal to half the patch size, that is only as long as the breeze fronts have not collided. This means that a simulation that exhibits the largest clouds at a given time may not do so at a later time.

Third, the idea that the cloud size scales with the boundary layer height seems invalid over surfaces with different heterogeneity patch size. During the early stage of cloud development the height is proportional to the patch size and later independent of it. However, the cloud size evolution shows a different behavior. Therefore, convective parameterizations should not use the boundary layer height to determine the maximum cloud size in a given area with heterogeneous surface conditions.

The presented effects of land surface heterogeneity on the transition from shallow to deep convection emphasize the importance of including sub-grid surface conditions in coarser-resolution models to adequately capture the transition between shallow and deep convection.

Chapter 4

The Effect of Moist Convection on Thermally Induced Mesoscale Circulations[1]

4.1 Introduction

The warming of the surface by incoming radiation noticeably depends upon the surface properties. In the presence of surface heterogeneities this leads to the formation of surface temperature gradients and subsequent formation of horizontal temperature gradients in the boundary layer. To balance these gradients, confined mesoscale circulations are frequently observed close to surface boundaries (Pielke and Avissar, 1990). The most common examples of such circulations are vegetation- and sea-breezes. The horizontal extent of these circulations varies between a few and hundreds of kilometers. Because of their significance for local weather prediction, these phenomena have extensively been studied using analytical, observational and numerical methods (see Miller et al., 2003; Crosman and Horel, 2010, for comprehensive reviews). Particular emphasis in previous studies has been on the propagation of thermally induced mesoscale circulations in a dry atmosphere (Rotunno, 1983; Dalu and Pielke, 1989; Wang et al., 1996; Steyn, 1998; Drobinski and Dubos, 2009) and on their effect on the triggering of convection (Lynn et al., 1998; Van Heerwaarden and Vilà-Guerau de Arellano, 2008; Garcia-Carreras et al., 2011; Huang and Margulis, 2011; Kang and Bryan, 2011). The results from modeling studies are supported by various observational studies, for instance in semi-arid regions (Taylor et al., 2007) or over costal areas (Blanchard and López, 1985; Kingsmill, 1995).

---

[1] **Rieck M.**, C. Hohenegger and P. Gentine (2015): The effect of moist convection on thermally induced mesoscale circulations. Q. J. R. Meteorol. Soc., revised.

Despite many studies looking at the effect of the mesoscale circulations on convection, only few studies have asked vice versa how convection modifies a given mesoscale breeze circulation. Segal et al. (1986) studied the effect of cloud shading on mesoscale circulations using a two-dimensional mesoscale model. In their study, clouds were not explicitly simulated but their effect was simply mimicked by reducing the incoming radiation. Using this simplified representation, they found that cloud shading reduces the mesoscale circulation by a factor of two when the incoming solar radiation at the surface was reduced by 60 %. Given their experimental setup this result remains questionable. Lohou and Patton (2014) simulated the effect of shallow cumulus shading at high resolution. They showed that, due to a different surface energy partitioning, clouds strongly reduce the surface temperature while surface evapotranspiration slightly increases. By comparing cloudy and non-cloudy points in Chapter 3, we showed that the sensible heat flux difference between two surface patches was reduced by up to 20 % due to the existence of shallow and congestus clouds over the warmer part of the domain.

Berg and Oerlemans (1985) studied the effect of convection on a sea breeze by using a mesoscale model with simplified cloud physics, but neglected the cloud shading effect. Due to computational constraints, their simulation was limited to shallow non-precipitating convection, two dimensions and four hours of integration. Their work revealed that clouds generally strengthen the sea breeze and that the inland propagation accelerates when clouds are present. Berg and Oerlemans (1985) argued that the propagation accelerates because clouds appear at the landward side of the front and create a horizontal gradient in diabatic heating. Similar studies were conducted by Seitter (1986) and Jacob (1991). Both studies obtained a slower propagation when clouds are present, compared to a dry current of similar depth, and temperature gradient. Despite this inconsistency, the validity of these results is difficult to access because convection was not resolved and important processes such as cloud shading, detailed cloud microphysics or a diurnally varying heat source were missing.

The above mentioned studies did not consider the possible effect of convective precipitation on the characteristics of the mesoscale circulation. Kingsmill (1995) investigated the triggering of secondary convection by the collision of cold pools and a thermally induced mesoscale circulation. Observation over Florida revealed that the cold downdraft induced by deep convection plays an important role in maintaing convective activity after the peninsula-scale forcing has ceased (Cooper et al., 1982; Blanchard and López, 1985). Nicholls et al. (1991) simulated various cases of convection interacting with a sea breeze over the Floridian Peninsula. They observed stronger sea breezes in cases where deep convection and precipitation developed. Along similar lines, Bao and Fuqing (2013) recently showed that cold pool dynamics play an essential role in the propagation and maintenance of convection, triggered by a mountain-plain circulation. Generally, it is well known that cold pools from evaporating and melting hydrometeors excite density currents with potential effects on the subsequent convection formation at the leading edge of the cold pool and on the horizontal organization of convection, effects that have been previously studied over homogeneous surfaces (see e.g. Srivastava, 1987; Rotunno, 1988; Tompkins, 2001; Schlemmer and Hohenegger, 2014). The superposition of a mesoscale breeze system with a cold pool circulation may be important for the development of the circulation, because both phenomena generate a density current and produce vertical lifting at the front of the mesoscale circulation and at the edge of the cold pool, respectively.

The goal of this study is to analyze whether and how deep precipitating convection and especially the downdraft induced density current modifies a preexisting thermally induced mesoscale circulation. Our analysis can be seen as an extension of the problem discussed in Antonelli and Rotunno (2007) and Robinson et al. (2013), where the propagation of idealized density currents in a dry atmosphere has been analyzed. We use a comprehensive large-eddy simulation setup with detailed microphysics, interactive radiation and interactive land surface in an attempt to include all the effects of moist convection on the mesoscale circulation. The simulations are three-dimensional and employ a resolution of 100 m to resolve most of the convective processes and their interactions. The analysis focuses on two main topics. First, we look at the effect of clouds on the circulation by comparing a cloudy with a non-cloudy simulation (Section 4.3.1). Second, we look at the effect of cold pools by studying a perturbed physics experiment where cold pools are suppressed (Section 4.3.2). A simple formulation is proposed to predict the propagation velocity of a mesoscale circulation interacting with precipitating convection (Section 4.4) and compared with results from large-eddy simulations (Section 4.5). Summary and discussion are given in Section 4.6. The next section introduces the modeling setup.

4.2 Methodology

4.2.1 Model Setup

In this study, we use a comprehensive large-eddy simulation (LES) modeling framework including parameterized two-moment bulk microphysics (Seifert and Beheng, 2005), delta-four stream radiative transfer (Pincus and Stevens, 2009) and interactive land surface (see Chapter 2). This modeling framework has been tested and successfully applied to simulate the diurnal cycle of deep convection over oceanic tropical areas in Hohenegger and Stevens (2013), homogeneous continental mid-latitude areas in Schlemmer and Hohenegger (2014) and heterogeneous continental mid-latitude areas in Chapter 3. The configuration of the numerical model (UCLA-LES) used in this study is identical to the one employed in Chapter 3, is described in Chapter 2 and will therefore not be repeated here. In Chapter 3 this configuration is used to study the effect of the surface patch size on the cloud size distribution.

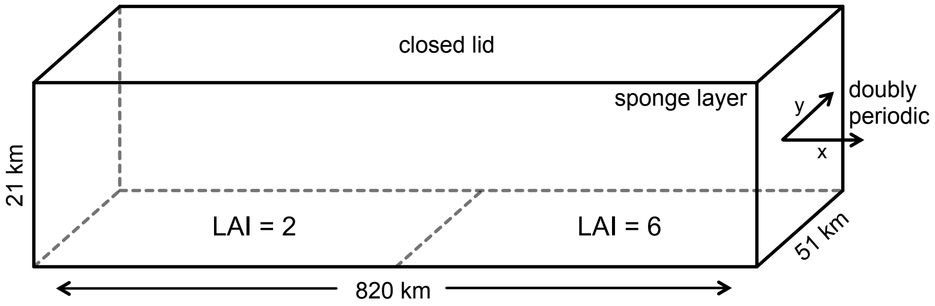

Figure 4.1: Schematic illustration of the experiment setup.

4.2.2 Experiment Setup

The LES simulations are designed to mimic the interactions between diurnally triggered deep convection and thermally induced mesoscale circulations. The computational domain (see Fig. 4.1) contains 8192×512 points in the horizontal and 118 points in the vertical. All simulations are carried out on a doubly periodic grid with a horizontal resolution of 100 m. The grid is stretched in the vertical starting with a resolution of 50 m close to the surface and up to 500 m near the tropopause. The vertical extent amounts 21 km, where the upper 2.5 km of the domain contain a sponge layer to damp gravity waves. Although the computational domain resembles a channel, the simulations are fully three-dimensional because the domain size in y-direction is large enough to allow for several deep convective cells to develop.

Initial conditions are chosen in order to be representative for mid-latitude summertime conditions. We employ the same atmospheric profile as used in Chapter 3 but set the background wind to zero to facilitate the analysis. The model is integrated for one diurnal cycle from 5 LST in the morning to 19 LST in the evening. The data produced by the numerical simulations is stored in xy and xz cross sections. The xy cross sections contain instantaneous values at different height levels, whereas the xz cross sections contain y-averaged data. Both cross sections are outputted every 60 s. Domain averaged time series and profile statistics are stored at 30 s temporal resolution, whereas full 3-dimensional data is only available every 30 minutes.

In order to create an idealized thermally induced mesoscale circulation, the domain is split into two parts with different surface conditions (see Fig. 4.1). The difference between the two land surface types is created by a change in the leaf area index from 2 to 6. The variation is abrupt and yields a sharp interface between a potentially strong evaporating surface on the right that will appear as relatively cold and wet, against a less evaporating surface to the left hand side that will appear relatively warm and dry. As the domain is doubly periodic, there are two interfaces, one located at $x=0$ km and one at $x=410$ km. Both interfaces lead to the formation of a mesoscale circulation that propagates towards the center of the patch with $LAI=2$. For the considered simulation time, the domain is large enough so that the two opposing circulations do not interact. Because the problem is fully symmetric, we concentrate the analysis on the circulation triggered at x=0 km. The remaining characteristics of the land surface (e.g. soil moisture) are homogeneous and as described in Chapter 2 and 3. The effect of precipitation infiltration into the soil is not considered in the modelling framework at this time. This means that we neglect a potential cooling of the surface through the increase of soil moisture from precipitation.

Precipitating convection modifies its environment through the formation of clouds and through the production of precipitation with its associated effects (e.g. downdrafts and cold pools). Therefore, we perform three main experiments to understand the effect of convection on the idealized circulation: one control experiment (CTL) without any modification, one experiment where the full cloud development including precipitation is suppressed (DRY) and one where only the precipitation effects, i.e. cold pools are suppressed (NOCP).

The details of the experiment configurations are important to understand our conclusions in the following sections and are therefore explained next. In NOCP the microphysics routine is modified. The evaporation of hydrometeors is switched off so that the conversion from precipitation to water vapor is impossible. The melting of ice particles is also deactivated to prevent additional cooling from this process. In this setup, the formation of cold pools is thus not possible because the two main processes leading to the formation of cold pools are suppressed. Additional experiments were performed to test the necessity of deactivating the melting of hydrometeors to suppress cold pools. Our analysis confirms earlier results from Srivastava (1987) and shows that the melting of hydrometers is important for the formation of cold pools. The modification of the microphysics has some consequences for the simulations. First, the moistening of the sub-cloud layer by evaporation of precipitation is prohibited. Several studies have shown that this process can be important for further cloud formation over homogeneous surfaces (Tompkins, 2001). However, in the given setup clouds are triggered at the breeze front and grow from warm air ahead of the front (Garcia-Carreras et al., 2011), air that is generally not affected by the cold pool. Second, frozen hydrometeors do not melt when they reach the melting point. This means that most of the precipitation that reaches the surface is classified as graupel; a matter of definition which is not important for our study.

It is important to stress here that the discussed modifications only concern the precipitating part of the microphysics routine. This means that the fundamental processes inside a cloud, such as latent heating, phase changes and precipitation formation, remain unchanged. That is why the modifications do not significantly influence the cloud development in NOCP compared to CTL. This will become clearer in the following sections when the structure and the statistics of convection will be presented. Therefore, the overall effect of our modifications is simply the (artificial) suppression of cold pools.

In DRY, the microphysics routine is switched off completely. This means that water does not condensate once supersaturation is reached but remains in the vapor phase. As a result, the relative humidity is expected to increase compared to the cloudy simu-

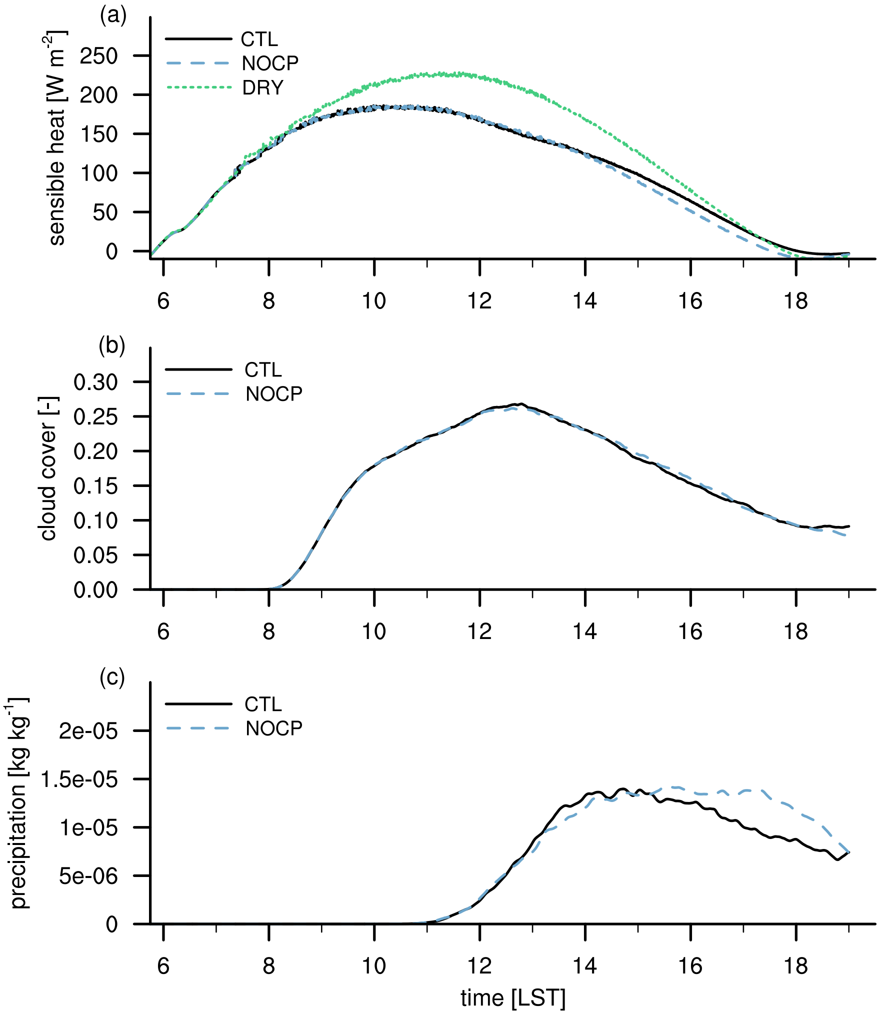

Figure 4.2: Time series of domain mean quantities: (a) surface sensible heat flux, (b) cloud cover and (c) surface precipitation mixing ratio in CTL, NOCP and DRY.

lations. The consequence of this modification is that all moist convective processes are missing and therefore their effect on the thermodynamic structure of the atmosphere is suppressed. As a result, the boundary layer humidity is expected to increase compared to the cloudy simulations because the ventilation of the boundary layer by moist convection is missing.

4.3 Results from Large-Eddy Simulations

Before analyzing the effect of convection on the mesoscale circulation we present the general structure of the simulations. Figure 4.2 shows time series of the domain-averaged surface sensible heat flux, cloud cover and surface precipitation mixing ratio. After an initial spin-up with negligible incoming radiation, the domain-averaged surface sensible heat fluxes rise up to 100 Wm^{-2} at 8 LST and a convective boundary layer

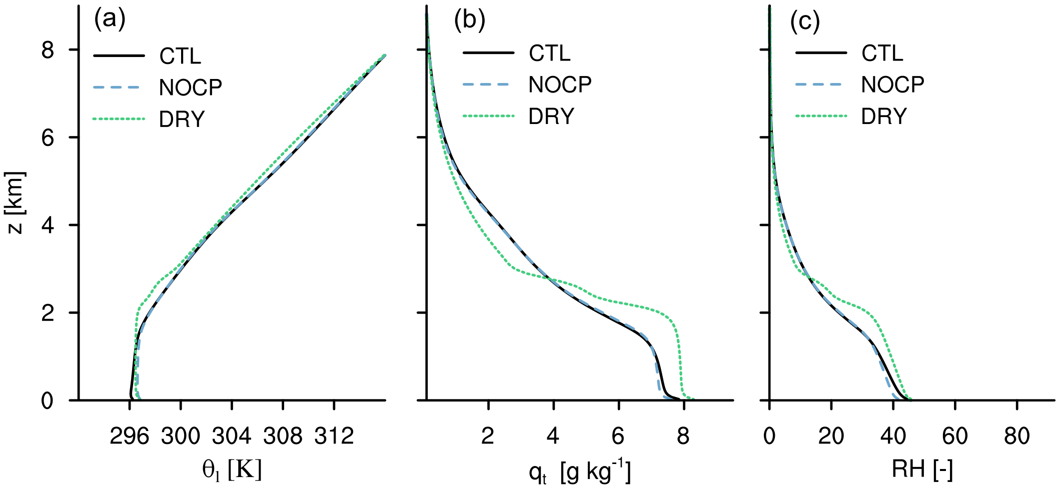

Figure 4.3: Domain mean vertical profiles of (a) liquid water potential temperature, (b) total water and (c) relative humidity at 15 LST.

develops. In the moist simulations (CTL and NOCP) shallow convection appears after 8 LST. As time proceeds, the boundary layer grows, clouds become deeper and reflect more incoming solar radiation. The cloud shading is strongest at 13 LST when the cloud cover reaches its maximum. The difference in mean sensible heat flux due to clouds is about 50 Wm^{-2} at this time, as can be seen by taking the difference between the black (CTL) and green (DRY) curve in Fig. 4.2. The cloud cover reduces after 13 LST because precipitation effectively removes moisture from the atmosphere and because the incoming radiation decreases. The domain mean cloud cover consists of contributions from deep convection and mainly from shallow clouds which are abundant in the entire model domain. Surface precipitation gradually starts after 11 LST and peaks around 14 LST (Fig. 4.2c). Despite the previously discussed modification in the microphysics routine, precipitation and cloud cover develop very similarly both in NOCP and CTL. This confirms that the experimental design in NOCP does not fundamentally change the characteristics of moist convection.

Atmospheric profiles taken at 15 LST are presented in Fig. 4.3 to further illustrate the effects of our modifications. As expected, CTL and NOCP show similar profiles except for a slightly cooler and wetter boundary layer in CTL. Due to the lack of cloud shading and therefore larger sensible heat fluxes in DRY, the boundary layer can heat up faster and is on average 500 m deeper at this time. Parallel to this, the boundary layer specific humidity is 0.7 g kg^{-1} higher in DRY. Two effects cause the higher moisture content. First, the enhanced available surface energy in DRY leads to a higher surface latent heat flux (e.g. +40 Wm^{-2} in DRY compared to CTL at 15 LST). Second, the ventilation of the boundary layer by moist convection is missing. This also suggests weaker dry air entrainment from the free atmosphere into the boundary layer in experiment DRY. In summary, the resulting effect of suppressed convection is a deeper and moister boundary layer that also exhibits a slightly higher relative humidity.

time [LST]	$F_{\text{sens,LAI=2}}$ [Wm^{-2}]	$F_{\text{sens,LAI=6}}$ [Wm^{-2}]	$F_{\text{lat,LAI=2}}$ [Wm^{-2}]	$F_{\text{lat,LAI=6}}$ [Wm^{-2}]
08	159.0	103.7	185.9	253.2
10	220.8	148.6	286.8	395.1
12	205.4	137.3	327.3	444.0
14	149.6	97.4	315.7	428.6
16	85.6	41.6	235.3	333.3

Table 4.1: Surface boundary conditions for experiment CTL at different times. F_{sens} denotes the sensible heat flux and F_{lat} the latent heat flux. The fluxes are shown for each of the two sub-domains with LAI=2 and LAI=6, respectively.

The surface fluxes are not distributed uniformly in space because the domain is divided into two patches with different LAI (see Fig. 4.1). The resulting surface fluxes for the two patches in CTL are listed in Table 4.1. At 10 LST the surface with LAI=2 depicts a 72 Wm^{-2} higher sensible heat flux but a 108 Wm^{-2} lower latent heat flux compared to the surface with LAI=6. This behavior is consistent throughout the simulation, the surface with the lower LAI promotes a stronger heating and weaker moistening of the atmosphere compared to the surface with higher LAI. This reflects a change in Bowen ratio in agreement with a change in LAI. The difference in the buoyancy flux between the two patches induces a temperature difference in the boundary layer. Therefore, a confined mesoscale circulation develops in all experiments and propagates into the warmer fluid (LAI=2). Such a circulation is commonly described as a density current with a well developed head towards the warmer fluid (Rotunno, 1988). The head of the circulation, also known as breeze front, advects colder and moister air as the front propagates into the warmer fluid. Clouds are preferentially located at the breeze front on the warm patch. The propagation speed is defined as the displacement of the front. The location of the front manifests itself by a strong gradient in temperature, moisture and horizontal wind velocity as well as stronger vertical wind velocities. The front is diagnosed in our simulations at the position of the maximum vertical velocity at 500 m height.

Figure 4.4 shows the derived propagation distance of the front for all experiments. The circulation develops around 8 LST and the front starts to propagate similarly in all experiments until 10 LST. From this point in time, both cloudy simulations (CTL and NOCP) increase their propagation speed compared to DRY. 10 LST is about two hours after the first clouds appeared in CTL (see Fig. 4.2b), which suggests that moist convection accelerates the front propagation. After 13 LST, the two simulations CTL and NOCP begin to depart, about 2 h after precipitation started (Fig. 4.2c). The differences in the location of the front in NOCP and DRY at 18 LST compared to CTL are substantial and amount to 53 km in NOCP and 117 km in DRY. Figure 4.4 thus suggests that the formation of convective clouds (10-18 LST) and the formation of

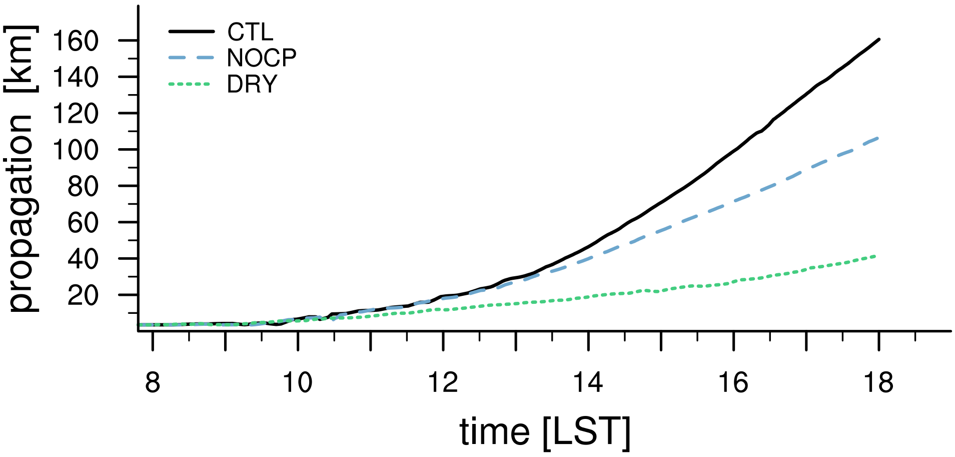

Figure 4.4: Propagation distance of the breeze front for all experiments. The position of the front is diagnosed from y-averaged data available every minute and displayed relative to x=0 km employing a running average over 20 minutes.

cold pools associated with precipitation (13-18 LST) both accelerate the propagation of the thermally induced mesoscale circulation. In the following sections, we discuss the underlying effects responsible for such an acceleration and propose a theory for the propagation speed of the breeze front.

4.3.1 The Role of Clouds

We start by explaining the differences between NOCP and DRY, and disregard the cold pool effects for now. Clouds may influence a preexisting mesoscale circulation through their control on the surface energy budget (cloud shading), as argued in Segal et al. (1986), and trough spinning up an own circulation through convective heating (cloudy dynamics), following the ideas of Berg and Oerlemans (1985) and Seitter (1986).

Cloud Shading

In order to influence the strength and propagation of the mesoscale circulation, the temperature distribution within the boundary layer has to be modified (Benjamin, 1968; Robinson et al., 2013). Clouds preferentially occur over warm surface areas and especially close to land-surface boundaries that create mesoscale circulations. Therefore, cloud shading effects are expected to reduce temperature differences that initially induced the mesoscale circulation, although this effect may strongly depend upon the location of the front.

Figure 4.5 presents vertical cross sections of cloud condensate (NOCP) and virtual potential temperature anomalies (NOCP and DRY) at 12 LST. Generally, on the larger scale the boundary layer temperature follows the surface sensible heat flux pattern; the temperature is higher above the warmer surface (left patch with LAI=2) and lower

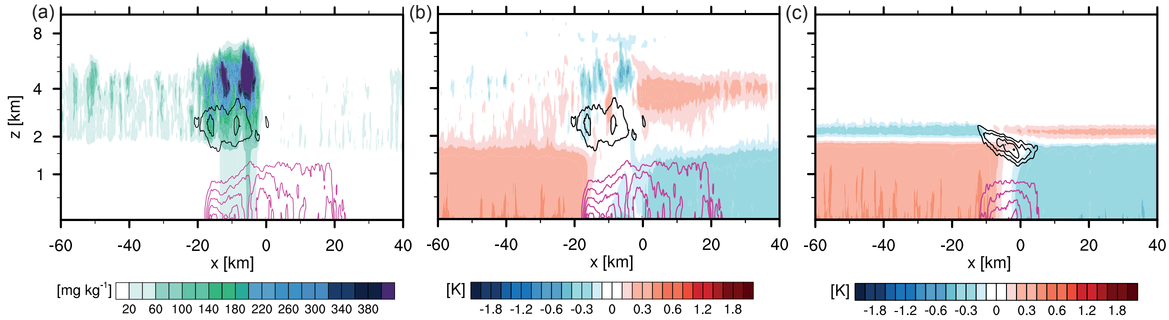

Figure 4.5: Vertical cross section at 12 LST: (a) cloud condensate in NOCP (shaded contours in mg kg^{-1}) and virtual potential temperature anomalies in (b) NOCP and (c) DRY (shaded contours in K). The figures also show horizontal wind velocity (contour lines in 0.5 ms^{-1}, black colors in positive and red colors in negative x-direction). The x-axis denotes the distance to the interface between the two surface patches (Fig. 4.1: x=0), which also depicts the starting location of the front.

above the colder surface (right patch with LAI=6) as compared to the domain mean. At 12 LST, deep convection is located between -20 and -5 km along the x-axis (Fig. 4.5a). The boundary layer temperature is not significantly modified in this particular area, but slightly warmer than the air above the cold part of the domain (Fig. 4.5b). In comparison, the DRY experiment shows a similar behavior, i.e. the temperature anomalies within the boundary layer exhibit the same values as in NOCP, except that the strongest temperature gradient lags behind the front (Fig. 4.5c).

To assess the time evolution of the temperature gradient more quantitatively, Fig. 4.6 shows a time series of the virtual potential temperature gradient. The gradient is calculated from values averaged over 50 km on each side of the front in the horizontal and averaged over the lowest 1500 m in the vertical. The exact position of the front is obtained from the method used to construct Fig. 4.4. As already seen from the vertical cross sections at one time instance in Fig. 4.5, the temperature differences in NOCP and DRY are almost identical during the entire simulation period. This can be explained by the temporal variability of the shading. The location of the shaded areas changes in time due to the rapid movement of the clouds at the breeze front. The cooling is therefore strongly diluted by mixing processes because it is distributed over large areas.

Consequently, the analysis reveals that the shading induced by convective clouds above the front does not significantly influence the propagation of the mesoscale circulation. Note that this has only been tested for our particular case where most of the deep clouds appear in a narrow range at the breeze front and propagate with a pronounced horizontal velocity. The shading by clouds may be more important under stationary conditions where the boundary layer can adopt to the colder surface below the clouds.

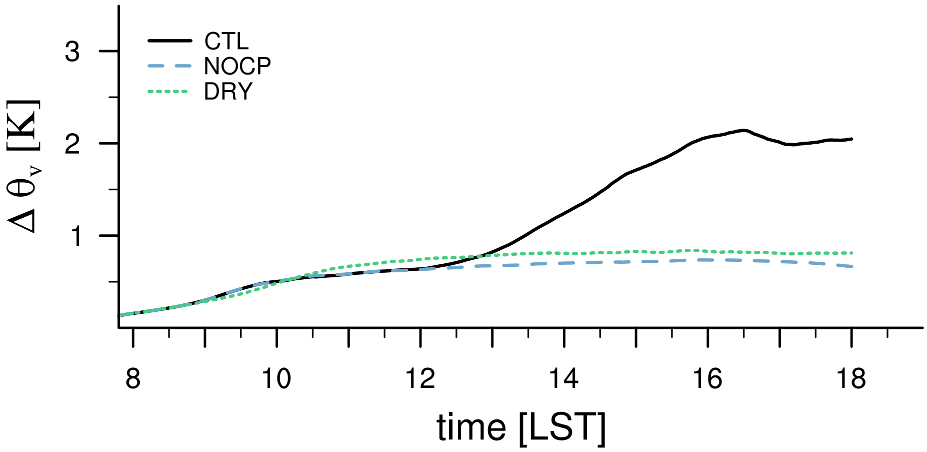

Figure 4.6: Time series of diagnosed virtual potential temperature difference across the front. The difference is calculated from the temperature averaged over 50 km on each side of the front in the horizontal and over the lowest 1500 m in the vertical.

Cloud Dynamics

Besides cloud shading, moist convection also releases latent heat and excites a local cloud circulation. A typical moist convective circulation in the absence of precipitation evaporation is characterized by strong narrow updrafts below and inside the cloud layer and surrounded by weak large scale subsidence. In this paragraph, we evaluate the effect of cloud dynamics on the propagation of the mesoscale circulation.

Figure 4.7a,d shows a snapshot of the circulation of the dry and the cloudy case at 14 LST. In DRY, the mesoscale circulation is shallow because it is capped by the inversion at about 3 km height (see Fig. 4.3). Updrafts of about 0.5 ms^{-1} are triggered at the breeze front and reach up to 2.5 km. A pronounced horizontal return current is observed between 1.5 and 2.5 km height. Above the inversion, the horizontal and vertical motion is insignificant. The general picture is similar to that obtained in previous studies of a breeze circulation in a dry atmosphere (see e.g. Antonelli and Rotunno, 2007; Robinson et al., 2013).

In the cloudy case, NOCP, the picture is completely different at that time. Deep clouds are located just above the front and dissipate on the leeward side of the circulation (see Fig. 4.7c). Updrafts break through the inversion and penetrate deep into the atmosphere because latent heating inside the cloud layer creates a buoyancy excess. This is why the updrafts at the front are much stronger in NOCP compared to DRY and reach to much greater heights. The presence of clouds also influences the characteristics of the mesoscale circulation in NOCP. The circulation is intensified and the front is more pronounced as compared to DRY. This can be seen from the denser contour lines of the horizontal wind at the front, the larger maximum in the vertical wind velocity at the front, and the stronger pressure perturbation at the front in the NOCP experiment compared to DRY. In addition, the return current has merged with the outflow at the top of the cloud layer.

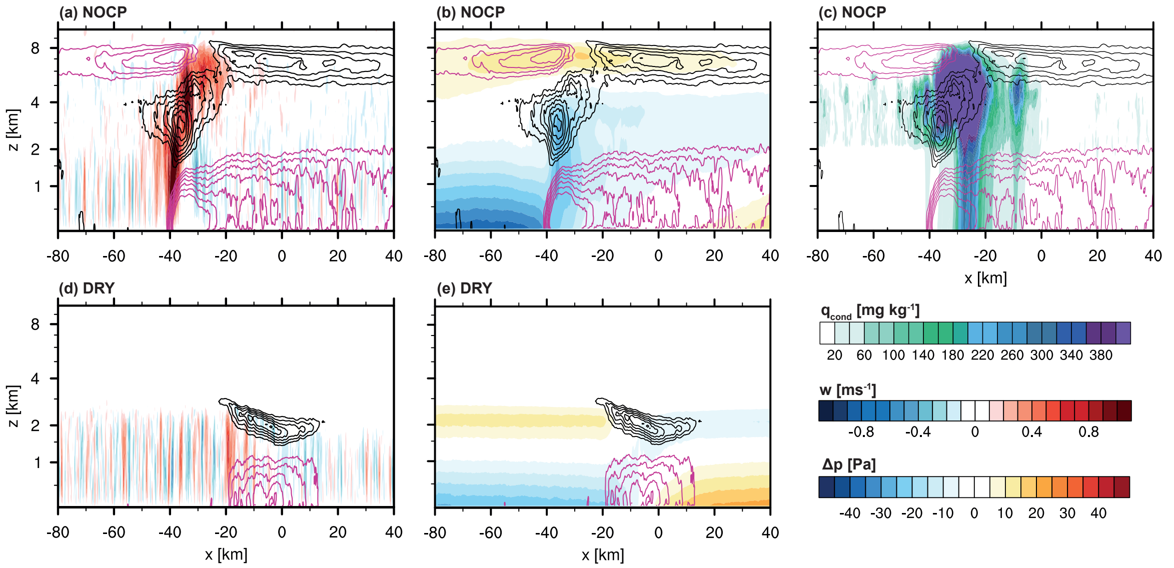

Figure 4.7: Vertical xz cross section of experiments NOCP (a,b,c) and DRY (d,e) at 14 LST: (a,d) vertical velocity (shaded contours in m s^{-1}), (b,e) pressure perturbation, defined as the deviation from the domain mean (shaded contours in Pa), and (c) cloud condensate in NOCP (shaded contours in mg kg^{-1}). All figures also display the horizontal wind velocity (contour lines in 0.5 m s^{-1}, black colors in positive and red colors in negative x-direction). The x-axis denotes the distance to the interface between the two surface patches (Fig. 4.1: x=0), which also depicts the starting location of the front.

It is evident from both snapshots in Fig. 4.7a,d that the propagation distance of the front in NOCP is about twice that of DRY at that point in time. This fact has been shown in Fig. 4.4 and can now be explained. Figure 4.7b,e displays the horizontal pressure perturbation in the area around the front for the two simulations. In both experiments a negative pressure perturbation exists ahead of the front where the fluid is warmer and a positive perturbation behind the front where the fluid is colder. However, the negative perturbation ahead of the front is much stronger in NOCP compared to DRY. This is because the clouds trigger stronger updrafts and effectively lift the air out of the boundary layer into the free atmosphere just ahead of the front. The condensation process in NOCP creates a buoyancy excess within the cloud layer and is the fundamental reason why updrafts are more intense and break through the boundary layer. Updrafts are not observed in the cold air behind the front, which is also a typical characteristic of synoptic cold fronts. The updrafts only draw warm air from ahead of the front and distribute it into the cloud layer where it is diffused into the free atmosphere. The lifting of boundary layer air causes convergence ahead of the front and increases the horizontal pressure gradient that drives the circulation. This dynamical forcing accelerates the propagation of the front.

Although we only presented the circulation at one instance in time, this explanation holds for the whole simulation. In the early morning when no clouds are present, both experiments depict the exact same structure and magnitude of the circulation.

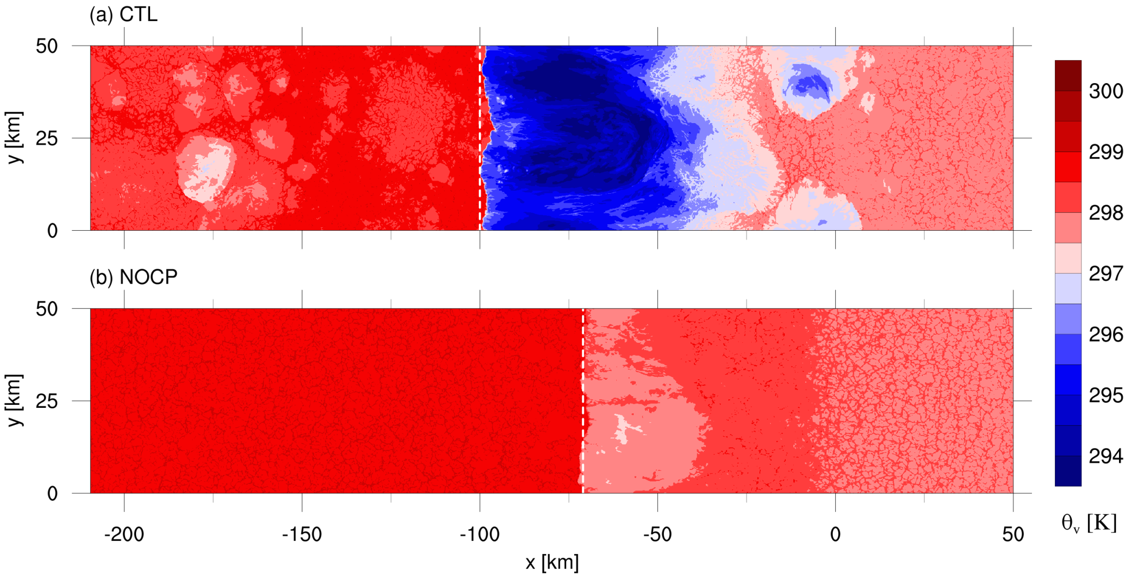

Figure 4.8: Horizontal cross section of virtual potential temperature close to the surface (z=125 m) at 16 LST for (a) CTL and (b) NOCP. The dashed white line represents the location of the front as shown in Fig. 4.4. The x-axis denotes the distance to the interface between the two surface patches (Fig. 4.1: x=0), which also depicts the starting location of the front.

Later, when clouds appear above the front, the circulation is intensified and stretched vertically in the cloudy simulation, whereas it remains weak and shallow in the dry case. When convection becomes stronger during the day, the dynamic effects also increase, which explains the diverging propagation distance between the cloudy and the dry experiments (Fig. 4.4).

4.3.2 The Role of Cold Pools

Another peculiar effect of convection on the mesoscale circulation and its propagation arises from the formation of cold pools. We compare the CTL experiment with the NOCP experiment where cold pools are suppressed by design.

In both simulations, precipitation starts around 12 LST, reaches a maximum and slowly decreases towards the evening (Fig. 4.2c). The location of the precipitation maxima lags the front because deep convection is constantly triggered at the front (Fig. 4.7c). In CTL, part of the falling precipitation constantly evaporates in the sub-saturated boundary layer and creates a deficit in virtual potential temperature, the cold pool. This cooling can clearly be seen in Fig. 4.8a, which shows a xy cross section of virtual potential temperature close to the surface. In contrast, such a strong cooling is absent when cold pools are suppressed, as in NOCP (Fig. 4.8b). The area behind the front that is affected by the cold pools is about 50 km. This can clearly be attributed to a series of continuously generated cold pools behind the front. In CTL the maximum temperature

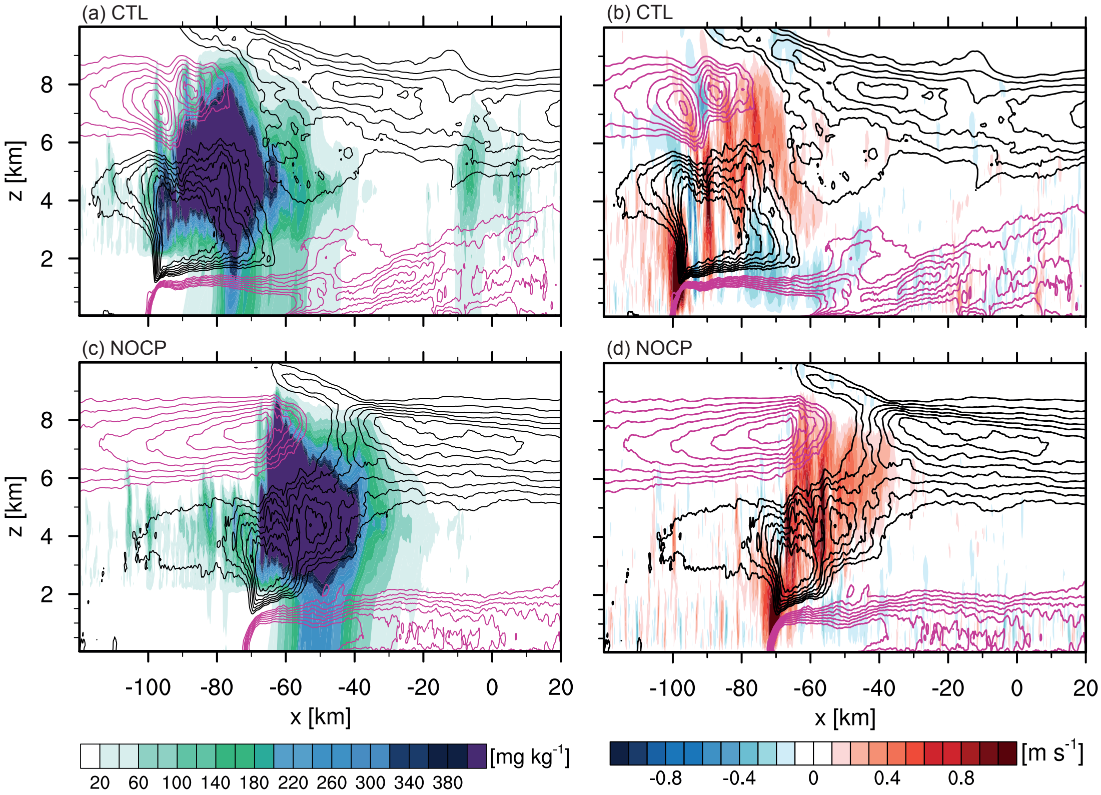

Figure 4.9: (a,c) Cloud condensate (shaded contours in mg kg^{-1}) and (b,d) vertical velocity (shaded contours in m s^{-1}) for the experiments CTL and NOCP at 16 LST. All figures also display the horizontal wind velocity (contour lines in 0.5 m s^{-1}, black colors in positive and red colors in negative x-direction). The x-axis denotes the distance to the interface between the two surface patches (Fig. 4.1: x=0), which also depicts the starting location of the front.

gradient between the center of the cold pool and the environment is about 5 K at this time which is a typical value for cold pools (see e.g. Schlemmer and Hohenegger, 2014), whereas the temperature gradient induced by the surface heterogeneity is only about 0.6 K in NOCP. The time evolution of the mean boundary layer temperature gradient has already been assessed in the previous section (Fig. 4.6). While DRY and NOCP exhibit the same values, CTL shows a strong increase when precipitation starts to fall. This underlines that the temperature gradient in CTL is dominated by the cold pool effect after 1230 LST.

Despite the differences in temperature, the cloud structure is very similar in both NOCP and CTL (Fig. 4.9a,c). An area of deep convection is located at the front with the precipitation maximum lagging 20 km behind the front. Deep convective clouds appear in a different horizontal position in CTL because the breeze front is advanced by about 30 km compared to NOCP. A particular difference between CTL and NOCP is also the area of the downdraft behind the front. While the downdraft is strong and well pronounced in CTL (Fig. 4.9b between -80 and -50 km), it is weaker in NOCP (Fig. 4.9d between -60 and -40 km). The cold downdraft mass flux in CTL takes over part of the return circulation, whereas the return circulation in NOCP is connected to the cloud top outflow and a larger scale subsidence behind the front. The strength of the downdraft mass flux in CTL is constrained by microphysical processes and the boundary layer humidity.

How does the cold air influence the mesoscale circulation? As over homogeneous surfaces, the buoyancy difference created by the cold pool triggers a circulation (Rotunno, 1988). Both the existing mesoscale and the cold pool circulation superimpose in the positive mode because the location of both phenomena coincide. In contrast to the dynamical effect of clouds, cold pools exert a thermodynamical effect on the circulation. Because the temperature perturbation induced by the cold pool is much stronger than the one created by the background surface heterogeneity, the front accelerates significantly. This also confirms that the two simulations can only begin to diverge when precipitation starts to fall and cold pools become strong enough.

In our experiments cold pools are constantly triggered at the front and decay towards the colder side. In opposition to homogenous surface conditions without a background mesoscale circulation, under heterogeneous surface conditions the cold pools propagate in the direction of the front because the background mesoscale circulation imposes a preferred orientation. The problem is different to squall line propagation predicted by RKW theory (Rotunno, 1988) because in our case the preferred propagation direction is enforced by the land surface discontinuity.

4.4 Extension of the Density Current Formulation

4.4.1 Theory

This section aims at formulating a simple theoretical model to predict the propagation speed of the front based on the mechanisms highlighted in Section 4.3. The propagation of the mesoscale breeze front shows three distinct phases. First, the dry convective phase where the temperature gradient due to the different land surface characteristics builds up and a local circulation is established. Second, an accelerated propagation when moist convection becomes significant and a cloud base mass flux exists but unsaturated downdrafts and cold pools are not yet significant. And finally a third phase with a further acceleration of the propagation as a result of an enhanced temperature gradient at the surface due to cold pool activity. The latter phase is driven by a thermodynamical effect like the dry convective phase because cold pools are nothing else than cold air propagating into warmer air. This is not true for the second phase which is linked to a dynamical effect. The propagation speed of the front, c_*, results from the sum of these two effects:

$$c_* = c_{*,\mathrm{thermo}} + c_{*,\mathrm{dynamic}} \tag{4.1}$$

The propagation speed, $c_{*,\text{thermo}}$, describes the circulation induced by the temperature gradient, whereas $c_{*,\text{dynamic}}$ describes the additional effect on the propagation speed by the moist convective updraft mass flux. The LES sensitivity experiments presented in Section 4.3 revealed that we can separate the two effects. As a starting point, Eq. 4.1 assumes that the two effects are independent from each other and can thus be linearly added. Although some nonlinearities have to be expected, the results in sections 4.3.1 and 4.3.2 give justification for our assumption. In particular the cloud dynamical effect does not alter the temperature difference across the front, whereas the dry circulation and cold pools primarily affect the temperature difference. The presence of cold pools can in theory affect the convective updraft mass flux but this effect seems small as NOCP and CTL display similar $c_{*,\text{dynamic}}$ (see Section 4.2 and Fig. 4.11e). This motivates the first order assumption of the Galilean addition of both velocities.

The thermodynamic part can be described as a classical density current with two fluids of different temperature. The density current theory has been successfully applied to mesoscale circulations and is supported by numerical studies and observations. Benjamin (1968) and later Rotunno (1988) showed that the propagation speed of such a density current depends on the height of the cold fluid and the temperature difference between the cold and warm fluid. Hence we may write:

$$c_{*,\text{thermo}} = k_1 \sqrt{g \; h \; \frac{\Delta\theta_v}{\theta_{v,00}}} \tag{4.2}$$

where h denotes the height of the cold fluid, $\Delta\theta_v$ the virtual potential temperature difference between the two fluids, $\theta_{v,00}$ is the mean temperature of the warm fluid, g the gravitational acceleration and k_1 a proportionality constant, the internal Froude number. Equation 4.2 has also been used over homogeneous terrain to infer the propagation velocity of cold pools (Ross et al., 2004; Knippertz et al., 2009; Schlemmer and Hohenegger, 2014).

A similar reasoning does not apply to $c_{*,\text{dynamic}}$. In Section 4.3, our numerical simulations showed that both cloud shading and convective heating do not significantly influence the temperature gradient across the front. However, dynamical effects associated with strong updrafts at the front causing a pressure drop ahead of the front are responsible for the acceleration of the front. An equation like Eq. 4.2 cannot describe this dynamical effect because the buoyancy increase in the cloud layer and the resulting convective updrafts are neglected (see Rotunno, 1988). The convective updrafts are neglected in the classical density current formulation because there is an assumed lid on the top of the boundary layer.

Instead, we approximate the additional term $c_{*,\text{dynamic}}$ by mass conservation within the sub-cloud layer ahead of the front. The situation is illustrated in Fig. 4.10. Air ahead of the front is sucked from the boundary layer into the cloud layer. This flux is then balanced by horizontal convergence in the boundary layer. The convergence accelerates

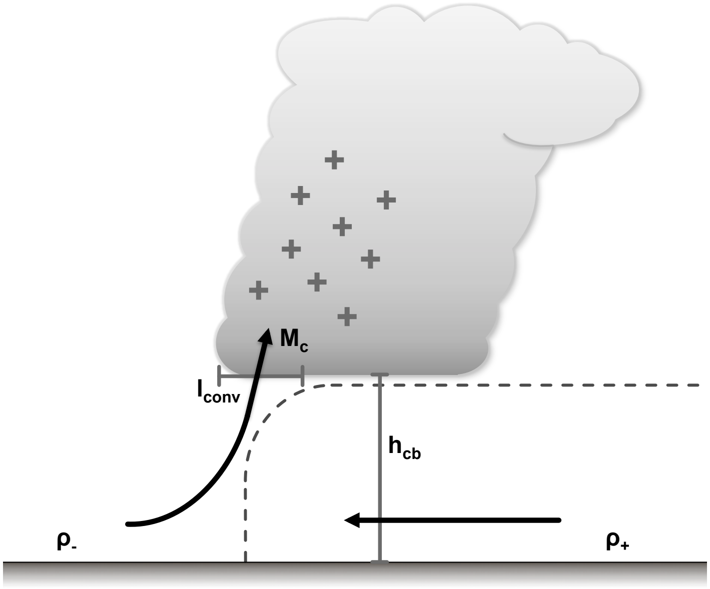

Figure 4.10: Schematic illustration of the cloud circulation at the breeze front, the warm air towards the left and the cold air towards the right. Arrows denote the cloud base mass flux and the horizontal flux at the front, the dashed line indicates the position of the breeze front. The markers indicate the area where convective heating is strong.

the front in the direction of the propagation because the pressure gradient force points from the colder fluid towards the warmer and because the cold air is already moving in this direction, whereas the warm air ahead of the front is stagnant. The continuity equation ($\nabla[\rho\vec{u}] = 0$) is integrated in a tube along the front. Assuming symmetry in the y-direction yields:

$$\rho_{\mathrm{warm}}\ w\ l_{\mathrm{conv}} = \rho_{\mathrm{cold}}\ u\ h_{\mathrm{cb}}. \tag{4.3}$$

In our 2-dimensional problem, l_{conv} convective length scale in the horizontal and h_{cb} the cloud base height at the front. The product of the vertical velocity, w, with the convective length scale, l_{conv}, is the cloud base mass flux per unit width, M_{c}. The horizontal velocity scale u is the additional propagation, $c_{*,\mathrm{dynamic}}$, induced by the cloud circulation. Thus, Eq. 4.3 can be rewritten as

$$c_{*,\mathrm{dynamic}} = k_2\ \frac{\rho_{\mathrm{warm}}}{\rho_{\mathrm{cold}}}\ \frac{M_{\mathrm{c}}}{h_{\mathrm{cb}}}. \tag{4.4}$$

The density of the warm and the cold fluid are denoted by ρ_{warm} and ρ_{cold}, respectively. We introduced a proportionality constant k_2 because the cloud base mass flux may also contain part of the dry circulation and friction is not considered. Equation 4.4 reveals that the additional acceleration by convective clouds, $c_{*,\mathrm{dynamic}}$, is essentially given by the cloud base mass flux weighted by the cloud base height.

The superposition of the density current formulation (Eq. 4.2) and the cloud circulation (Eq. 4.4) yields the final form for the propagation speed of the mesoscale circulation:

$$c_* = k_1 \sqrt{g \; h \; \frac{\Delta\theta_v}{\theta_{v,00}}} + k_2 \; \frac{\rho_{\mathrm{warm}}}{\rho_{\mathrm{cold}}} \; \frac{M_{\mathrm{c}}}{h_{\mathrm{cb}}} \; \approx k_1 \sqrt{g \; h \; \frac{\Delta\theta_v}{\theta_{v,00}}} + k_2 \; \frac{M_{\mathrm{c}}}{h} \tag{4.5}$$

The propagation speed depends on the virtual potential temperature gradient between cold and warm air, the height of the cold fluid and the cloud base mass flux ahead of the front. A faster propagation may be caused by an increased temperature gradient or an intensification of convection above the front, i.e. the cloud base mass flux. In the simplified form of Eq. 4.5 it is assumed that the ratio between ρ_{cold} and ρ_{warm} as well as the ratio between h_{cb} and h are unity. The derived equation is applied to the results obtained from large-eddy simulations in the next section.

4.4.2 Application to LES Results

Equation 4.5 proposes an approximation for the propagation speed of mesoscale breeze fronts including the effect of moist convection. The different terms in Eq. 4.5 are diagnosed from the LES to compute the theoretical propagation speed (Fig. 4.11b), which is then compared to the propagation speed diagnosed directly from LES (Fig. 4.11a and Fig. 4.11c).

In order to compute the theoretical propagation speed, the two velocity terms, $c_{*,\mathrm{thermo}}$ (Fig. 4.11d) and $c_{*,\mathrm{dynamic}}$ (Fig. 4.11e), are estimated from the LES experiments. All data used to calculate the two terms is averaged in the y-direction and available every minute. Following the simplified form of Eq. 4.5, this requires computing the horizontal temperature difference between the two fluids, the height of the colder fluid, and the cloud base mass flux at the front. The temperature difference across the front, $\Delta\theta_v$, is calculated from the temperature averaged horizontally over 50 km on each side of the front and vertically over the depth of the cold fluid. We chose to average horizontally over 50 km because this is the maximum horizontal extent of clouds (see Fig. 4.9a,c) and cold pools (see Fig. 4.8) in the simulations. This choice assures that we capture the mean effect of cloud shading and cold pools, although we might average out some fluctuations due to smaller clouds and smaller cold pools. For simplicity, the height of the density current h is fixed to a value of 1.5 km, which is also used for the vertical averaging of the temperatures and the diagnosis of the cloud base mass flux. The height has been identified as the characteristic vertical extent of the cold fluid throughout the simulations. It can be clearly recognized by the rapid change in the sign of the temperature anomaly at a certain height (see e.g. Fig. 4.5b). The actual height is, however, lower in the morning hours (8-10 LST) when the boundary layer is not yet fully developed. The cloud base mass flux is computed as the product of the vertical velocity at cloud base w and the convective length scale l_{conv}. The typical updraft size, whereby an updraft is defined as the region of positive vertical velocity adjacent to the

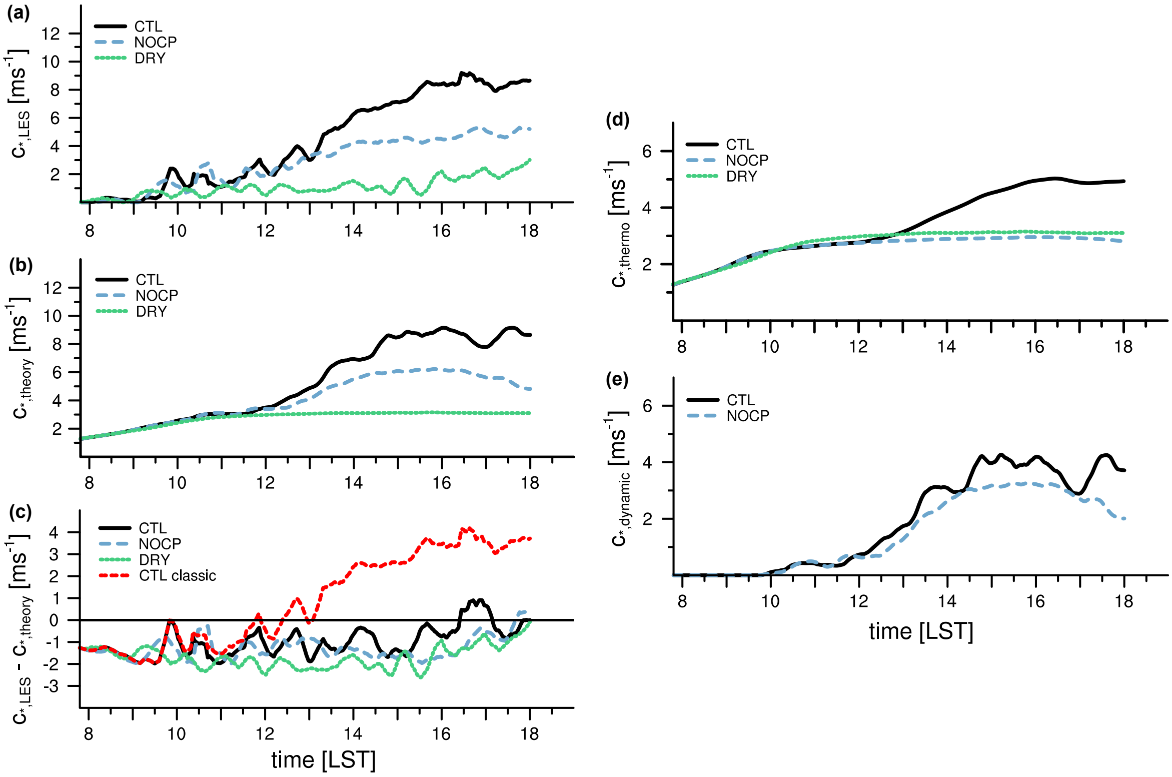

Figure 4.11: Time series of (a) propagation velocity of the front diagnosed from LES, $c_{*,\mathrm{LES}}$, (b) propagation velocity predicted from Eq. 4.5, $c_{*,\mathrm{theory}}$, (c) velocity difference between the diagnosed values ($c_{*,\mathrm{LES}}$) and the theoretical values ($c_{*,\mathrm{theory}}$), (d) thermodynamical contribution calculated from Eq. 4.2, and (e) dynamical contribution calculated from Eq. 4.4. Quantities are diagnosed from y-averaged data available every minute employing a running average over 20 minutes. Detailed assumptions for the computation of the different terms are given in the text.

front location, amounts to 5 km (see e.g. Fig 4.9b,d). l_{conv} is thus fixed to a value of 5 km. This choice is justified because in our particular problem the updraft is well defined at the front and the horizontal averaging inhibits large fluctuations (w is also averaged over these 5 km). The proportionality constant k_1 is set to 0.5, whereas k_2 is set to 0.97. The value for k_1 is close to the one determined by Seitter (1986) from data of 20 observed density currents. The values for k_1 and k_2 are chosen such that $c_{*,\mathrm{theory}}$ matches $c_{*,\mathrm{LES}}$ towards the end of the simulation (18 LST).

As expected from Section 4.3, $c_{*,\mathrm{thermo}}$ shows similar values for DRY and NOCP because the temperature gradient is the same for both simulations. In CTL, the velocity diverges after 1230 LST due to a strong increase in $\Delta\theta_v$ and keeps increasing between 13 and 16 LST. The behavior of CTL can clearly be attributed to the occurrence of cold pools that develop behind the mesoscale front.

In the morning when convection is shallow, $c_{*,\mathrm{dynamic}}$ (Fig. 4.11e) is negligible because the cloud base mass flux at the front is rather small. Around 11 LST, the transition from shallow to deep convection (cloud tops above 5 km) happens in both CTL and

NOCP, and after 1130 LST $c_{*,\mathrm{dynamic}}$ increases significantly. The largest values are observed in the early afternoon with values of around 3 ms^{-1}. Both simulations exhibit similar values in agreement with the fact that our modifications in NOCP did not fundamentally alter convection and justifying our linearity assumption in Eq. 4.1. Per definition, $c_{*,\mathrm{dynamic}}$ is zero in DRY. Comparing c_* and $c_{*,\mathrm{dynamic}}$ reveals that $c_{*,\mathrm{dynamic}}$ contributes significantly to c_* and explains the differences between DRY and NOCP.

Figure 4.11a,b shows the total propagation speed directly diagnosed from LES and the propagation speed calculated with Eq. 4.5. Comparison of the propagation speeds reveals good agreement between the theoretical and the diagnosed values (see Fig. 4.11c). The order of magnitude, the differences in magnitude between the three experiments and the time evolution are similar although the actual values are overestimated in the theoretical formulation. Given the various assumptions, the degree of agreement is nevertheless remarkable. The improvement may be seen by comparison of the red and the black line in Fig. 4.11c. The red line represents the difference in propagation velocity, once diagnosed for CTL and once computed with the classical formula for density currents (Rotunno, 1988), which only accounts for the thermodynamical effect. Tuning of the constants k_1 and k_2 in our Eq. 4.5 could give a better agreement between Fig. 4.11a and Fig. 4.11b. The overestimation of c_* in the early hours of the simulations is due to the chosen fixed value of 1.5 km for h. In reality, the cold fluid needs to deepen in the beginning because the simulations start from a homogeneous temperature distribution.

The analysis shows that the observed differences in the diagnosed propagation between DRY and NOCP are attributed to moist convection, whereas the differences between NOCP and CTL are related to the cold pool effect. Note that the averaging process in y-direction influences the statistics and makes the transition between the wake of the current and the environmental air less sharp and well defined. Nevertheless, the derived relationship also holds for data that is not averaged in y-direction (not shown). The deduced relationship is a good explanatory model and can capture the main differences between the propagation of the different experiments, even though it is not expected to match perfectly with the simulated velocities from LES.

4.5 Summary and Discussion

In this study, large-eddy simulation is used to understand the effect of moist convection on an idealized thermally induced mesoscale circulation. Simulations with typical mid-latitude summertime conditions and a well-defined land-surface gradient are integrated for one diurnal cycle. A mesoscale circulation develops at the temperature boundary between cold and warm fluids and persists throughout the day. Deep convection and precipitation is shown to continuously develop at the breeze front starting at noon. Sensitivity experiments with perturbed model physics are performed to understand the effect of convective clouds and cold pools on the background mesoscale circulation.

First, the microphysics routine is modified to suppress the formation of cold pools from evaporating and melting hydrometeors. The analysis shows a strongly reduced propagation of the breeze front when cold pools are suppressed. This is due to the fact that cold pools cool the fluid behind the front, enhance the temperature gradient across the front and thus enhance the propagation velocity.

Second, the microphysics routine is switched off and cloud development is suppressed entirely. Again, a mesoscale circulation develops in the cloud-free atmosphere, but with a weaker strength and a considerably slower front propagation compared to the cloudy experiments. The intensification of the circulation in the cloudy case cannot be attributed to the shading effect of clouds because the horizontal temperature gradient is not modified by the presence of clouds. Instead, strong vertical motion induced by convective clouds is found to be the dominant mechanism that intensifies the mesoscale circulation. The horizontal pressure gradient across the front increases because clouds appear at the breeze front and effectively lift air ahead of the front. The combination of these thermodynamical (cold pools) and dynamical (cloud lifting) effects yields three conceptual stages that determine the temporal evolution of a thermally induced mesoscale circulation influenced by moist convection: The dry onset, the moist convective acceleration and the cold pool intensification (see Fig. 4.12 for a conceptual overview).

A simple formula is presented to describe the cloud dynamical and thermodynamical effect on the propagation of the breeze front (Eq. 4.5). Large-eddy simulations reveal that the thermodynamical and the cloud dynamical effect can be separated and that the combination of the two effects yields the total propagation speed. The classic formula for density currents accounts for the thermodynamic effects underlying the dry and the cold pool circulations. Additionally, the cloud base mass flux is proposed as a proxy for the dynamical effect of clouds on the pressure gradient force. Comparison with results from our numerical simulations shows a qualitatively good agreement between the predicted and the diagnosed propagation speed and confirms our explanations.

The focus of this Chapter is on process understanding and on the elaboration of the underlying physical effects. The sensitivity of the results to atmospheric background conditions and to the strength of the surface heterogeneity has not been assessed. Additional simulations were performed to test the sensitivity to domain and patch size. A simulation with a four-times smaller patch size showed the same behavior of the breeze front as the presented experiments. However, because of the smaller patch size, the opposing propagating breeze fronts collide, disrupting the effects described in this study. Optimal conditions for a strong impact of convection on a preexisting circulation may thus be: a moist and unstable atmosphere (strong convection), a weak background wind, and a large patch size with a weak heterogeneity amplitude (weak background circulation). A continental land-sea breeze system is a good example for such an optimal situation because the length scales are large and the mesoscale circulation develops slowly. Beyond process understanding, the presented results have some

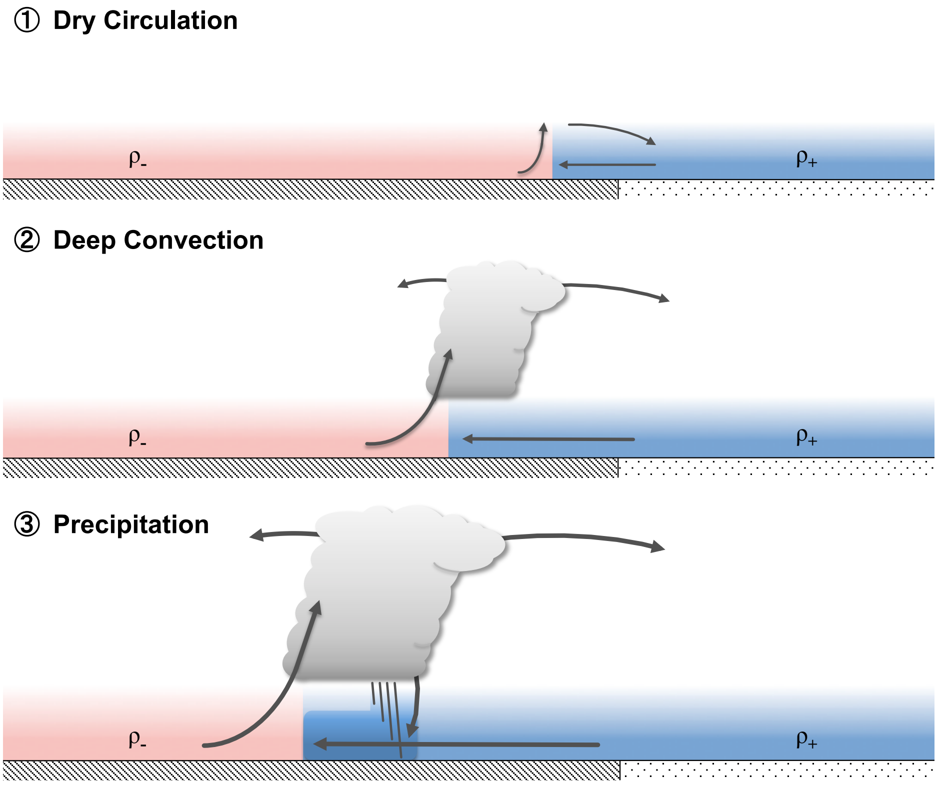

Figure 4.12: Conceptual stages of a mesoscale circulation interacting with precipitation convection: 1. Dry convective circulation, 2. enhanced propagation and vertical stretching and 3. acceleration due to cold pool activity behind the front.

important implications for mesoscale circulations.

The strength and propagation velocity of mesoscale circulations critically depends on the stage of convective development, on the location of the clouds and especially on the updraft and downdraft mass fluxes. This is an important finding for numerical weather prediction and climate modeling because local phenomena such as circulations and convective clouds are often poorly represented. Therefore, the prediction of convection associated with such circulations may fail.

The transition to precipitating deep convection and the subsequent formation of cold pools further amplifies the effect of clouds. The perturbations induced by cold pools are significantly stronger than those induced by the surface heterogeneity itself. This suggests that static surface heterogeneity becomes less important once cold pools can develop. Nevertheless, static surface discontinuity is essential to initially trigger a mesoscale circulation with a fixed propagation direction and a cloud development at the front of the circulation.

In addition, the faster propagation of the breeze front by convection may have positive effects on the local climate in costal regions, e.g. by improving air quality in costal areas due to the faster inland propagation of clean maritime air masses.

Chapter 5

The Interaction Between Static and Dynamic Land Surface Heterogeneities

5.1 Introduction

Surface properties that do not change on timescales beyond the diurnal cycle are defined as static heterogeneities. Prominent examples are vegetation characteristics or soil type. The effect of static surface heterogeneities on cloud size has been discussed in Chapter 3. It was found that static land surface heterogeneities have a profound influence on the organization and size distribution of deep convective clouds.

In contrast, dynamic heterogeneities induce temporal variability in the surface fluxes on timescales beyond the convective diurnal cycle. Clouds induce dynamic heterogeneities by shading the Earth surface on time and length scales related to the convective lifecycle (see Chapter 3). This heterogeneity type exhibits weak memory because cloud shading disappears when clouds dissolve and the soil heat capacity is small. Another classic example of a dynamic heterogeneity is the soil moisture, with memory due to the history of evaporation and precipitation. The effect of soil moisture on convection has been analyzed in several studies (Chen and Avissar, 1994; Clark and Arritt, 1995; Emori, 1998). The results suggest a non-linear behavior with complex interactions on different scales. In particular, Emori (1998) found a coupling between soil moisture and precipitation so that a heterogeneous soil moisture distribution is maintained. In this chapter we investigate the relative role of both static and dynamically induced surface heterogeneities. We elucidate the formation mechanisms of the dynamic patterns and relate their impact on the further convective development to the influence on static patterns.

The coupling between surface precipitation and soil moisture was not included in the model setup in Chapter 3. Thus, surface precipitation could not influence the available soil moisture and thus the Bowen ratio. This assumption was legitimate in Chapter 3 because we analyzed processes on time scales shorter than one diurnal cycle and focused on the analysis before precipitation sets in. However, on longer timescales, convection feeds back on the surface through the infiltration of precipitation into the soil. This feedback changes the surface energy balance because soil moisture influences the evaporative fluxes. Therefore, patterns of different soil moisture promote dynamic heterogeneities in the sense that they appear abruptly and modulate the surface fluxes on timescales beyond the diurnal cycle.

Moisture availability is an important prerequisite for convection and precipitation formation over land. Several studies have assessed the coupling mechanism between soil moisture and precipitation with models and observations (Findell and Eltahir, 2003; Clark and Taylor, 2004; Hohenegger et al., 2009; Taylor et al., 2011; Schlemmer et al., 2012; Froidevaux, 2014). It was found that the sign and strength of the feedback depends on the treatment of convection (Hohenegger et al., 2009) and on the background wind (Froidevaux, 2014), and is strongest at the mesoscale (Clark and Taylor, 2004; Schlemmer et al., 2012). Generally, one should differentiate between spatial and temporal scales: While mesoscale circulations force a mostly negative coupling on a local scale, the coupling is mostly positive in time. This means that precipitation occurs locally in areas where the soil is drier compared to its surrounding (circulation and buoyancy advantage), but temporarily more precipitation is expected in regions with higher average soil moisture (moisture advantage).

The above mentioned studies have investigated the coupling in setups, where effects of static and dynamic heterogeneities are difficult to isolate, or in idealized setups considering only one of the two effects. Little attention has been paid to the modulation of preexisting static surface heterogeneities by dynamic processes such as soil moisture. In this chapter, we study long-term large-eddy simulation (LES) experiments with prescribed static surface heterogeneity. The behavior of dynamic heterogeneities is implicitly included in the formulation of our land surface model. Sensitivity experiments are performed where the coupling between precipitation and soil moisture is switched off. This helps isolating the effects of dynamic surface heterogeneity on the surface flux distribution. The degree to which convective precipitation is organized is an important process in this problem. Organized precipitation may create new local gradients or simply homogenize the surface fluxes. The purpose of this study is to understand these mechanisms, to identify dominant time and length scales related to such dynamic heterogeneities and to determine under which situations they are important.

We introduce the model and experiment setup in the next section. A convective quasi-equilibrium state is introduced in Section 5.3, while the feedback from convective precipitation is analyzed in Section 5.4. In Section 5.5, the results are summarized and discussed.

5.2 Methodology

5.2.1 Large-Eddy Simulation Setup

UCLA-LES is used as described in Chapter 2 with the full microphysics, radiation and surface parameterization package. The domain size is 256 × 256 km^2 in the horizontal and 22 km in the vertical. Because the simulations are integrated for several diurnal cycles and in a large domain, the computational cost is considerably higher compared to the experiments discussed in Chapter 2, 3 and 4 (where the horizontal grid size was 100 m). For this reason, we increase the horizontal grid size from 100 to 1000 m and likewise increase the vertical grid size in the boundary layer from 25 to 100 m. We are aware that the chosen vertical resolution is not ideal for coupling with our land surface model, especially for near surface gradients, because the first grid point is at 50 m. Given the requirements for domain size and integration time, it was necessary to reduce the number of points in both vertical and horizontal direction.

Given the coarser resolution, the simulations cannot resolve the turbulent eddies and will thus neglect part of the turbulent spectrum. The sub-grid turbulence scheme compensates for part of these unresolved scales because it has a scale adaptive component given by a turbulent length scale that increases with grid size (Beare, 2013). It is a well-known issue that at such resolutions, shallow clouds are not fully resolved, whereas deep clouds are explicitly resolved. The effects of resolution on turbulence and shallow clouds are also discussed in Cheng et al. (2010). Using UCLA-LES, they show that the sum of resolved and unresolved kinetic energy remains similar for simulations with different horizontal resolution between 100 and 2000 m, although the resolved scales become larger. Generally, small-scale turbulent structures strongly depend on model resolution, whereas bulk properties of the flow become independent of resolution (Langhans et al., 2012). Since we are interested in precipitating deep convection with typical length scales much larger than the grid spacing, we are confident that it is justified to use such coarse resolution.

In this chapter, we investigate the ability of surface precipitation to dampen or completely remove static surface heterogeneities. Surface precipitation may depend on atmospheric background conditions, large scale forcing, surface properties (e.g. static heterogeneity length scale) and the numerical model. Instead of investigating the full parameter space, we study some well defined cases where the impact of dynamic heterogeneity may be maximized (see below).

5.2.2 Initial Conditions and Experiment Design

The LES model is initialized with idealized profiles for midlatitude summertime conditions following the framework of Schlemmer et al. (2011). Because we study the effect of convective precipitation, we choose initial conditions that are moist and unstable

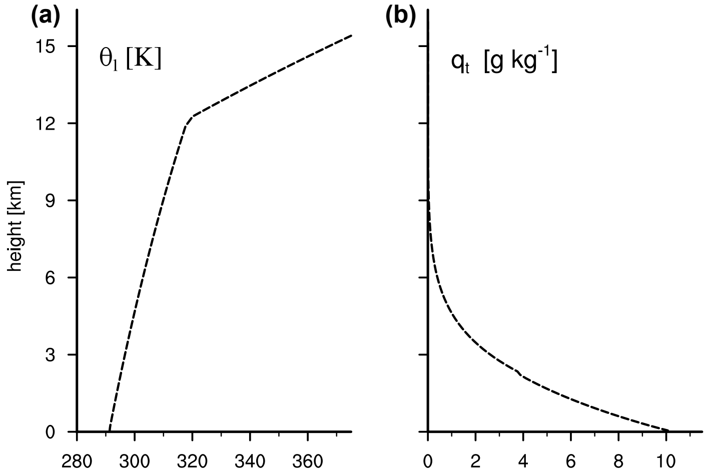

Figure 5.1: Initial atmospheric profile of (a) liquid water potential temperature and (b) specific humidity used in all experiments.

enough to produce convective precipitation (Fig. 5.1). The absolute temperature decreases uniformly with height at a rate of 8 K km^{-1} up to tropopause at 12 km and the specific humidity is chosen such that the relative humidity decreases from 80% in the boundary layer to 50 % at 5.5 km height and to 10 % above the tropopause. The transition from the boundary layer humidity to the free tropospheric humidity and to the humidity above the tropopause is obtained by combining two *tanh* functions as described in Schlemmer et al. (2011).

The infiltration of convective precipitation in the soil influences the surface energy balance through the modulation of the surface resistance to evaporation. The Penman-Monteith equation (Penman, 1948; Monteith, 1965) serves as an approximation for the natural evapotranspiration from a vegetated land surface:

$$F_{\text{lat}} = \frac{(Q_{\text{net}} - F_{\text{soil}})\ \frac{dq_{\text{sat}}}{dT}\ + \frac{\rho c_p}{r_a}(q_{\text{sat}}(T_{\text{atm}}) - q_{\text{atm}})}{\frac{dq_{\text{sat}}}{dT} + \frac{c_p}{L_v}(1 + \frac{r_{\text{surf}}}{r_a})} \tag{5.1}$$

where Q_{net} is the net incoming radiation, F_{soil} the soil heat flux, $\frac{dq_{\text{sat}}}{dT}$ the rate of change of saturation specific humidity with temperature, $q_{\text{sat}}(T_{\text{atm}}) - q_{\text{atm}}$ the humidity deficit, r_{a} the aerodynamic resistance and r_{surf} the surface resistance (the exact formulation for r_{surf} is given in Eq. 2.16).

Figure 5.2 illustrates the functional relationship between the latent heat flux and soil moisture content for two different leaf area indices (LAI). The parameters in Eq. 5.1 are fixed at constant values, typical for mid-latitude summertime conditions. Below the wilting point plants do not evaporate, whereas evaporation increases with soil moisture content until the field capacity is reached. The largest rate of change of evapotranspiration appears close to the wilting point, whereas the curve flattens out close to the field capacity. In a soil moisture limited regime, i.e. close to the wilting point, a slightly wetter surface depicts a considerably higher surface latent heat flux.

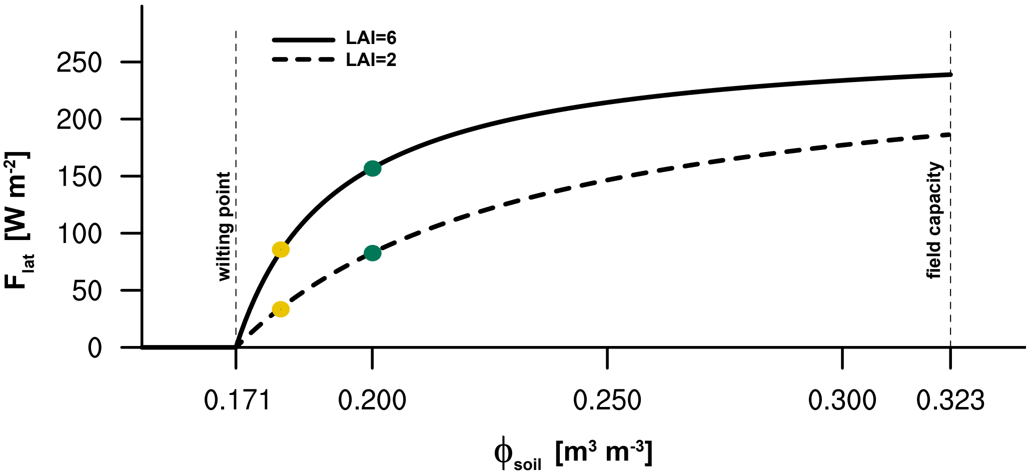

Figure 5.2: Functional relationship between surface latent heat flux (F_{lat}) and the soil moisture content (ϕ_{soil}) following Eq. 5.1. The two curves depict vegetation with large leaves (LAI=6, solid line) and small leaves (LAI=2, dashed line). The following parameters were fixed: Q_{net}=400 Wm^{-2}, F_{soil}=40 Wm^{-2}, $\frac{dq_{\mathrm{sat}}}{dT}$=7.9 g kg^{-1} K^{-1}, ρ=1.2 kg m^{-3}, c$_{\mathrm{p}}$=1004 J kg^{-1} K^{-1}, r_a=60 s m^{-1}, q_{atm}=8 g kg^{-1}, q_{sat}=10 g kg^{-1},L_v=2.5 10^6 J kg^{-1}, p_{00}=1000 hPa, $r_{\mathrm{surf,min}}$=150 s m^{-1}, ϕ_{wp}=0.171 m^3 m^{-3}, ϕ_{fc}=0.323 m^3 m^{-3} and f$_1$, f$_3$ and f$_4$ in Eq. 2.16 are set to 1. The colored markers indicate the soil moisture content used to initialize the model. The green marker denotes the experiments INF-01, NOINF-01, INF-02 and NOINF-02, whereas the yellow marker denotes the dry experiments INF-03 and NOINF-03.

In contrast, the system is energy limited when the soil moisture is close to the field capacity and evaporation does not depend on soil moisture. The model is initialized in the soil moisture limited regime where the effect of surface precipitation on the latent heat flux is potentially large. A homogeneous volumetric soil moisture content is prescribed in the entire domain. Note that in our formulation of the land surface model a minimum value for the resistance to evaporation is used. In opposition to Fig. 5.2, this means that surface latent heat fluxes may be nonzero even if the soil moisture is well below the wilting point.

		INF-01	NOINF-01	INF-02	NOINF-02	INF-03	NOINF-03
ϕ	$[m^3m^{-3}]$	0.20	0.20	0.20	0.20	0.18	0.18
LAI_{min}	[-]	2.0	2.0	3.0	3.0	2.0	2.0
LAI_{max}	[-]	6.0	6.0	5.0	5.0	6.0	6.0
c_{veg}	[-]	0.9	0.9	0.9	0.9	0.9	0.9
c_{soil}	[-]	0.1	0.1	0.1	0.1	0.1	0.1

Table 5.1: Summary of the performed experiments with initial conditions for soil moisture (ϕ), minimum and maximum value of leaf area index (LAI), vegetated fraction (c_{veg}) and bare soil fraction (c_{soil}).

Table 5.1 summarizes the experiments. Three sets of experiments are performed; each set contains an experiment where surface precipitation infiltrates into the soil (INF) and a sensitivity experiment where surface precipitation does not infiltrate and is simply removed from the system (NOINF). The first set of experiments (INF-01, NOINF-01) employs a large heterogeneity amplitude (ΔLAI = 4) and an intermediate soil moisture content ($\phi = 0.20$ m^3 m^{-3}). The second set of experiments (INF-02, NOINF-02) employs the same soil moisture conditions but a weaker heterogeneity amplitude (ΔLAI = 2). The last set of experiments (INF-03, NOINF-03) employs a very dry soil that is close to the wilting point ($\phi = 0.18$ m^3 m^{-3}). The soil moisture content is constant with height, whereas the soil temperature decreases monotonically as described in Table 2.1. The surface is covered with 90 % vegetation and 10 % bare soil in all experiments. The surface runoff model is switched off to avoid water loss, while infiltration into deeper layers follows Richards equation (Eq. 2.25) with a rigid lid at the lowest model level. The surface heterogeneity is prescribed by varying the LAI in a checkerboard pattern. The patch size is chosen to be 32 km, which is an optimal length scale for strong interactions with convection and a relatively late convergence of mesoscale circulations (compare Chapter 3). While the heterogeneity amplitude differs between the experiments, all experiments depict an average LAI of 4.0 to ensure a comparable mean energy input into the atmosphere.

5.3 Equilibrium Characteristics of Convection over Inhomogeneous Land Surfaces

Figure 5.3 shows the composite diurnal cycle of convection over two weeks along with the inter-daily spread around the mean. Shallow convection develops after 9 LST and transitions to deep precipitating convection between 10 and 11 LST. The maximum cloud cover amounts to 0.15 at around 12 LST and gradually decreases to zero until 00 LST. Some midlevel nocturnal clouds are considered negligible because they are inactive and do not precipitate. The inter-daily spread of cloud cover is larger in the range between 9 and 11 LST because the onset of convection slightly differs from day to day. We omit the first day because convection is very strong in the entire domain due to the the chosen very moist profile in this study. Generally, the spread around the mean diurnal cycle is small despite the changes in the surface conditions with time. The size of clouds is typically distributed in a spectrum from small shallow clouds of a few hundreds of meters to tens of km (see also Chapter 3). Given the coarser resolution in the experiments in this chapter, the smallest clouds have a size of 1 km, while the largest clouds exhibit a size that is again about half of the surface patch size. The precipitation phase exhibits a similar behavior compared to the cloud fraction time series. Surface precipitation starts between 10 and 11 LST after the first appearance of deep convective clouds and gradually decreases to zero until 21 LST. The maximum precipitation rates lie between 0.4 and 0.6 mm h^{-1} from 12 to 14 LST.

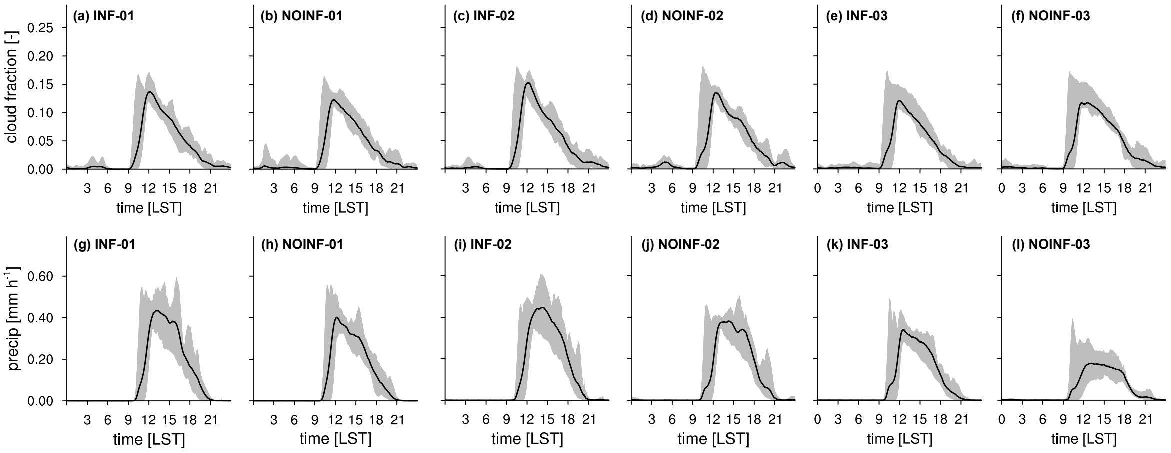

Figure 5.3: Composite diurnal cycle of (a-f) cloud fraction and (g-l) surface precipitation, both time series are averaged over two weeks of simulation time. Grey shading indicates the minimum and maximum values around the mean. The first day of the simulations is omitted because of the very moist initial conditions that force earlier convection than on subsequent days.

Overall, the INF and NOINF experiments exhibit similar cloud cover and precipitation characteristics. This is because the average surface energy constraints and the atmospheric background conditions are equivalent in all simulations. The simulations turn into a radiative convective equilibrium, in which convection is triggered in the morning, grows to deep convection and precipitates thereafter. Nevertheless, the NOINF experiment exhibits slightly lower precipitation rates compared to the INF experiment. This relates to the fact that in the NOINF experiments, the soil moisture decreases with time because the surface precipitation does not infiltrate into the soil. This is an artifact of our experiment design and is discussed in more detail in the next paragraph.

In the experiments without infiltration of precipitation (NOINF), by design, convection is not fully in equilibrium because the moisture reservoir is not balanced during precipitation events. This means that the soil slowly dries and surface evaporation decreases from day to day, which will eventually feed back on the atmospheric humidity and the diurnal cycle of convection. Fig. 5.4 shows a time series of the total soil moisture content in all experiments. The INF experiments can sustain a rather

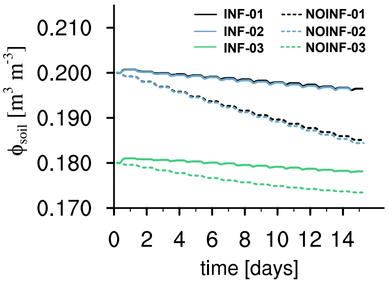

Figure 5.4: Time series of the soil moisture content for the different experiments.

constant soil moisture ($\phi_{day1} - \phi_{day14} = 0.003$ m^3 m^{-3}), while in the NOINF experiments the soil moisture considerably decreases ($\phi_{day1} - \phi_{day14} = 0.014$ m^3 m^{-3}). The decrease in the soil moisture in the NOINF experiments is the result of the moisture imbalance induced by the experiment setup. The decrease in soil moisture also explains the decrease in surface precipitation in the NOINF experiments (especially in NOINF-03). The insignificant decrease in soil moisture in the INF experiments stems from a slight redistribution of moisture from the soil into the upper troposphere through deep convective activity. Given the pronounced decrease in the surface precipitation rate in NOINF-03, in the following, we focus on the experiments with higher initial soil moisture (INF-01, NOINF-01, INF-02, NOINF-02).

5.4 From Heterogeneous Towards Homogeneous Land Surface Fluxes

Figure 5.5 illustrates the horizontal distribution of surface latent heat fluxes at the second and last day of INF-01 and INF-02. To compare the long-term effects of precipitation, all experiments are shown at 8:30 LST where the modulation of the surface energy balance by convective clouds is still negligible (cloud formation sets in after 9 LST, see Fig. 5.3). Note that we do not show the surface fluxes on the first day because convection is very strong during the spin up process even in the morning hours and masks the effect of the heterogeneous surface due to the chosen very moist profile. The background checkerboard pattern in surface latent heat flux is created by the imposed variations in LAI and is clearly visible in both experiments on the second day (Fig. 5.5a,c). At day 14, the patterns are still clearly visible in INF-01 but with a much smaller amplitude. After 14 days of convection in INF-02, the patterns are much less distinct than in INF-01 but still visible (Fig. 5.5d). The homogenization process is thus not completed in neither experiment.

In our simulations precipitation falls mostly over the patches with low initial evapotranspiration (Fig.5.6a). The ratio between precipitation over the warm and the cold patch remains above unity during the two weeks of simulation time in all experiments. The local coupling between evapotranspiration (i.e. soil moisture) and convection is thus negative in all our simulations. Experiments with large static heterogeneity amplitude (INF-01, NOINF-01) depict a stronger coupling than experiments with a small amplitude (INF-02, NOINF-02). The convective precipitation falls mostly over the patches with reduced evapotranspiration and creates a soil moisture pattern that is inverse to the pattern imposed by the static surface heterogeneity. The soil moisture content increases where the LAI is small and the soil moisture remains lower where the LAI is high (not shown). This suggests that the dynamic surface heterogeneities counteract the static patterns, although the resulting effects of precipitation remain limited.

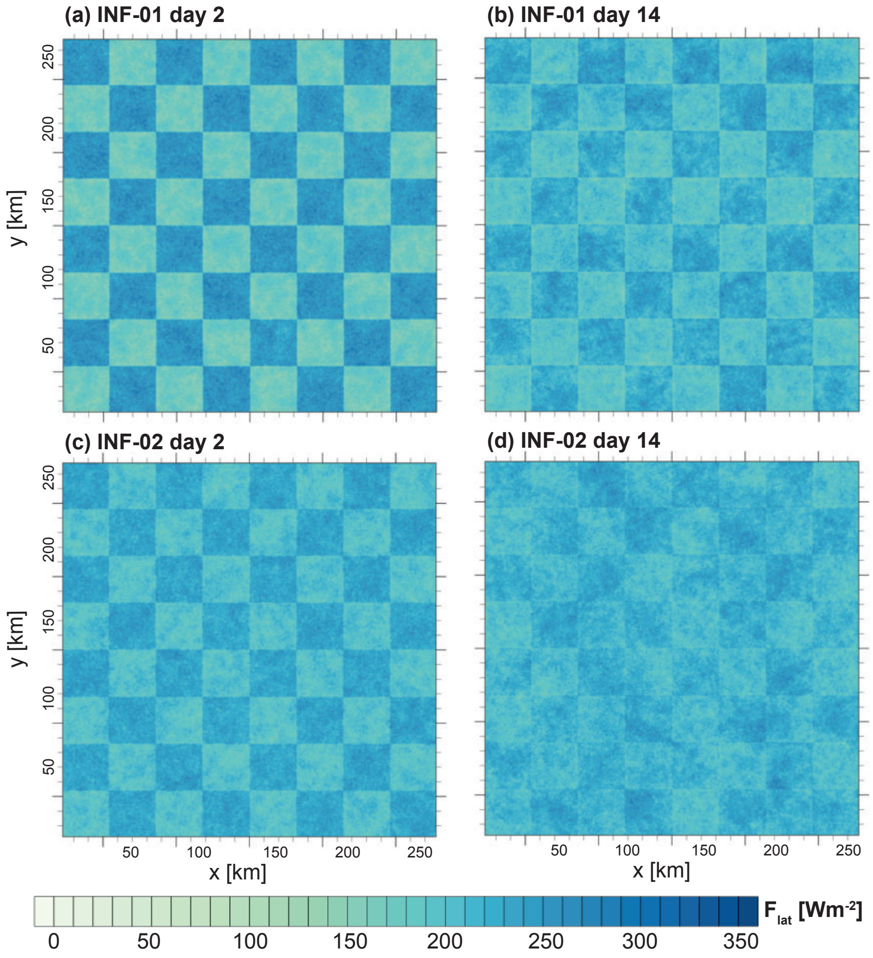

Figure 5.5: Horizontal distribution of surface latent heat fluxes at 8:30 LST for the dynamic experiments with strong heterogeneity amplitude (a,b) and with smaller amplitude (c,d). Left hand side figures show the conditions on the second day, whereas figures on the right hand side depict the situation at day 14.

The degree of homogenization can be quantified by the ratio of latent heat fluxes over different patches (Fig. 5.6b). The ratio decreases considerably in time and indicates a homogenization in all experiments. The ratio also decreases in the NOINF experiments even though the soil moisture cannot increase in response to precipitation. This is because the soil moisture does not decrease uniformly due to different LAI, which causes different evaporation rates over the different patches. This modulates the surface fluxes in a way that the latent heat flux ratio between the patches decreases slowly. The homogenization in the INF experiments is much faster, indicating that the homogenization through precipitation is more efficient. Comparing INF-01 and INF-02, the rate of homogenization is faster in INF-01, especially during the first days, because the precipitation ratio (Fig. 5.6a) is much higher in INF-01. After two weeks of simulation, the surface flux ratio in INF-01 has reached about the level that INF-02 initially had. A further reduction of the differences between the surface patches would require much longer timescales.

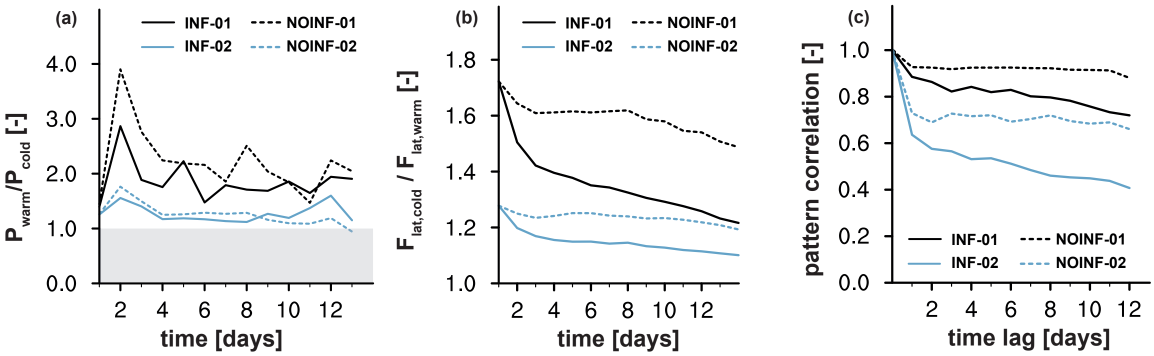

Figure 5.6: Time series of (a) daily surface precipitation ratio between the warm and the cold patch, (b) latent heat flux ratio between the warm and the cold patch and (c) spatial correlation between latent heat flux at the second and subsequent days. All data used to calculate the ratios in (b) and the correlation in (c) is averaged between 7-8 LST of the corresponding day, while the precipitation data in (a) is averaged over full days. The black lines represent the experiment INF-01 (solid) and NOINF-01 (dashed), whereas the blue lines represent the experiments INF-02 (solid) and NOINF-02 (dashed).

The surface latent heat fluxes are analyzed using pattern correlation. Figure 5.6c shows the Pearson coefficient of the time-lagged spatial correlation. The reference state is fixed to the second day of the simulation and the coefficient is computed for each subsequent day using data averaged between 7 and 8 LST. Because the imposed patterns remain visible in all experiments (see Fig. 5.5), the correlation is always positive. Note that the jump at the beginning of the time series is due to the autocorrelation at zero time lag. The NOINF experiments show a rather constant correlation, which confirms that the imposed patterns are not altered in these experiments. In the INF experiments, the correlation gradually decreases with time. The initial surface heterogeneity is thus successively removed by precipitation. Because the pattern correlation cannot detect new emerging structures, we analyze the variance budget in the next paragraph.

Spectral analysis is used to identify the dominant length scales in the surface latent heat flux data. The power spectral density (PSD) describes the spatial variability of the surface latent heat fluxes. Figure 5.7 presents the time evolution for the experiments employing a large heterogeneity amplitude (INF-01 and NOINF-01). The other experiments are not shown because they depict a similar behavior. A dominating maximum at wavenumber k=4, which corresponds to a wavelength of 64 km, emerges in the early morning hours of each day when the net radiation at the surface becomes positive. The dominating maximum is clearly related to the imposed static surface heterogeneity of 8 × 8 patches. Note that the checkerboard structure causes secondary maxima to appear at higher harmonics of the heterogeneity length scale because surface heterogeneity is imposed with step functions that are not continuous. The imposed length scale at k=4 is present at all time instances and in both experiments, especially in the morning hours. The homogenization process can thus not eliminate the imposed length scale at k=4, which is consistent with Fig. 5.6 and 5.5.

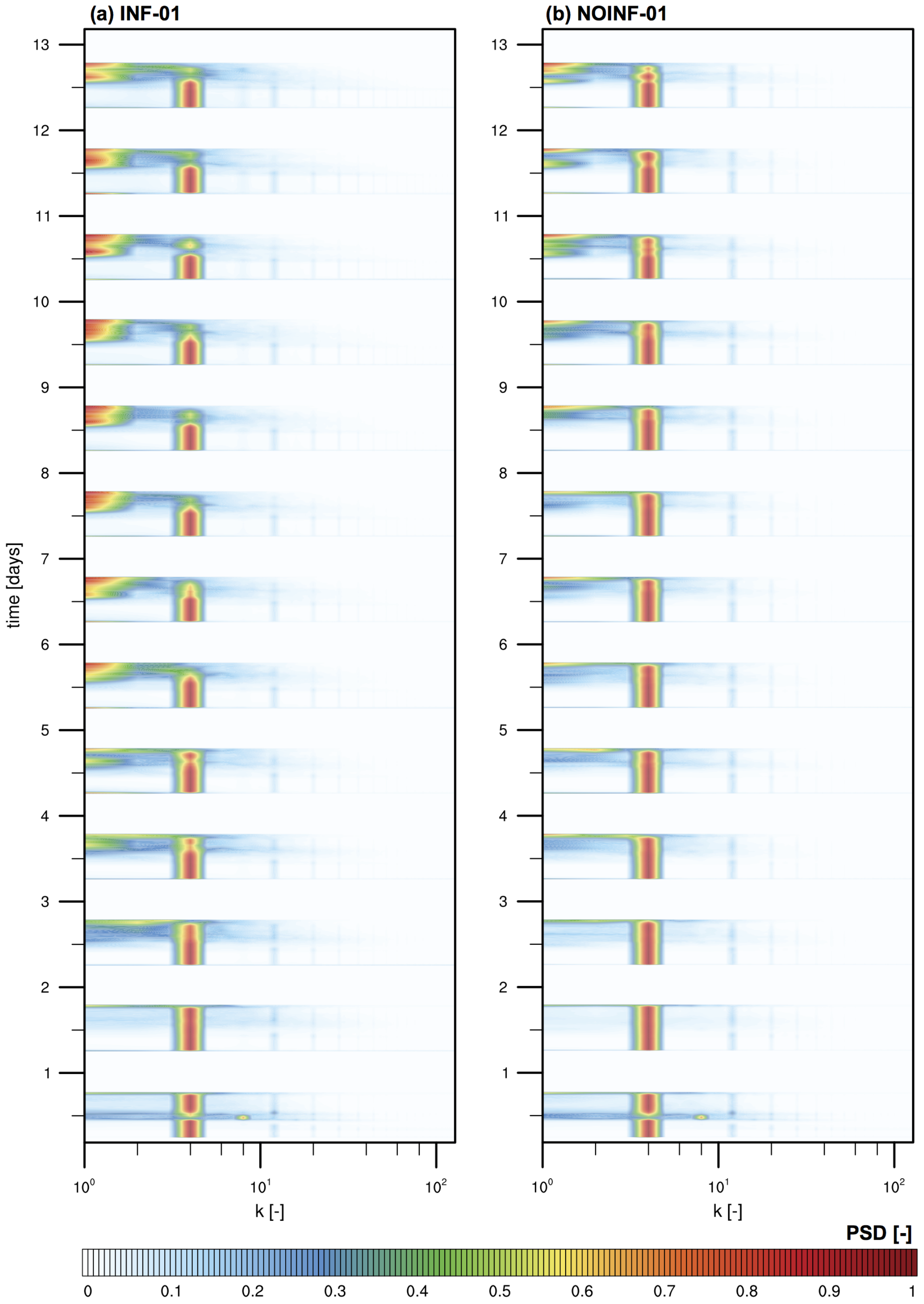

Figure 5.7: Time series of normalized power spectral density (PSD) of the surface latent heat flux anomalies around the domain mean for experiments INF-01 and NOINF-01. The spectra are calculated from data that is time averaged (4 min) and tapered at the boundaries. The spectra are calculated from one-dimensional data in both x and y directions. This is justified because we assume isotropic structures in the surface fluxes such as convection and turbulence. To a first approximation, the surface patches are also isotropic. For each time step the PSD is normalized with the L_2 norm, $||\mathrm{PSD}||_{L_2} = (\sum_{k=1}^{k_{\max}} \mathrm{PSD}(k)^2)^{\frac{1}{2}}$, to show its relative contribution to the total variability. Data points where the average surface latent heat flux drops below 1 W m^{-2} are masked.

This is however not true during the second half of each diurnal cycle. Figure 5.7 reveals that in the afternoon, new structures develop in INF-01 and NOINF-01. In INF-01, the importance of wavenumber k=4 for the total variance reduces strongly and other scales gain relevance in the spectrum. This is also true for NOINF-01 but to a smaller extent. The spectrum widens and a new maximum develops at k=1 on day five. The spectrum is more continuous compared to the morning hours, while the power density decreases with increasing wavenumber. This means that the variability is transferred from the heterogeneity scale mostly towards larger scales. The widening of the spectrum is related to a homogenization of the surface. The spectrum becomes wider because the related processes such as convective clouds and small-scale circulations are continuous. Towards the evening, the power density decreases again because the net incoming radiation decreases and convection ceases.

The new length scales are related to clouds and precipitation. To help understand Fig. 5.7, Fig 5.8 depicts a view on the cloud field in the morning and afternoon. During the first half of the day, mesoscale circulations are triggered and clouds organize following the imposed surface heterogeneity (see also Chapter 3). Thus, the imprint of convective clouds does not change the dominant length scales of the system. Because the precipitation patterns follow the cloud organization; we also find little influence by precipitation in the spectrum. The static heterogeneities dominate the wave spectra because they appear at a discrete wavenumber and because other continuous processes such as convection and precipitation are organized accordingly. New emerging structures are not identified during the first half of each diurnal cycle.

What is so different about the second half of the diurnal cycle? A fundamental difference is the fact that deep precipitating convection has developed and that propagating cold pools have a dominant control on the convective development (Fig. 5.8c,d). Cold pools exert strong perturbations on the boundary layer and propagate with pronounced velocities (see Chapter 4). The collision of several cold pools forces strong updrafts and may trigger new deep convective cells (e.g. Schlemmer and Hohenegger, 2014). At this stage, convection is not organized by the land surface anymore but aggregates following the cold pool forcing, which is not tied to the initial surface heterogeneity (compare Fig. 5.8). Cold pools advect cold and dry air over warmer surfaces and modify the surface fluxes. This modification by cold pools is induced by thermodynamic and wind effects; in contrast to the more indirect modification through the surface resistance by soil moisture. This means that the atmospheric control on the surface fluxes dominates, while the surface control on the fluxes becomes of secondary order at this time. The result is an effective homogenization of the surface fluxes by cold pools in the afternoon of each diurnal cycle, especially in the INF experiments with weaker surface heterogeneity.

The characteristics of the surface flux spectra of INF-01 and NOINF-01 (Fig. 5.7) are similar because cold pool formation is present in both experiments on each day. Despite these common features, the two experiments also depict some differences among each

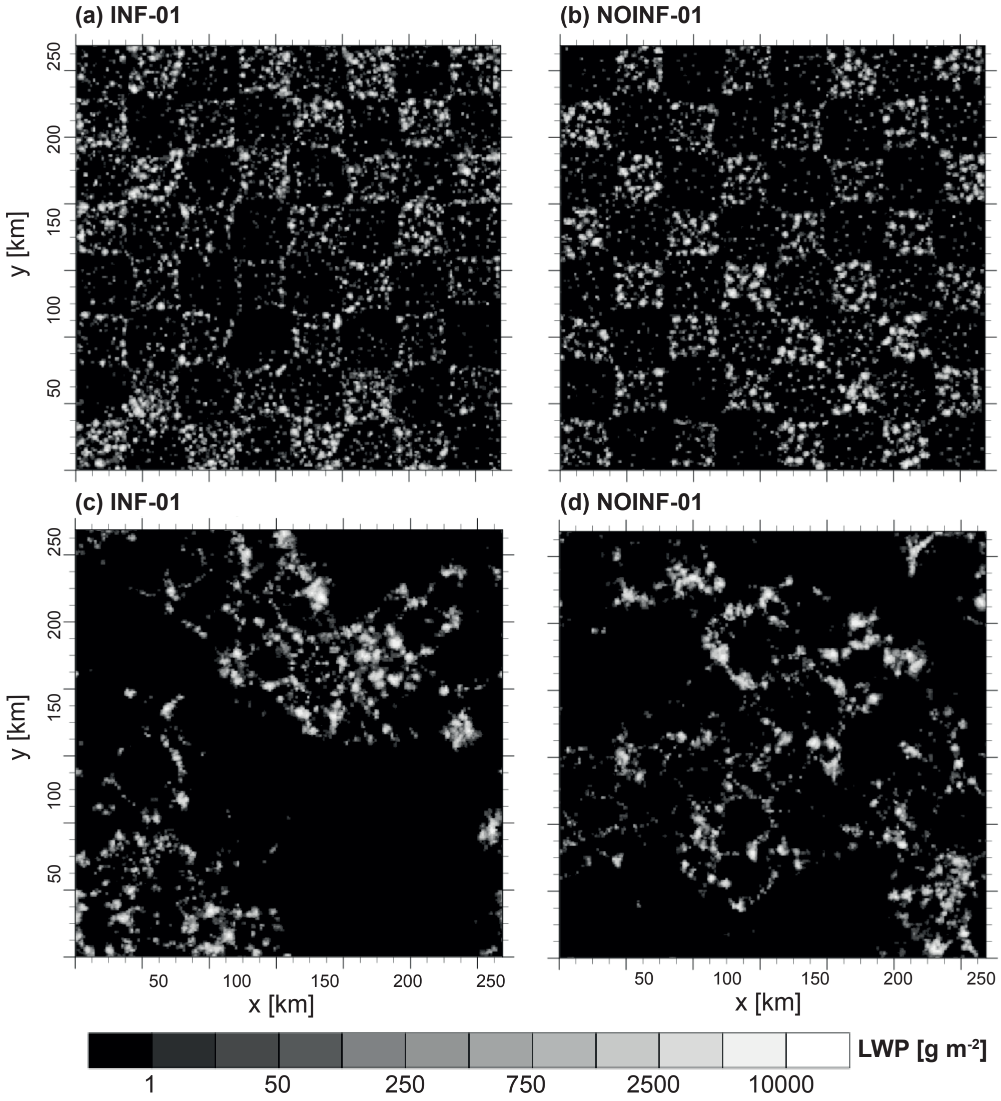

Figure 5.8: Instantaneous view on the cloud field in terms of liquid water path for INF-01 and NOINF-01. Two different time instances during the fourth day are shown: (a,b) at 10 LST and (c,d) at 14 LST.

other. The imposed surface heterogeneity scale is more dominant in NOINF-01 because the heterogeneous surface forcing is stronger. For example, on day six the maximum at k=4 disappears in INF-01 during the afternoon, while it is still present in NOINF-01. Generally, the spectra in INF-01 show more variability because the maximum is less dominant in the afternoon. The same mechanisms hold for the experiments INF-02 and NOINF-02 (not shown). In these experiments, cold pools are even more dominant because the heterogeneity amplitude is smaller and the surface forcing is weaker.

The spectral analysis highlights the importance of cold pool formation for the modification of land surface fluxes. While cold pools modify the surface flux spectrum on each consecutive day, the homogenization process by soil moisture precipitation coupling does not add new dominant length scales.

5.5 Summary and Discussion

In this chapter, we analyze the modulation of static surface heterogeneities by precipitating convection. Two weeks of convective diurnal cycles are simulated by means of large-eddy simulations. Three sets of experiments with different soil moisture content and different heterogeneity amplitude are performed. Each set contains one simulation where surface precipitation feeds back on the soil moisture content (INF) and one experiment where soil moisture can only change due to evaporation (NOINF). The composite diurnal cycle of convection is surprisingly robust to changes in the surface properties and develops a stationary state in all experiments.

As expected, the imposed surface heterogeneity triggers mesoscale circulations that force the development of convection over patches with less evaporation. This means that the coupling between evapotranspiration and surface precipitation is negative in all simulations during two weeks of simulation time. After several diurnal cycles, the soil moisture depicts a pattern that is inverse to the one initially imposed by the LAI distribution. The soil moisture increases over the dry patch due to infiltration of precipitation. This effect overcompensates the decrease in soil moisture due to higher evapotranspiration over the wet patch. As a consequence, the ratio between the surface latent heat fluxes of warmer and colder patch decreases. This homogenizes the surface fluxes within the domain. The rate of homogenization decreases with the heterogeneity amplitude. Two weeks of diurnal precipitation are not sufficient to completely homogenize the surface pattern in our simulations. A further homogenization is expected to require longer timescales because the forcing decreases with time. While this homogenization effect is slow, another effect is found to be important to introduce new length scales and to change the convective organization.

The analysis of surface length scales reveals two distinct phases within the diurnal cycle of the surface fluxes. The first phase is the initialization of convection including the transition to deep convection. During this stage, the imposed surface length scale dominates the spectrum, because convection is organized by the imposed surface pattern. The only effect during this stage is a slow homogenization. The second stage is characterized by cold pool propagation and convective aggregation. During this stage the surface heterogeneity is temporarily weakened because the atmospheric control on the surface fluxes by cold pools is much stronger than the surface control on the fluxes by land surface heterogeneities. On some days, cold pools are strong enough to temporarily remove the dominant surface scale. This is especially true in the experiments with dynamic soil moisture precipitation coupling because the surface heterogeneity has become weaker. As a result, the surface flux spectra become more continuous and the variability increases towards both smaller and larger scales. Nevertheless, the imposed surface heterogeneities cannot be completely eliminated, neither by soil-moisture precipitation coupling nor by intense cold pools.

The purpose of this chapter was to identify the modification of initially imposed static surface heterogeneities by precipitating convection. To determine the potential of this effect, we employ a setup that is sensitive to modifications given a static background heterogeneity. First, the atmospheric background conditions were tuned to produce a considerable amount of convective precipitation. Second, the surface patch size was chosen such that precipitating convection is maximized over the dry patch. Higher precipitation amounts would accelerate the homogenization process as long as precipitation is still convective and constraint to the surface heterogeneity. The simulations were performed under relatively dry soil conditions to induce large changes in the surface energy balance by infiltration of precipitation. Finally, the background wind was switched off to avoid advection of precipitation over patches with high evapotranspiration, which could otherwise amplify the imposed surface heterogeneity. Because we optimize the setup for a potentially strong effect, a different setup will likely cause a weaker effect.

In this study, we tested the effect of dynamic heterogeneities in the parameter space that is potentially sensitive to changes in the soil moisture. Dry surface conditions are combined with moist atmospheric conditions resulting in a high potential for precipitating convection. Under these conditions, static surface heterogeneities cannot be completely eliminated within two weeks. Given such long timescales and the constraints for soil moisture, background wind and weak synoptic forcing, it becomes clear that a full homogenization by convective precipitation is unlikely to happen under realistic conditions. Typical midlatitude weather conditions also involve strong synoptic scale forcing with frontal and stratiform precipitation that would inhibit small-scale feedbacks. Occasionally, long periods of diurnally forced precipitating convection exist in midlatitudes (Hohenegger et al., 2009) and especially in tropical semi-arid regions (Taylor et al., 1997). Under such conditions, the heterogeneity of the surface fluxes is expected to decrease in amplitude but cannot be eliminated completely. This suggests that the influences of static surface heterogeneities on convective development remain significant even on longer timescales.

Chapter 6

Summary and Conclusions

In this dissertation, we have addressed research questions related to the interaction between inhomogeneous land surfaces and moist convection. In the following, we summarize the major results for each question and conclude its impact on the research area. A general conclusion is given at the end. In the outlook, we discuss the implications of our work for future parameterization development and observational studies, and propose a study on land-atmosphere interactions in a warmer climate.

A new land surface model has been implemented into the University of California Los Angeles - Large-Eddy Simulation (UCLA-LES) model. The modeling setup allows for complex interactions between the land surface, clouds, and radiation at high resolution. The high resolution is crucial to resolve the spectrum of convective clouds and related circulations in order to understand interactions between the land and the atmosphere. The correctness of the implementation into UCLA-LES was confirmed by a comparison with the Dutch Atmospheric Large-Eddy Simulation model for a case of a dry convective boundary layer with an interactive land surface. The presented modeling framework allows us to accomplish our research objectives specified by the following questions.

What Determines the Cloud Size Distribution over Land?

Idealized large-eddy simulations have been used to understand the effect of various surface patch sizes on the size distribution of convective clouds. As seen over homogeneous surfaces, the cloud size distribution can be approximated by a power law with a scale break at larger scales. While the scale break varies with surface patch size, the exponent of the power law is independent of it. Because the majority of the clouds are small, cloud cover remains invariant for different surface conditions. The scale break and thus the size of the largest clouds varies with patch size and depends on the timing of converging mesoscale circulations. Over heterogeneous surfaces, the local maximum of the size a cloud can reach is limited to half the patch size. Given these results, the following conclusion can be drawn:

- We dismiss the idea that larger clouds always grow faster because they feel a lower entrainment as found over homogeneous surfaces. Instead, the timing and strength of the convergence induced by mesoscale circulations influences the growth rate of convective clouds. This means that cloud development is more complex over heterogeneous land surfaces and relationships obtained from homogeneous conditions may be too simplified.

Does the Transition Time from Shallow to Deep Convection Depend on the Size of Land-Surface Heterogeneity?

The distinct effect of the surface patch size on the cloud size distribution suggests that the transition time from shallow to deep convection is modified by surface heterogeneity. This hypothesis has been confirmed, however, it was not possible to determine a simple relationship between patch size and transition time. The time it takes to transition depends on the timing between the growth rate of clouds due to the destabilization of the atmosphere and the timing of the mesoscale convergence triggered by the surface heterogeneity. The total accumulated precipitation tends to increase with patch size, while the transition time is minimized for intermediate surface patch sizes between 12 and 25 km. This intermediate patch size causes a transition time of two thirds that over a homogeneous surface, which is a significant modification of the diurnal cycle of convection.

- In order to better capture the transition from shallow to deep convection over land, the effect of sub-grid surface conditions can be included into coarser resolution weather and climate models. We suggest to incorporate a proxy for the simulated effect of surface heterogeneity on the cloud size and transition time, which should depend of the dominant length scale on the underlying surface. Different approaches are conceivable, e.g. in the entrainment formulation or triggering function of a convective parameterization as well as a modification of the cloud size distribution in advanced spectral mass flux schemes. Detailed suggestions are given in the outlook of this thesis.

The results of the previous questions emphasize the control of mesoscale circulations on the cloud size and on the transition process. However, convection can also strongly modulate the circulation characteristics, as addressed in the next question.

What are the Impacts of Precipitating Convection on the Characteristics of Surface Induced Circulations?

The formation of clouds and precipitation significantly affects the propagation of surface induced mesoscale circulations. Three conceptual stages are identified. First, a dry convective circulation with a slowly propagating breeze front. Second, the occurrence of deep convection intensifies the circulation due to strong updrafts and significantly accelerates the front propagation. Finally, a precipitating stage where strong cold pools develop at the breeze front and induce further acceleration of the propagation speed. The acceleration induced in both stages, the cloud dynamical stage and the precipitation thermodynamical stage, is of the same order of magnitude as the absolute value of the dry circulation and thus relevant to predict a correct propagation. Classical theory of density currents implicitly includes the third stage, which represents the cooling from precipitation evaporation. In contrast, classical theory fails to represent the second stage. The theory is extended using the cloud base mass flux, which accounts for the observed effects of moist nonprecipitating convection on the propagation speed. We demonstrate the applicability of this theory to results from large-eddy simulation.

- The propagation of a mesoscale circulation depends critically on the stage of convective development. Because convective parameterizations are imperfect, numerical weather prediction models with parameterized convection are likely to predict an incorrect strength and timing of the propagating systems. This may lead to significant biases in local weather predictions. Global climate models with grid sizes $\mathcal{O}(100\ km)$ are incapable to resolve mesoscale circulations and propagation of convective systems because grid cells are too large. This may cause significant precipitation biases over land, especially in coastal areas where the propagation of convective systems is not represented (e.g. Florida peninsula).

- The modification of the propagation of mesoscale circulations is especially important in the context of large scale heterogeneities with a delayed mesoscale convergence, because the modification by convection requires time to develop. Such optimal conditions include large scale vegetation and especially continental land-sea breeze systems. In this context, moist convection has a positive effect on the local climate in costal regions due to a faster inland propagation of clean maritime air.

- Finally, our results suggest that mesoscale circulations are potentially stronger in moist convective environments than in dry situations. The positive superposition of the dry circulation with the deep convective stage and the precipitation stage causes an enhancement of mesoscale circulations and may thus trigger larger and deeper clouds.

The previous chapters revealed an influence of static surface heterogeneities on moist convection and its feedback on the circulation. The effect of infiltration of precipitation in the soil is addressed in the next question.

Can Precipitating Convection Homogenize the Surface Fluxes over Heterogeneous Land Surfaces?

Running large-eddy simulations of diurnal convection for two weeks shows that precipitation prevails over the dry surface patches and changes the surface fluxes. Sensitivity experiments reveal that infiltration of organized precipitation in the soil helps to homogenize the surface fluxes, but cannot eliminate the imposed static surface heterogeneity during two weeks of simulation time. However, cold pools introduce strong perturbations in the boundary layer temperature and humidity distribution subsequent to precipitation events. Cold pools have strong control on the surface and act to homogenize the surface fluxes within the entire domain, but only during cold pool lifetime. Two distinct stages in the evolution of the surface fluxes are identified. First, during nonprecipitating convection, the imposed static surface heterogeneity dominates the surface flux spectrum. Second, during precipitation and subsequent cold pool formation, the spectrum becomes wider and the surface fluxes become more homogeneous. During two weeks of simulation time, the homogenization effect of cold pools becomes stronger with time, while the static surface heterogeneity is successively weakened but not eliminated by infiltration of precipitation.

- Infiltration of precipitation into the soil cannot fully eliminate surface heterogeneities on timescales of two weeks. This means that the influence of static heterogeneities on convective development remains significant even under persistent conditions of precipitating diurnal convection.
- The effect of a homogenization of the surface fluxes by precipitation infiltration is weak even though the experiments are performed under optimal conditions for such an effect. These conditions include a moist and unstable atmospheric state where deep convection may easily be triggered, a weak synoptic forcing where local circulations exert the dominant control on convection, and a dry soil where evaporation is sensitive to the infiltration of precipitation. A stronger effect is unlikely to happen under different background conditions.
- While the long-term homogenization of the surface by infiltration of precipitation in the soil is slow, the short term homogenization by cold pools is surprisingly effective. This suggests that during the precipitating regime, the triggering and organization of convection is mostly determined by cold pool dynamics, while during the nonprecipitating regime, the triggering and organization is induced by surface heterogeneity.

General Concluding Remarks

The goal of this dissertation was to improve the understanding of the interactions between surface heterogeneities, deep moist convection and related circulations, and to derive relationships among them. Three main cycles have been addressed (Fig. 1.2): A) The influence of the land surface on convective clouds and their feedback on the surface. B) The effect of clouds and precipitation on the atmospheric circulation, and C) the effect of precipitation on the land surface. The following conclusions are drawn from the combination of these three effects:

- Static and dynamic surface heterogeneities directly control the surface fluxes during the development of convection. The heterogeneity of the surface fluxes determines the convective organization and transition to deep convection as well as the precipitation characteristics. The effects are likely to be important during midlatitude summertime conditions and in semi-arid and tropical regions where diurnally forced convection is dominant. The dynamic surface heterogeneities induced by cloud shading effects and soil moisture variability have only limited effect on convection. On short timescales, the shading effect was independent of patch size but important for the strength of mesoscale circulations. On longer timescales, the homogenization of the surface by infiltration of precipitation in the soil was slow. Despite their rather weak effects on daily and weekly timescales, dynamic land-surface heterogeneities counteract the influence of static surface heterogeneities. This suggests that anthropogenic land cover changes are antagonized by nature through land-atmosphere interactions. Locally, warm and dry surface patches receive the majority of surface precipitation, which results in a cooling of warmer surfaces and a moistening of drier soils.

- The atmospheric control on the surface fluxes is remarkably strong during the precipitating stage of convection. During this time, cold pools are identified to be the dominant source for convective development, while surface heterogeneities become of secondary importance. The effect of cold pools has recently been introduced into a convective parameterization (Grandpeix and Lafore, 2010). The triggering of convection in parameterization may be separated into a precipitating and a nonprecipitating regime, where land surface heterogeneities mostly influence the nonprecipitating regime.

- Our results have been obtained from large-eddy simulation with idealized large-scale conditions typical for midlatitude summertime (Schlemmer et al., 2011). The use of domain and time averaged quantities as well as the obtained systematic behavior of the convective response across the different experiments give confidence that the results and mechanisms discussed in this dissertation are characteristic for the general behavior of summertime convection in response to heterogeneous surface forcing. We expect the results to hold for similar regimes (e.g. convection in semi-arid or tropical climates) as long as clouds are predominantly triggered due to a buoyancy advantage (i.e. over warmer surface patches). Optimal conditions for the simulated effects are weak large-scale forcing where convection develops locally.

- The use of an interactive land-surface model and a high-resolution convection resolving atmospheric model is crucial to represent land-atmosphere interactions. Simulations without an interactive land surface may overestimate mesoscale circulations because convective clouds organize and reduce the available energy in areas with a buoyancy advantage. In addition, the effect of dynamic heterogeneity and cold pools on the surface fluxes may only be represented with an interactive land surface. An interactive land surface model coupled to a high-resolution atmospheric model is thus required to correctly model moist convection and circulations over inhomogeneous land surfaces.

Chapter 7

Outlook

The focus of this dissertation was to understand and quantify the interactions between heterogeneous land surfaces and deep moist convection. The way we pursue our ideas follows a process-based approach, where a fundamental understanding is preferred over ensemble analysis. Jakob (2010) argues that for parameterization development this approach is essential because it helps incorporating the increased knowledge into models in a more realistic way. Despite this process understanding, the application of the obtained results must not be neglected. Thus, the next step following our research is to use our ideas in larger scale weather and climate models where the described effects may be parameterized. The results from this dissertation already motivated a follow-up study on the representation of an idealized land-sea breeze circulation across models with different resolution and different treatments of convection (Hohenegger et al., 2014).

Current numerical weather prediction (NWP) models operating with a horizontal grid size less than 10 km explicitly resolve part of the convective spectrum and often omit parameterizations for deep convection. Following Skamarock (2004), the effective resolution of these models is about seven times the grid size. This suggests that the effective resolution under which circulations and convection are correctly represented is significantly larger than 10 km in most NWP models. Our experiments revealed that convective development and precipitation generation depend on surface patch sizes well below 10 km. It is therefore unlikely that the effects of surface heterogeneity are properly represented in high-resolution NWP models within the so called ”grey-zone”. Ideas to incorporate surface heterogeneity effects into NWP and climate models with parameterized convection are discussed in the next paragraph.

7.1 Ideas for Parameterization Development

The individual conclusions already highlighted areas of parameterization improvement. The pathway from the process level at small scales towards an application in larger scale weather and climate models is a challenge. Such parameterizations use simple relationships between grid scale variables and the anticipated cloud development. Land surface characteristics and some of their effects on cloud development can be included into parameterizations to gain a more physical representation of convection over land. While a fully comprehensive representation of heterogeneity effects on convection may be beyond the scope of most parameterizations, some of the principal mechanisms we identified may be included into convective parameterizations. Here we present some preliminary ideas for future parameterization development:

- A starting point to parameterize heterogeneity effects in large scale models may be the entrainment formulation. Simulations with a lower entrainment rate exhibit larger clouds and a faster transition to deep convection (de Rooy et al., 2013). As a first approximation, we suggest to vary the bulk entrainment rate depending on the underlying dominant surface length scale. A power spectrum of surface properties, such as used in Chapter 5, may be used to determine the dominant length scale for each grid box. This can be achieved using satellite surface data that are available at high resolution. The lowest entrainment rates should be specified in regions with intermediate surface length scales between 12 and 25 km. Scales smaller than the boundary layer height and scales larger than the Rossby radius of deformation should exhibit similar entrainment rates as found over homogeneous surfaces because the effects of surface heterogeneity become negligible. This simple modification can be tested in climate models and especially in NWP models with parameterized convection. In NWP models the horizontal grid size is still too large to correctly represent surface induced circulations and their effect on convective clouds. The assumption of the entrainment approach is that regions with an optimal heterogeneity scale exhibit a faster transition to deep convection. This may improve the timing of the diurnal cycle of convection which is a problem in many NWP models (Petch et al., 2002). Our suggestion may be combined with the recently proposed modification of the convective closure in large-scale models by Bechtold et al. (2014).

- Another starting point to represent surface heterogeneities may be in spectral convection schemes with an explicit representation of cloud sizes, following ideas of Arakawa and Schubert (1974). The scheme developed by Plant and Craig (2008) may be seen as development in this direction. The convective ensemble is specified by probability density functions (PDF) of the cloud base mass flux. In such a scheme, the PDF is used to determine the cloud ensemble within a grid box. Our results suggest that, over heterogeneous land surfaces, the tail of the PDF should be modified to account for larger clouds, while the bulk of the PDF should remain unchanged. This may help to get a more physical representation, especially in coarser resolution weather and climate models over land.

- All convection schemes use triggering functions to determine whether moist convection is initiated (e.g. Arakawa and Schubert, 1974). While many triggering functions depend on a single bulk plume, advanced schemes may also incorporate a spectral representation of entraining plumes. Using the spectral approach, the ensemble of plumes can be modified depending on land surface characteristics. Areas with optimal surface conditions should obtain a higher triggering potential through e.g. a larger temperature perturbation of the ascending parcel. The details of the approach depend on the individual model physics.

- As seen in Chapters 4 and 5, convective triggering and organization is controlled by cold pool dynamics during periods of intense precipitation. During these periods, the influence of the land surface on convection becomes negligible. Therefore, the modifications suggested above should be important during periods without precipitation. The effect of cold pools may be incorporated by a separate density current parameterization (e.g. Grandpeix and Lafore, 2010). In this context, we also propose a modified formula for density current propagation as described in Chapter 5.

- Despite the suggestions for parameterization development over heterogeneous land surfaces, there is also evidence that surface heterogeneity may not be important under certain conditions. For example, cloud cover was, to a first approximation, invariant to the surface heterogeneity in all our simulations. This suggests that one may neglect detailed information on sub-grid surface heterogeneity if only interested in large-scale cloud cover. Under conditions of strong synoptic forcing, the influence of surface heterogeneity on convection is expected to become weak. While the exact effect of background wind on land-atmosphere interactions is still controversial (Avissar and Schmidt, 1998; Raasch and Harbusch, 2001; Lynn and Tao, 2001), it becomes increasingly apparent that under conditions of strong background wind, the effect of surface heterogeneity on the atmospheric circulation and thus also on the cloud size development weakens.

7.2 The Use of Observations

In this dissertation, we used a large-eddy simulation modeling framework where the boundary layer, circulations and especially moist convection are explicitly resolved. Even models with such a high resolution have deficiencies, i.e. microphysical processes and small-scale turbulence have to be parameterized and induce uncertainty. Therefore, our results can be compared to observations.

The relations required for parameterization development are hard to infer from observations because of low spatiotemporal resolution and the inability to measure required quantities. This is especially true for three-dimensional data sets of wind, temperature and humidity in large domains. Despite these limitations, several measurement campaigns have been set up to better understand land-atmosphere interactions (e.g. ARM-SGP, FIFE, HAPEX-Sahel, LBA and SMACEX). The findings are important for our understanding, but also in order to validate results obtained from model studies. Currently, new techniques are developed to infer three-dimensional wind fields from ground based precipitation radar networks following the work of Protat and Zawadzki (1999). While this data will only be available during precipitation events, it is a promising perspective and may be used to validate some of the findings from our process studies. The data may be applied to our findings in Chapter 4, where the cloud and cold pool circulation play a central role for the propagation of mesoscale breeze systems.

The effect of surface heterogeneity on the cloud size distribution could also be derived from satellite data to reconfirm our findings from Chapter 3. High resolution data sets of cloud liquid water path are available from geostationary meteorological satellites, e.g. the Meteosat Second Generation (MSG) (Schmetz et al., 2002). Previous studies over the Florida peninsula used data from Landsat Thermatic Maper (Landsat-TM) to quantify the effect of land cover change on precipitation (Marshall and Pielke, 2004). The cloud liquid water path from MSG may be combined with data on land surface characteristics obtained from the Landsat-TM satellite to reconfirm the link between large clouds and surface patch size.

With the ever-increasing resolution in atmospheric models, one must not forget to also increase the resolution of surface data sets to take advantage of the ability to directly resolve land-atmosphere interaction as accurately as possible. In addition, many of the ideas to incorporate our findings into parameterizations rely on high-resolution surface data to quantify the actual sub-grid heterogeneity of the land-surface. Spatially comprehensive high-resolution surface datasets exist, but are often not available in current NWP and climate models. In particular, the seasonal variability of vegetation, surface albedo but also soil moisture is often not represented. With modern satellite data being readily available, this is a topic for future research.

7.3 Land-Atmosphere Interactions in a Warmer Climate

In this dissertation, the interactions between land surface heterogeneity and moist convection have been tested for a climatological mean state. Generally, it is uncertain how land surface interactions change in a warmer climate, although they are thought to increase future climate variability (Seneviratne et al., 2006). It is of interest whether the mechanism we identified in this dissertation act under very different climatic conditions. Although the cloud size evolution is expected to act similar, this can easily be tested by repeating part of the analysis from Chapter 3. In addition, Rieck et al. (2012) found a surface flux feedback on convection over a homogeneous ocean surface. The study revealed stronger surface moisture fluxes in a warmer climate that help to increase tropospheric mixing and finally decrease cloud cover. We propose a similar study over land using the modeling framework established in this dissertation. While we can only speculate here, the surface moisture fluxes in a warmer climate should also increase over land. In contrast to the experiments from Rieck et al. (2012), this may strongly decrease the sensible heat fluxes because the surface energy is limited. To which extend this will cause a drying of the land surface and a reduction of cloud cover is unknown. Fundamental differences between land and ocean are the variable surface temperature and the limited soil moisture over land, while in Rieck et al. (2012) the ocean surface had a constant temperature and an infinite water reservoir. The proposed study may help to better understand the response of convection to a tropospheric warming over land.

References

Antonelli, M. and Rotunno, R. (2007). Large-Eddy Simulation of the Onset of the Sea Breeze. *Journal of the Atmospheric Sciences*, 64(12):4445–4457.

Arakawa, A. and Schubert, W. (1974). Interaction of a cumulus cloud ensemble with the large-scale environment, Part I. *Journal of the Atmospheric Sciences*, 31:674–701.

Avissar, R. and Pielke, R. (1989). A parameterization of heterogeneous land surfaces for atmospheric numerical models and its impact on regional meteorology. *Monthly Weather Review*, 117:2113–2136.

Avissar, R. and Schmidt, T. (1998). An Evaluation of the Scale at which Ground-Surface Heat Flux Patchiness Affects the Convective Boundary Layer Using Large-Eddy Simulations. *Journal of the Atmospheric Sciences*, 55:2666–2689.

Baldauf, M., Seifert, A., Förstner, J., Majewski, D., Raschendorfer, M., and Reinhardt, T. (2011). Operational Convective-Scale Numerical Weather Prediction with the COSMO Model: Description and Sensitivities. *Monthly Weather Review*, 139(12):3887–3905.

Bao, X. and Fuqing, Z. (2013). Impacts of the mountainplains solenoid and cold pool dynamics on the diurnal variation of warm-season precipitation over northern China. *Atmospheric Chemistry and Physics*, 13(14):6965–6982.

Bathiany, S., Claussen, M., Brovkin, V., Raddatz, T., and Gayler, V. (2010). Combined biogeophysical and biogeochemical effects of large-scale forest cover changes in the MPI earth system model. *Biogeosciences*, 7(5):1383–1399.

Beare, R. J. (2013). A Length Scale Defining Partially-Resolved Boundary-Layer Turbulence Simulations. *Boundary-Layer Meteorology*, 151(1):39–55.

Bechtold, P., Chaboureau, J.-P., Beljaars, a., a.K. Betts, Köhler, M., Miller, M., and Redelsperger, J.-L. (2004). The simulation of the diurnal cycle of convective precipitation over land in a global model. *Quarterly Journal of the Royal Meteorological Society*, 130(604):3119–3137.

Bechtold, P., Semane, N., Lopez, P., Chaboureau, J.-P., Beljaars, A., and Bormann, N. (2014). Representing Equilibrium and Nonequilibrium Convection in Large-Scale Models. *Journal of the Atmospheric Sciences*, 71(2):734–753.

Beljaars, A. and Holtslag, A. A. M. (1991). Flux Parameterization over Land Surfaces for Atmospheric Models. *Journal of Applied Meteorology*, 30:327–341.

Benjamin, T. B. (1968). Gravity currents and related phenomena. *Journal of Fluid Mechanics*, 31(2):209–248.

Berg, L. C. J. and Oerlemans, J. (1985). Simulation of the sea-breeze front with a model of moist convection. *Tellus*, 37A(1):30–40.

Betts, A. K. (1975). Parametric Interpretation of Trade-Wind Cumulus Budget Studies. *Journal of the Atmospheric Sciences*, 32:1934–1945.

Blanchard, D. O. and López, R. E. (1985). Spatial patterns of convection in south Florida. *Monthly weather review*, 113:1282–1299.

Blossey, P. N., Bretherton, C. S., Zhang, M., Cheng, A., Endo, S., Heus, T., Liu, Y., Lock, A. P., de Roode, S. R., and Xu, K.-M. (2013). Marine low cloud sensitivity to an idealized climate change: The CGILS LES intercomparison. *Journal of Advances in Modeling Earth Systems*, 5(2):234–258.

Böing, S. J., Jonker, H. J. J., Siebesma, a. P., and Grabowski, W. W. (2012). Influence of the Subcloud Layer on the Development of a Deep Convective Ensemble. *Journal of the Atmospheric Sciences*, 69(9):2682–2698.

Bony, S. and Dufresne, J.-L. (2005). Marine boundary layer clouds at the heart of tropical cloud feedback uncertainties in climate models. *Geophysical Research Letters*, 32(20):L20806.

Chen, F. and Avissar, R. (1994). Impact of Land-Surface Moisture Variability on Local Shallow Convective Cumulus and Precipitation in Large-Scale Models. *Journal of Applied Meteorology*, 33:1382–1401.

Chen, F. and Dudhia, J. (2001). Coupling an advanced land surface-hydrology model with the Penn State-NCAR MM5 modeling system. Part I: Model implementation and sensitivity. *Monthly Weather Review*, 129:569–585.

Cheng, A., Xu, K.-M., and Stevens, B. (2010). Effects of resolution on the simulation of boundary-layer clouds and the partition of kinetic energy to subgrid scales. *Journal of Advances in Modeling Earth Systems*, 2:1–21.

Clapp, R. and Hornberger, G. (1978). Empirical equations for some soil hydraulic properties. *Water resources research*, 14(4):601–604.

Clark, C. and Arritt, P. (1995). Numerical simulations of the effect of soil moisture and vegetation cover on the development of deep convection. *Journal of Applied Meteorology*, 34:2029–2045.

Clark, D. B. and Taylor, C. M. (2004). Feedback between the Land Surface and Rainfall at Convective Length Scales. *Journal of Hydrometeorology*, 5:625–639.

Claussen, M. (1991). Estimation of areally-averaged surface fluxes. *Boundary-Layer Meteorology*, 54:387–410.

Claussen, M., Brovkin, V., and Ganopolski, A. (2001). Biogeophysical versus biogeochemical feedbacks of largescale land cover change. *Geophysical Research Letters*, 28(6):1011–1014.

Cooper, H. J., Garstang, M., and Simpson, J. (1982). The diurnal interaction between convection and penninsular-scale forcing over south florida. *Monthly Weather Review*, 110:486–503.

Crosman, E. T. and Horel, J. D. (2010). Sea and Lake Breezes: A Review of Numerical Studies. *Boundary-Layer Meteorology*, 137(1):1–29.

Cutrim, E., Martin, D., and Rabin, R. (1995). Enhancement of Cumulus Clouds over Deforested Lands in AMazonia. *Bulletin of the American Meteorological Society*, 76:1801–1805.

Dalu, G. and Pielke, R. (1989). An Analytical Study of the Sea Breeze. *Journal of the Atmospheric Sciences*, 46(12):1815–1825.

Dawe, J. T. and Austin, P. H. (2012). Statistical analysis of an LES shallow cumulus cloud ensemble using a cloud tracking algorithm. *Atmospheric Chemistry and Physics*, 12(2):1101–1119.

de Rooy, W. C., Bechtold, P., Fröhlich, K., Hohenegger, C., Jonker, H., Mironov, D., Pier Siebesma, a., Teixeira, J., and Yano, J.-I. (2013). Entrainment and detrainment in cumulus convection: an overview. *Quarterly Journal of the Royal Meteorological Society*, 139(670):1–19.

Dickinson, R. E. and Kennedy, P. (1992). Impacts on regional climate of Amazon deforestation.

Drobinski, P. and Dubos, T. (2009). Linear breeze scaling: from large-scale land/sea breezes to mesoscale inland breezes. *Quarterly Journal of the Royal Meteorological Society*, 135(644):1766–1775.

Duynkerke, P. (1999). Turbulence, radiation and fog in Dutch stable boundary layers. *Boundary-Layer Meteorology*, 90:447–477.

Emori, S. (1998). The interaction of cumulus convection with soil moisture distribution: An idealized simulation. *Journal of Geophysical Research*, 103(D8):8873.

Findell, K. and Eltahir, E. (2003). Atmospheric controls on soil moisture-boundary layer interactions. Part I: Framework development. *Journal of Hydrometeorology*, 4:552–569.

Flato, G., Marotzke, J., Abiodun, B., Braconnot, P., Chou, S. C., Collins, W., Cox, P., Drouech, F., Emori, S., Eyring, C., Forest, C., Gleckler, E., Guilyardi, E., Jakob, C., Kattsov, V., Reason, C., and Rummukainen, M. (2013). Evaluation of Climate Models. *Climate Change 2013: The Physical Science Basis. Contribution of Working Group I to the Fifth Assessment Report of the Intergovernmental Panel on Climate Change. Cambridge University Press, Cambridge, United Kingdom and New York, NY, USA*.

Fritsch, J., Kane, R., and Chelius, C. (1986). The contribution of mesoscale convective weather systems to the warm-season precipitation in the United States. *Journal of Climate and Applied Meteorology*, 25:1333–1345.

Froidevaux, P. (2014). Influence of the background wind on the local soil moisture-precipitation feedback. *Journal of the Atmospheric Sciences*, 71:782–799.

Fu, Q. and Liou, K. N. (1993). Parameterization of the Radiative Properties of Cirrus Clouds. *Journal of the Atmospheric Sciences*, 50(13):2008–2024.

Garcia-Carreras, L., Parker, D. J., and Marsham, J. H. (2011). What is the Mechanism for the Modification of Convective Cloud Distributions by Land Surface Induced Flows? *Journal of the Atmospheric Sciences*, 68(3):619–634.

Graf, H.-F. and Yang, J. (2007). Evaluation of a new convective cloud field model: precipitation over the maritime continent. *Atmospheric Chemistry and Physics*, 7(2):409–421.

Grandpeix, J.-Y. and Lafore, J.-P. (2010). A Density Current Parameterization Coupled with Emanuels Convection Scheme. Part I: The Models. *Journal of the Atmospheric Sciences*, 67(4):881–897.

Heus, T. and Seifert, a. (2013). Automated tracking of shallow cumulus clouds in large domain, long duration large eddy simulations. *Geoscientific Model Development*, 6(4):1261–1273.

Heus, T., van Heerwaarden, C. C., Jonker, H. J. J., Pier Siebesma, A., Axelsen, S., van den Dries, K., Geoffroy, O., Moene, a. F., Pino, D., de Roode, S. R., and Vilà-Guerau de Arellano, J. (2010). Formulation of the Dutch Atmospheric Large-Eddy Simulation (DALES) and overview of its applications. *Geoscientific Model Development*, 3:415–444.

Hohenegger, C., Brockhaus, P., Bretherton, C. S., and Schär, C. (2009). The Soil Moisture Precipitation Feedback in Simulations with Explicit and Parameterized Convection. *Journal of Climate*, 22(19):5003–5020.

Hohenegger, C., Schlemmer, L., Stevens, B., and Silvers, L. (2014). Coupling of convection and mesoscale circulation across resolution. *Tellus*, 0(0):submitted.

Hohenegger, C. and Stevens, B. (2013). Preconditioning Deep Convection with Cumulus Congestus. *Journal of the Atmospheric Sciences*, 70(2):448–464.

Huang, H.-Y. and Margulis, S. a. (2011). Investigating the Impact of Soil Moisture and Atmospheric Stability on Cloud Development and Distribution Using a Coupled Large-Eddy Simulation and Land Surface Model. *Journal of Hydrometeorology*, 12(5):787–804.

Huang, H.-y. and Margulis, S. A. (2012). Impact of soil moisture heterogeneity length scale and gradients on daytime coupled land-cloudy boundary layer interactions. *Hydrological Processes*, 27:1988–2003.

Jacob, D. (1991). *Numerische Simulation der Wolkenbildung in einer Land-Seewind-Zirkulation*. Dissertation, Universität Hamburg.

Jakob, C. (2010). Accelerating Progress in Global Atmospheric Model Development through Improved Parameterizations: Challenges, Opportunities, and Strategies. *Bulletin of the American Meteorological Society*, 91(7):869–875.

Jarvis, P. G. (1976). The Interpretation of the Variations in Leaf Water Potential and Stomatal Conductance Found in Canopies in the Field. *Philosophical Transactions of the Royal Society of London*, 273(927):593–610.

Kain, J. S. (2004). The Kain Fritsch Convective Parameterization: An Update. *Journal of Applied Meteorology*, 43(1980):170–181.

Kang, S.-L. and Bryan, G. H. (2011). A Large-Eddy Simulation Study of Moist Convection Initiation over Heterogeneous Surface Fluxes. *Monthly Weather Review*, 139(9):2901–2917.

Khairoutdinov, M. and Randall, D. (2006). High-Resolution Simulation of Shallow-to-Deep Convection Transition over Land. *Journal of the Atmospheric Sciences*, 63:3421–3436.

Kingsmill, D. E. (1995). Convection Initiation Associated with a Sea-Breeze Front, a Gust Front, and Their Collision. *Monthly Weather Review*, 123:2913–2933.

Knippertz, P., Trentmann, J., and Seifert, a. (2009). Highresolution simulations of convective cold pools over the northwestern Sahara. *Journal of Geophysical Research*, 114(D8):D08110.

Koster, R. and Suarez, M. (1992). A comparative analysis of two land surface heterogeneity representations. *Journal of climate*, 5:1379–1390.

Koster, R. D., Dirmeyer, P. a., Guo, Z., Bonan, G., Chan, E., Cox, P., Gordon, C. T., Kanae, S., Kowalczyk, E., Lawrence, D., Liu, P., Lu, C.-H., Malyshev, S., McAvaney, B., Mitchell, K., Mocko, D., Oki, T., Oleson, K., Pitman, A., Sud, Y. C., Taylor, C. M., Verseghy, D., Vasic, R., Xue, Y., and Yamada, T. (2004). Regions of strong coupling between soil moisture and precipitation. *Science (New York, N.Y.)*, 305(5687):1138–40.

Kuang, Z. and Bretherton, C. S. (2006). A Mass-Flux Scheme View of a High-Resolution Simulation of a Transition from Shallow to Deep Cumulus Convection. *Journal of the Atmospheric Sciences*, 63:1895–1909.

Kühnlein, C., Keil, C., Craig, G. C., and Gebhardt, C. (2014). The impact of downscaled initial condition perturbations on convective-scale ensemble forecasts of precipitation. *Quarterly Journal of the Royal Meteorological Society*, 140:1552–1562.

Kuo, H. (1965). On formation and intensification of tropical cyclones through latent heat release by cumulus convection. *Journal of the Atmospheric Sciences*, 22:40–63.

Langhans, W., Schmidli, J., and Schär, C. (2012). Bulk Convergence of Cloud-Resolving Simulations of Moist Convection over Complex Terrain. *Journal of the Atmospheric Sciences*, 69(7):2207–2228.

Lohou, F. and Patton, E. G. (2014). Surface Energy Balance and Buoyancy Response to Shallow Cumulus Shading. *Journal of the Atmospheric Sciences*, 71(2):665–682.

Louis, J.-F. (1979). A parametric model of vertical eddy fluxes in the atmosphere. *Boundary-Layer Meteorology*, 17:187–202.

Lynn, B. and Tao, W. (2001). A parameterization for the triggering of landscape-generated moist convection. Part II: Zero-order and first-order closure. *Journal of the Atmospheric Sciences*, 58:593–607.

Lynn, B., Tao, W.-K., and Abramopoulos, F. (2001). A Parameterization for the Triggering of Landscape-Generated Moist Convection. Part I: Analysis of High-Resolution Model Results. *Journal of the Atmospheric Sciences*, 58:575–592.

Lynn, B., Tao, W.-K., and Wetzel, P. (1998). A Study of Landscape-Generated Deep Moist Convection. *Monthly Weather Review*, 126:928–942.

Manabe, S. and Strickler, R. (1964). Thermal equilibrium of the atmosphere with a convective adjustment. *Journal of the Atmospheric Sciences*, 21:361–385.

Marshall, C. H. and Pielke, R. A. (2004). The Impact of Anthropogenic Land-Cover Change on the Florida Peninsula Sea Breezes and Warm Season Sensible Weather. *Monthly Weather Review*, 132:28–52.

Mathon, V., Laurent, H., and Lebel, T. (2002). Mesoscale Convective System Rainfall in the Sahel. *Journal of Applied Meteorology*, 41(11):1081–1092.

McGuffie, K., Henderson-Sellers, A., Zhang, H., Durbidge, T. B., and Pitman, A. J. (2007). Global climate sensitivity to tropical deforestation. *Global and Planetary Change*, 10:97–128.

Miller, S. T. K., Keim, B. D., Talbot, R. W., and Mao, H. (2003). Sea breeze: Structure, forecasting, and impacts. *Reviews of Geophysics*, 41(3):1011.

Monteith, J. L. (1965). Evaporation and environment. *Symp. Soc. Exp. Biol*, 19:205–234.

Neggers, R. a. J. (2009). A Dual Mass Flux Framework for Boundary Layer Convection. Part II: Clouds. *Journal of the Atmospheric Sciences*, 66(6):1489–1506.

Neggers, R. A. J., Jonker, H. J. J., and Siebesma, P. (2003). Size Statistics of Cumulus Cloud Populations in Large-Eddy Simulations. *Journal of the Atmospheric Sciences*, 60:1060–1074.

Nicholls, M. E., Pielke, R. A., and Cotton, W. R. (1991). A Two-Dimensional Numerical Investigation of the Interaction between Sea Breezes and Deep Convection over the Florida Peninsula. *Monthly Weather Review*, 119:298–323.

Noilhan, J. and Lacarrere, P. (1995). GCM grid-scale evaporation from mesoscale modeling. *Journal of Climate*, 8:206–223.

Pearson, K. J., Lister, G. M. S., Birch, C. E., Allan, R. P., Hogan, R. J., and Woolnough, S. J. (2014). Modelling the diurnal cycle of tropical convection across the grey zone. *Quarterly Journal of the Royal Meteorological Society*, 140(679):491–499.

Penman, H. (1948). Natural evaporation from open water, bare soil and grass. *Proceedings of the Royal Society*, 193(1032):120–145.

Petch, J. C., Brown, a. R., and Gray, M. E. B. (2002). The impact of horizontal resolution on the simulations of convective development over land. *Quarterly Journal of the Royal Meteorological Society*, 128(584):2031–2044.

Peters-Lidard, C. (1998). The effect of soil thermal conductivity parameterization on surface energy fluxes and temperatures. *Journal of the Atmospheric Sciences*, 55:1209–1224.

Pielke, R. A. (2001). Influence of the spatial distribution of vegetation and soils on the prediction of cumulus convective rainfall. *Reviews of Geophysics*, 39(2):151–177.

Pielke, R. A. and Avissar, R. (1990). Influence of landscape structure on local and regional climate. *Landscape Ecology*, 4:133–155.

Pincus, R. and Stevens, B. (2009). Monte Carlo Spectral Integration: a Consistent Approximation for Radiative Transfer in Large Eddy Simulations. *Journal of Advances in Modeling Earth Systems*, 1(2):1–9.

Pincus, R. and Stevens, B. (2013). Paths to accuracy for radiation parameterizations in atmospheric models. *Journal of Advances in Modeling Earth Systems*, 5(2):225–233.

Plant, R. S. and Craig, G. C. (2008). A Stochastic Parameterization for Deep Convection Based on Equilibrium Statistics. *Journal of the Atmospheric Sciences*, 65(1):87–105.

Protat, A. and Zawadzki, I. (1999). A variational method for real-time retrieval of three-dimensional wind field from multiple-Doppler bistatic radar network data. *Journal of Atmospheric and Oceanic Technology*, 16:432–449.

Raasch, S. and Harbusch, G. (2001). An analysis of secondary circulations and their effects caused by small-scale surface inhomogeneities using large-eddy simulation. *Boundary-Layer Meteorology*, 101:31–59.

Rabin, R. and Stensrud, D. (1990). Observed effects of landscape variability on convective clouds. *Bulletin of the American Meteorological Society*, 71(3):272–280.

Richards, L. a. (1931). Capillary Conduction of Liquids Through Porous Mediums. *Journal of Applied Physics*, 1(5):318–333.

Rieck, M., Nuijens, L., and Stevens, B. (2012). Marine Boundary Layer Cloud Feedbacks in a Constant Relative Humidity Atmosphere. *Journal of the Atmospheric Sciences*, 69(8):2538–2550.

Robinson, F. J., Patterson, M. D., and Sherwood, S. C. (2013). A Numerical Modeling Study of the Propagation of Idealized Sea-Breeze Density Currents. *Journal of the Atmospheric Sciences*, 70(2):653–668.

Robinson, F. J., Sherwood, S. C., and Li, Y. (2008). Resonant Response of Deep Convection to Surface Hot Spots. *Journal of the Atmospheric Sciences*, 65(1):276–286.

Ross, A. N., Tompkins, A. M., and Parker, D. J. (2004). Simple Models of the Role of Surface Fluxes in Convective Cold Pool Evolution. *Journal of the Atmospheric Sciences*, 61(1980):1582–1595.

Rotunno, R. (1983). On the Linear Theory of the Land and Sea Breeze. *Journal of the Atmospheric Sciences*, 40:1999–2009.

Rotunno, R. (1988). A Theory for Strong, Long-Lived Squall Lines. *Journal of the Atmospheric Sciences*, 45:463–485.

Roy, S. B. (2003). A preferred scale for landscape forced mesoscale circulations? *Journal of Geophysical Research*, 108(D22):8854.

Sakradzija, M., Seifert, a., and Heus, T. (2014). Fluctuations in a quasi-stationary shallow cumulus cloud ensemble. *Nonlinear Processes in Geophysics Discussions*, 1(2):1223–1282.

Savic-Jovcic, V. and Stevens, B. (2008). The Structure and Mesoscale Organization of Precipitating Stratocumulus. *Journal of the Atmospheric Sciences*, 65(5):1587–1605.

Schaake, J. C., Koren, V. I., Duan, Q.-y., and Chen, F. (1996). Simple water balance model for estimating runoff at different spatial and temporal scales. *Journal of Geophysical Research*, 101:7461–7475.

Schlemmer, L. and Hohenegger, C. (2014). The formation of wider clouds by cold pool dynamics. *Journal of the Atmospheric Sciences*, 71:2842–2858.

Schlemmer, L., Hohenegger, C., Schmidli, J., Bretherton, C. S., and Schär, C. (2011). An Idealized Cloud-Resolving Framework for the Study of Midlatitude Diurnal Convection over Land. *Journal of the Atmospheric Sciences*, 68(5):1041–1057.

Schlemmer, L., Hohenegger, C., Schmidli, J., and Schär, C. (2012). Diurnal equilibrium convection and land surface-atmosphere interactions in an idealized cloud-resolving model. *Quarterly Journal of the Royal Meteorological Society*, 138(667):1526–1539.

Schmetz, J., Pili, P., Tjemkes, S., Just, D., Kerkmann, J., Rota, S., and Ratier, A. (2002). An introduction to Meteosat Second Generation (MSG). *Bulletin of the American Meteorological Society*, 83:977–992.

Segal, M. and Arritt, R. (1992). Nonclassical mesoscale circulations caused by surface sensible heat-flux gradients. *Bulletin of the American Meteorological Society*, 73(10):1593–1604.

Segal, M., Purdom, J. F. W., Song, J. L., Pielke, R. A., and Mahrer, Y. (1986). Evaluation of Cloud Shading Effects on the Generation and Modification of Mesoscale Circulations. *Monthly Weather Review*, 114:1201–1212.

Seifert, A. and Beheng, K. D. (2005). A two-moment cloud microphysics parameterization for mixed-phase clouds. Part 2: Maritime vs. continental deep convective storms. *Meteorology and Atmospheric Physics*, 92:67–82.

Seifert, A. and Heus, T. (2013). Large-eddy simulation of organized precipitating trade wind cumulus clouds. *Atmospheric Chemistry and Physics*, 13(11):5631–5645.

Seitter, K. L. (1986). A Numerical Study of Atmospheric Density Current Motion Including the Effects of Condensation. *Journal of the Atmospheric Sciences*, 43(24):3068–3076.

Seneviratne, S. I., Corti, T., Davin, E. L., Hirschi, M., Jaeger, E. B., Lehner, I., Orlowsky, B., and Teuling, A. J. (2010). Investigating soil moistureclimate interactions in a changing climate: A review. *Earth-Science Reviews*, 99(3-4):125–161.

Seneviratne, S. I., Lüthi, D., Litschi, M., and Schär, C. (2006). Land-atmosphere coupling and climate change in Europe. *Nature*, 443:205–209.

Sherwood, S. C., Bony, S., and Dufresne, J.-L. (2014). Spread in model climate sensitivity traced to atmospheric convective mixing. *Nature*, 505(7481):37–42.

Shukla, J., Nobre, C., and Sellers, P. (1990). Amazon deforestation and climate change. *Science (New York, N.Y.)*, 247:1322–1325.

Siebesma, A. (1998). Shallow cumulus convection. In *Buoyant convection in geophysical flows*, pages 441–486. Springer.

Skamarock, W. C. (2004). Evaluating Mesoscale NWP Models Using Kinetic Energy Spectra. *Monthly Weather Review*, 132(12):3019–3032.

Srivastava, R. C. (1987). A Model of intense downdrafts driven by the melting and evaporation of precipitation. *Journal of the Atmospheric Sciences*, 44(13):1752–1773.

Stensrud, D. J. (2007). *Parameteriation schemes: Keys to understanding numerical weather prediction models.* Cambridge University Press.

Stevens, B. and Bony, S. (2013). Water in the atmosphere. *Physics Today*, 66(6):29.

Stevens, B., Moeng, C.-H., Ackerman, A. S., Bretherton, C. S., Chlond, A., de Roode, S., Edwards, J., Golaz, J.-C., Jiang, H., Khairoutdinov, M., Kirkpatrick, M. P., Lewellen, D. C., Lock, A., Müller, F., Stevens, D. E., Whelan, E., and Zhu, P. (2005). Evaluation of Large-Eddy Simulations via Observations of Nocturnal Marine Stratocumulus. *Monthly Weather Review*, 133:1443–1462.

Steyn, D. G. (1998). Scaling the vertical structure of sea breezes. *Boundary-Layer Meteorology*, 86(1995):505–524.

Stull, R. B. (2000). *Meteorology for scientists and engineers.* Brooks/Cole, 2nd edition.

Su, H., McCabe, M. F., and Wood, E. F. (2005). Modeling Evapotranspiration during SMACEX : Comparing Two Approaches for Local- and Regional-Scale Prediction. *Journal of Hydrometeorology*, 6:910–922.

Sullivan, P., Moeng, C.-H., Stevens, B., Lenschow, D., and Mayor, S. (1998). Structure of the Entrainment Zone Capping the Convective Atmospheric Boundary Layer. *Journal of the Atmospheric Sciences*, 55:3042–3064.

Sullivan, P. P. and Patton, E. G. (2011). The Effect of Mesh Resolution on Convective Boundary Layer Statistics and Structures Generated by Large-Eddy Simulation. *Journal of the Atmospheric Sciences*, 68(10):2395–2415.

Taylor, C., Saïd, F., and Lebel, T. (1997). Interactions between the land surface and mesoscale rainfall variability during HAPEX-Sahel. *Monthly Weather Review*, 125:2211–2227.

Taylor, C. M., Gounou, A., Guichard, F., Harris, P. P., Ellis, R. J., Couvreux, F., and De Kauwe, M. (2011). Frequency of Sahelian storm initiation enhanced over mesoscale soil-moisture patterns. *Nature Geoscience*, 4(7):430–433.

Taylor, C. M., Parker, D. J., and Harris, P. P. (2007). An observational case study of mesoscale atmospheric circulations induced by soil moisture. *Geophysical Research Letters*, 34(15):L15801.

Teuling, A. J., Seneviratne, S. I., Stöckli, R., Reichstein, M., Moors, E., Ciais, P., Luyssaert, S., van den Hurk, B., Ammann, C., Bernhofer, C., Dellwik, E., Gianelle, D., Gielen, B., Grünwald, T., Klumpp, K., Montagnani, L., Moureaux, C., Sottocornola, M., and Wohlfahrt, G. (2010). Contrasting response of European forest and grassland energy exchange to heatwaves. *Nature Geoscience*, 3(10):722–727.

Tiedtke, M. (1989). A comprehensive mass flux scheme for cumulus parameterization in large-scale models. *Monthly Weather Review*, 117:1779–1800.

Tompkins, A. M. (2001). Organization of Tropical Convection in Low Vertical Wind Shears: The Role of Cold Pools. *Journal of the Atmospheric Sciences*, 58(13):1650–1672.

Van Heerwaarden, C. C. and Vilà-Guerau de Arellano, J. (2008). Relative Humidity as an Indicator for Cloud Formation over Heterogeneous Land Surfaces. *Journal of the Atmospheric Sciences*, 65(10):3263–3277.

van Heerwaarden, C. C., Vilà-Guerau de Arellano, J., Gounou, A., Guichard, F., and Couvreux, F. (2010). Understanding the Daily Cycle of Evapotranspiration: A Method to Quantify the Influence of Forcings and Feedbacks. *Journal of Hydrometeorology*, 11(6):1405–1422.

VanZanten, M. C., Stevens, B., Nuijens, L., Siebesma, a. P., Ackerman, a. S., Burnet, F., Cheng, a., Couvreux, F., Jiang, H., Khairoutdinov, M., Kogan, Y., Lewellen, D. C., Mechem, D., Nakamura, K., Noda, a., Shipway, B. J., Slawinska, J., Wang, S., and Wyszogrodzki, a. (2011). Controls on precipitation and cloudiness in simulations of trade-wind cumulus as observed during RICO. *Journal of Advances in Modeling Earth Systems*, 3(6):M06001.

Wakimoto, R. M. (1982). The Life Cycle of Thunderstorm Gust Fronts as Viewed with Dopper Radar and Rawinsonde Data. *Monthly Weather Review*, 110:1060–1082.

Wang, J., Bras, R. L., and Eltahir, E. A. B. (1996). A stochastic Linear Theory of Mesoscale Circulation Induced by the Thermal Heterogeneity of the Land Surface. *Journal of the Atmospheric Sciences*, 53:3349–3366.

Wieringa, J. (1986). Roughness-dependent geographical interpolation of surface wind speed averages. *Quarterly Journal of the Royal Meteorological Society*, 112:867–889.

Williams, E. (2002). Contrasting convective regimes over the Amazon: Implications for cloud electrification. *Journal of Geophysical Research*, 107(D20):8082.

Wood, R. and Field, P. R. (2011). The Distribution of Cloud Horizontal Sizes. *Journal of Climate*, 24(18):4800–4816.

Wu, C.-M., Stevens, B., and Arakawa, A. (2009). What Controls the Transition from Shallow to Deep Convection? *Journal of the Atmospheric Sciences*, 66(6):1793–1806.

Zhang, H., Henderson-Sellers, A., and Mc (1996). Impacts of tropical deforestation. Part I: Process analysis of local climatic change. *Journal of Climate*, 9:1497–1517.

Zhang, Y. and Klein, S. a. (2010). Mechanisms Affecting the Transition from Shallow to Deep Convection over Land: Inferences from Observations of the Diurnal Cycle Collected at the ARM Southern Great Plains Site. *Journal of the Atmospheric Sciences*, 67(9):2943–2959.

Zipser, E. J., Liu, C., Cecil, D. J., Nesbitt, S. W., and Yorty, D. P. (2006). Where Are the Most Intense Thunderstorms on Earth? *Bulletin of the American Meteorological Society*, 87(8):1057–1071.

Acronyms

ARM-SGP	Atmospheric Radiation Measurement - Southern Great Plains
BOMEX	Barbados Oceanographic and Meteorological Experiment
COSMO	Consortium for Small-scale Modeling
CRM	Cloud Resolving Model
DALES	Dutch Atmospheric Large-Eddy Simulation
DCBL	Dry Convective Boundary Layer
DWD	Deutscher Wetterdienst (German Weather Service)
DYCOMS	Dynamics and Chemistry of Marine Stratocumulus
ECMWF-IFS	European Centre for Medium-Range Weather Forcasts - Integrated Forcasting System
FIFE	First ISLSCP (International Satellite Land Surface Climatology Project) Field Experiment
GCM	Global Circulation Model
HAPEX-Sahel	Hydrology-Atmosphere Pilot Experiment in the Sahel
Landsat-TM	Landsat Thermatic Mapper
LAI	Leaf Area Index
LBA	Large-Scale Biosphere-Atmosphere Experiment in Amazonia
LES	Large-Eddy Simulation
LSM	Land Surface Model
LST	Local Standard Time
MSE	Moist Static Energy
MSG	Meteosat Second Generation
NCAR	National Center of Atmospheric Research
NWP	Numerical Weather Prediction
PDF	Probability Density Function
PSD	Power Spectral Density
RICO	Rain in Cumulus over the Ocean
SMACEX	Soil Moisture Atmosphere Coupling Experiment
SWB	Simple Water Balance
TKE	Turbulent Kinetic Energy
UCLA-LES	University of California Los Angeles - Large-Eddy Simulation

List of Figures

1.1 Illustration of the components of the surface energy balance and the main interactions between the surface and the atmosphere. The dashed line represents the atmospheric boundary layer. The arrows at the surface represent the surface exchange of energy and water, whereas the arrows in the boundary layer represent surface induced mesoscale circulations. Q_{net} is the net radiation at the surface, F_{lat} the surface latent heat flux, F_{sens} the surface sensible heat flux, F_{soil} the soil heat flux, I the infiltration of precipitation, and R the surface runoff. 3

1.2 Illustration of the interactions studied in this dissertation. 7

2.1 Time series of domain mean (a) surface latent heat flux, (b) surface sensible heat flux, (c) boundary layer height and (d) vertical integrated turbulent kinetic energy for the models UCLA-LES and DALES and with fixed surface radiation. The other time series are determined with interactive diurnal radiation and show (e) the latent and (f) sensible heat fluxes scaled with Q_{net} and the (g) aerodynamic and (h) surface resistance for both models. 22

2.2 Vertical profiles of domain mean (a-d) liquid water potential temperature, (e-h) specific humidity for the models UCLA-LES and DALES. Configuration with prescribed surface energy (a,b,e,f) and with the coupled radiation scheme (c,d,g,h). Dashed lines indicate the initial conditions and continuos lines show values every consecutive hour (9-13 LST) with increasing shade of color. . . . 23

3.1 Initial profile of (a) liquid water potential temperature (θ_l) and (b) total water specific humidity (q_l). 28

3.2 Horizontal view of the surface fluxes, (a-f) sensible and (g-l) latent heat, in the different experiments at 11 LST. 30

3.3 Instantaneous view of the cloud field in terms of liquid water path in the different experiments at 11 LST. 32

3.4 Time series of domain averaged (a) cloud cover and (b) surface rain rate. . . 33

3.5 Domain averaged vertical profiles of cloud condensate for all experiments (a)-(f) (condensate includes liquid water, ice, snow, hail, graupel and rain). Vertical dashed lines denote transition time, where the cloud condensate exceeds 1 mg kg^{-1} at 5.5 km height. 35

3.6 Cloud size distribution for the various experiments at different times (a-d). The distributions are calculated from instantaneous values of the liquid water path sampled every 60 seconds and the distributions are averaged over 30 minutes. The same bin width is used among the various experiments. The bin width increases with time to account for the growing cloud population. 37

3.7 (a) Time series of the maximum cloud size for all experiments and (b) domain maximum vertical velocity. Cloud statistics and vertical velocity are sampled every 60 seconds, applying a 20 minutes running mean. Marker points denote the collision time. 38

3.8 Vertical cross section of cloud condensate (shaded contours in mg kg^{-1}) and horizontal wind (contour lines in m s^{-1} with background wind removed, black colors in positive and red colors in negative x-direction, intervals of 0.25 m s^{-1} starting at 0.5 m s^{-1}) for different experiments (a)-(e) at 11 LST. HET-S resembles HOM and is not shown. All quantities at a given location x are averaged in y-direction over patches with the same leaf area index. Dashed lines indicate patch boundaries in y-direction. 39

3.9 Vertical cross sections of the total water content (shaded contours in g kg^{-1}) for HET-M at (a) 9 and (b) 11 LST. All quantities at a given location x are averaged in y-direction over patches with the same leaf area index. Dashed lines indicate patch boundaries in y-direction. 41

3.10 Time series of mean boundary layer height sampled only above warm patches. Values are diagnosed from three-dimensional data every 30 minutes. 42

3.11 Vertical profile of bulk fractional entrainment rate for different experiments at 14:00 LST. The entrainment is diagnosed from LES data following Betts (1975) (see also de Rooy et al., 2013, Eq. 18). 43

4.1 Schematic illustration of the experiment setup. 50

4.2 Time series of domain mean quantities: (a) surface sensible heat flux, (b) cloud cover and (c) surface precipitation mixing ratio in CTL, NOCP and DRY. . . 52

4.3 Domain mean vertical profiles of (a) liquid water potential temperature, (b) total water and (c) relative humidity at 15 LST. 53

4.4 Propagation distance of the breeze front for all experiments. The position of the front is diagnosed from y-averaged data available every minute and displayed relative to x=0 km employing a running average over 20 minutes. . 55

4.5 Vertical cross section at 12 LST: (a) cloud condensate in NOCP (shaded contours in mg kg^{-1}) and virtual potential temperature anomalies in (b) NOCP and (c) DRY (shaded contours in K). The figures also show horizontal wind velocity (contour lines in 0.5 ms^{-1}, black colors in positive and red colors in negative x-direction). The x-axis denotes the distance to the interface between the two surface patches (Fig. 4.1: x=0), which also depicts the starting location of the front. 56

4.6 Time series of diagnosed virtual potential temperature difference across the front. The difference is calculated from the temperature averaged over 50 km on each side of the front in the horizontal and over the lowest 1500 m in the vertical. 57

4.7 Vertical xz cross section of experiments NOCP (a,b,c) and DRY (d,e) at 14 LST: (a,d) vertical velocity (shaded contours in m s^{-1}), (b,e) pressure perturbation, defined as the deviation from the domain mean (shaded contours in Pa), and (c) cloud condensate in NOCP (shaded contours in mg kg^{-1}). All figures also display the horizontal wind velocity (contour lines in 0.5 m s^{-1}, black colors in positive and red colors in negative x-direction). The x-axis denotes the distance to the interface between the two surface patches (Fig. 4.1: x=0), which also depicts the starting location of the front. 58

4.8 Horizontal cross section of virtual potential temperature close to the surface (z=125 m) at 16 LST for (a) CTL and (b) NOCP. The dashed white line represents the location of the front as shown in Fig. 4.4. The x-axis denotes the distance to the interface between the two surface patches (Fig. 4.1: x=0), which also depicts the starting location of the front. 59

4.9 (a,c) Cloud condensate (shaded contours in mg kg^{-1}) and (b,d) vertical velocity (shaded contours in m s^{-1}) for the experiments CTL and NOCP at 16 LST. All figures also display the horizontal wind velocity (contour lines in 0.5 m s^{-1}, black colors in positive and red colors in negative x-direction). The x-axis denotes the distance to the interface between the two surface patches (Fig. 4.1: x=0), which also depicts the starting location of the front. 60

4.10 Schematic illustration of the cloud circulation at the breeze front, the warm air towards the left and the cold air towards the right. Arrows denote the cloud base mass flux and the horizontal flux at the front, the dashed line indicates the position of the breeze front. The markers indicate the area where convective heating is strong. 63

4.11 Time series of (a) propagation velocity of the front diagnosed from LES, $c_{*,\mathrm{LES}}$, (b) propagation velocity predicted from Eq. 4.5, $c_{*,\mathrm{theory}}$, (c) velocity difference between the diagnosed values ($c_{*,\mathrm{LES}}$) and the theoretical values ($c_{*,\mathrm{theory}}$), (d) thermodynamical contribution calculated from Eq. 4.2, and (e) dynamical contribution calculated from Eq. 4.4. Quantities are diagnosed from y-averaged data available every minute employing a running average over 20 minutes. Detailed assumptions for the computation of the different terms are given in the text. 65

4.12 Conceptual stages of a mesoscale circulation interacting with precipitation convection: 1. Dry convective circulation, 2. enhanced propagation and vertical stretching and 3. acceleration due to cold pool activity behind the front. . . . 68

5.1 Initial atmospheric profile of (a) liquid water potential temperature and (b) specific humidity used in all experiments. 72

5.2 Functional relationship between surface latent heat flux (F_{lat}) and the soil moisture content (ϕ_{soil}) following Eq. 5.1. The two curves depict vegetation with large leaves (LAI=6, solid line) and small leaves (LAI=2, dashed line). The following parameters were fixed: Q_{net}=400 Wm^{-2}, F_{soil}=40 Wm^{-2}, $\frac{dq_{\mathrm{sat}}}{dT}$=7.9 g kg^{-1} K^{-1}, ρ=1.2 kg m^{-3}, c$_{\mathrm{p}}$=1004 J kg^{-1} K^{-1}, r_a=60 s m^{-1}, q_{atm}=8 g kg^{-1}, q_{sat}=10 g kg^{-1},L_v=2.5 10^6 J kg^{-1}, p_{00}=1000 hPa, $r_{\mathrm{surf,min}}$=150 s m^{-1}, ϕ_{wp}=0.171 m^3 m^{-3}, ϕ_{fc}=0.323 m^3 m^{-3} and f$_1$, f$_3$ and f$_4$ in Eq. 2.16 are set to 1. The colored markers indicate the soil moisture content used to initialize the model. The green marker denotes the experiments INF-01, NOINF-01, INF-02 and NOINF-02, whereas the yellow marker denotes the dry experiments INF-03 and NOINF-03. 73

5.3 Composite diurnal cycle of (a-f) cloud fraction and (g-l) surface precipitation, both time series are averaged over two weeks of simulation time. Grey shading indicates the minimum and maximum values around the mean. The first day of the simulations is omitted because of the very moist initial conditions that force earlier convection than on subsequent days. 75

5.4 Time series of the soil moisture content for the different experiments. 75

5.5 Horizontal distribution of surface latent heat fluxes at 8:30 LST for the dynamic experiments with strong heterogeneity amplitude (a,b) and with smaller amplitude (c,d). Left hand side figures show the conditions on the second day, whereas figures on the right hand side depict the situation at day 14. 77

5.6 Time series of (a) daily surface precipitation ratio between the warm and the cold patch, (b) latent heat flux ratio between the warm and the cold patch and (c) spatial correlation between latent heat flux at the second and subsequent days. All data used to calculate the ratios in (b) and the correlation in (c) is averaged between 7-8 LST of the corresponding day, while the precipitation data in (a) is averaged over full days. The black lines represent the experiment INF-01 (solid) and NOINF-01 (dashed), whereas the blue lines represent the experiments INF-02 (solid) and NOINF-02 (dashed). 78

5.7 Time series of normalized power spectral density (PSD) of the surface latent heat flux anomalies around the domain mean for experiments INF-01 and NOINF-01. The spectra are calculated from data that is time averaged (4 min) and tapered at the boundaries. The spectra are calculated from one-dimensional data in both x and y directions. This is justified because we assume isotropic structures in the surface fluxes such as convection and turbulence. To a first approximation, the surface patches are also isotropic. For each time step the PSD is normalized with the L$_2$ norm, $||\mathrm{PSD}||_{L_2} = (\sum_{k=1}^{k_{\max}} \mathrm{PSD}(k)^2)^{\frac{1}{2}}$, to show its relative contribution to the total variability. Data points where the average surface latent heat flux drops below 1 W m^{-2} are masked. 79

5.8 Instantaneous view on the cloud field in terms of liquid water path for INF-01 and NOINF-01. Two different time instances during the fourth day are shown: (a,b) at 10 LST and (c,d) at 14 LST. 81

List of Tables

2.1 Default values of the depth, temperature and soil moisture for each soil level from top to bottom. The values are interpolated from the land surface scheme used in the COSMO model in Schlemmer et al. (2011). 17

2.2 List of default values of all land surface and soil parameters applied in this dissertation. 19

3.1 Summary of the performed experiments with experiment name, patch size, local time of transition to deep convection, local time of breeze front collision and domain mean precipitation averaged over the simulation period. The transition time is determined from profile statistics sampled every 60 seconds. The collision time is diagnosed from vertical cross sections showing horizontal (as displayed in Fig. 3.8) and vertical wind, sampled from 3D data every 30 minutes. 34

4.1 Surface boundary conditions for experiment CTL at different times. F_{sens} denotes the sensible heat flux and F_{lat} the latent heat flux. The fluxes are shown for each of the two sub-domains with LAI=2 and LAI=6, respectively. 54

5.1 Summary of the performed experiments with initial conditions for soil moisture (ϕ), minimum and maximum value of leaf area index (LAI), vegetated fraction (c_{veg}) and bare soil fraction (c_{soil}). 73

Acknowledgements

I would like to express my special appreciation to my advisor Cathy Hohenegger. I thank her for her excellent guidance, her encouragement and interest in the topic and her valuable advice throughout my studies. I would like to thank my co-advisors Bjorn Stevens and Martin Claussen for their great support, especially during the final stage of my dissertation. In addition, I would like to acknowledge Jürgen Böhner and Lars Kaleschke for serving as commission members.

Special thanks to the members of my IMPRS panel, in particular to Alexander Löw for serving as my panel chair and to Axel Seifert, Bjorn Stevens and Cathy Hohenegger for their helpful comments. Thank you to the Herz Group on Clouds and Convection and especially Linda Schlemmer, Mirjana Sakradizija, Ritthik Bhattacharya and Vera Schemann for the discussions and support. It has been a pleasure to be part of this energetic and encouraging working group. I would especially like to thank my colleagues Andreas Chlond, Chiel van Heerwaarden, Irina Petrova, Juan Pedro Mellado and Karsten Peters for their inspiring comments, suggestions and ideas on part of my research. Special thanks to Pierre Gentine who hosted me during my stay at Columbia University, New York and who was always ready for lively and productive discussions.

Thanks to Tobias Becker, Katrin Lonitz, and Hauke Schulz, who shared an office with me and who were great room mates and always took their time to discuss. I would also like to thank Antje Weitz, Cornelia Kampmann, and Wiebke Böhm for their great job and support at the IMPRS-school. A special thanks to my dear friends Sebastian Schubert, Sebastian Schirber, David Broehan and Thomas Krismer for their helpful comments, discussions and the best lunch breaks. They have been great company during the last years. Finally, I would like to thank my parents and especially Katharina for their love and unconditional support.

Thank you!

Aus dieser Dissertation hervorgegangene Vorveröffentlichungen

List of Publications

Rieck M., C. Hohenegger and C. van Heerwaarden (2014): The influence of land surface heterogeneities on cloud size development. Mon. Wea. Rev., **142**, 3830–3846.

Rieck M., C. Hohenegger and P. Gentine (2015): The effect of moist convection on thermally induced mesoscale circulations. Q. J. R. Meteorol. Soc., revised.

Eidesstattliche Versicherung

Declaration on Oath

Hiermit erkläre ich an Eides statt, dass ich die vorliegende Dissertationsschrift selbst verfasst und keine anderen als die angegebenen Quellen und Hilfsmittel benutzt habe.

I hereby declare, on oath, that I have written the present dissertation by myself and have not used other than the acknowledged resources and aids.

Hamburg, den 10. Februar 2015

Hinweis / Reference

Die gesamten Veröffentlichungen in der Publikationsreihe des MPI-M
„Berichte zur Erdsystemforschung / Reports on Earth System Science",
ISSN 1614-1199

sind über die Internetseiten des Max-Planck-Instituts für Meteorologie erhältlich:
http://www.mpimet.mpg.de/wissenschaft/publikationen.html

All the publications in the series of the MPI -M
„Berichte zur Erdsystemforschung / Reports on Earth System Science",
ISSN 1614-1199

are available on the website of the Max Planck Institute for Meteorology:
http://www.mpimet.mpg.de/wissenschaft/publikationen.html